Figures

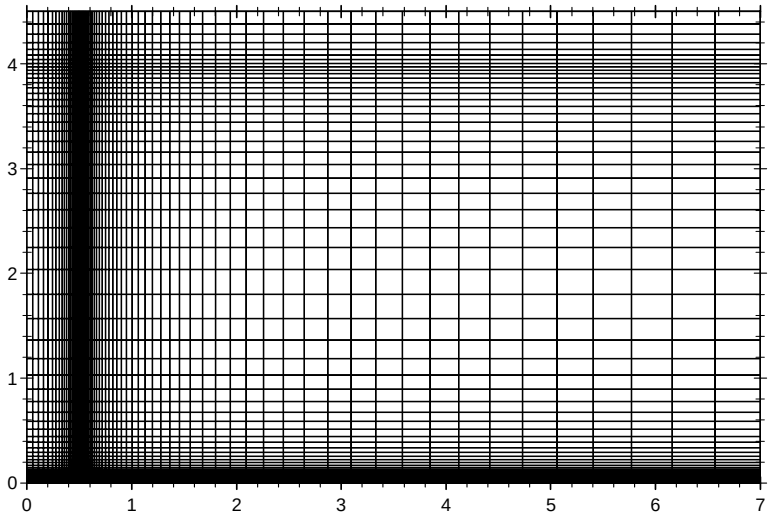

Figure 5.4: Low-Reynolds-number 90×70 (axial $\times$ radial) grid used in the impinging jet flow calculations.

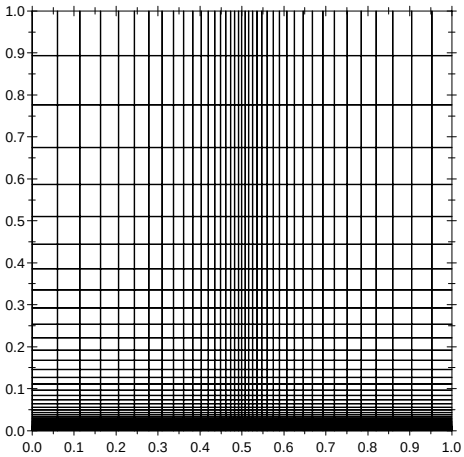

Figure 5.5: Close-up of wall-bounded region, low-Reynolds-number 90×70 (axial $\times$ radial) grid used in the impinging jet flow calculations.

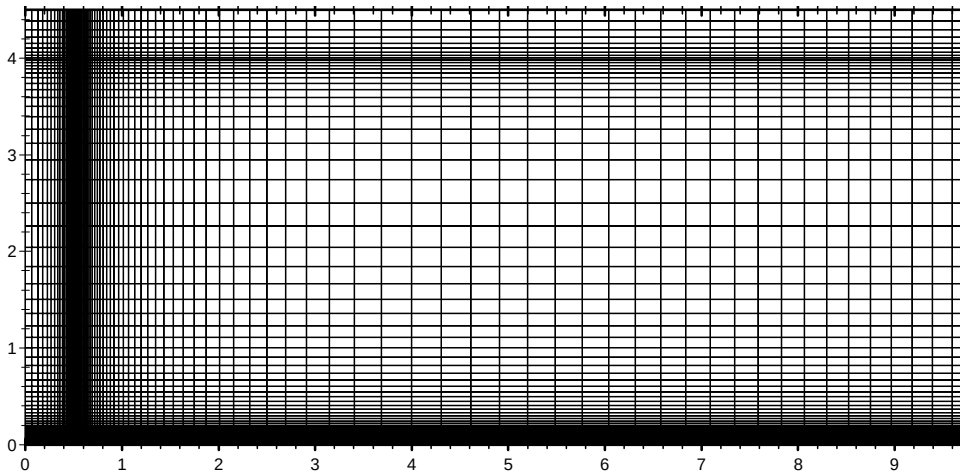

Figure 5.6: Low-Reynolds-number 120×90 grid used in the impinging jet flow calculations.

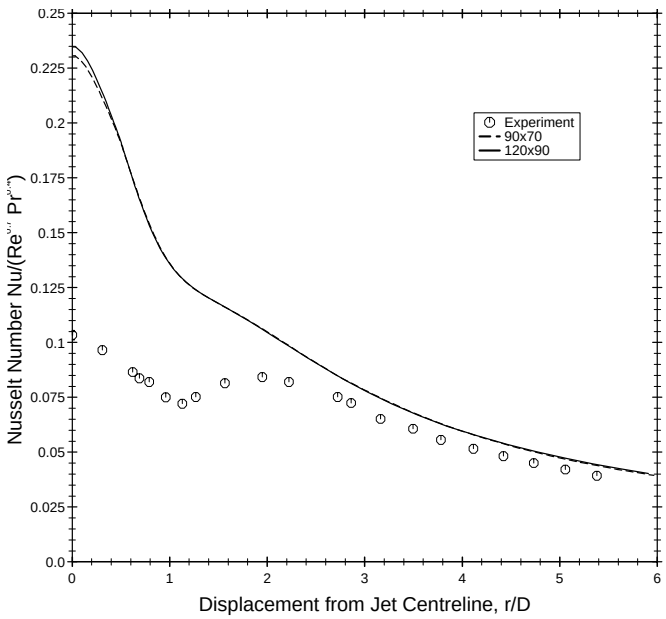

Figure 5.7: Comparison of Nusselt number predictions for the impinging jet flow with the 90×70 and 120×70 grids, using a linear $k - \varepsilon$ model with the standard Yap correction.

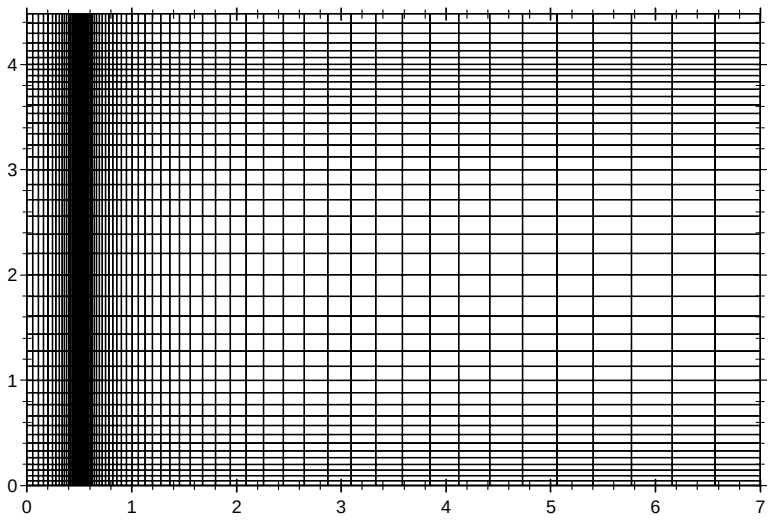

Figure 5.8: High-Reynolds-number 45×70 (axial $\times$ radial) grid used in the impinging jet flow with a near-wall cell size $DX = 250$.

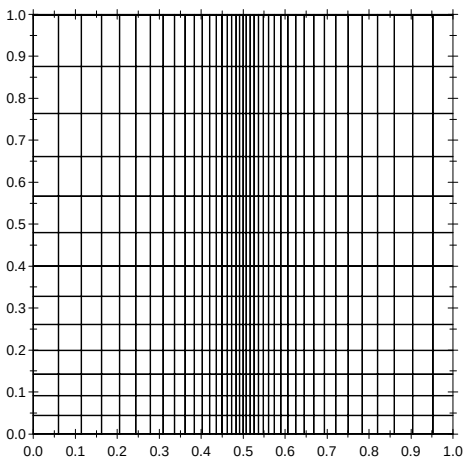

Figure 5.9: Close-up of wall-bounded region in the high-Reynolds-number 45×70 (axial $\times$ radial) grid used in the impinging jet flow with a near-wall cell size $DX = 250$.

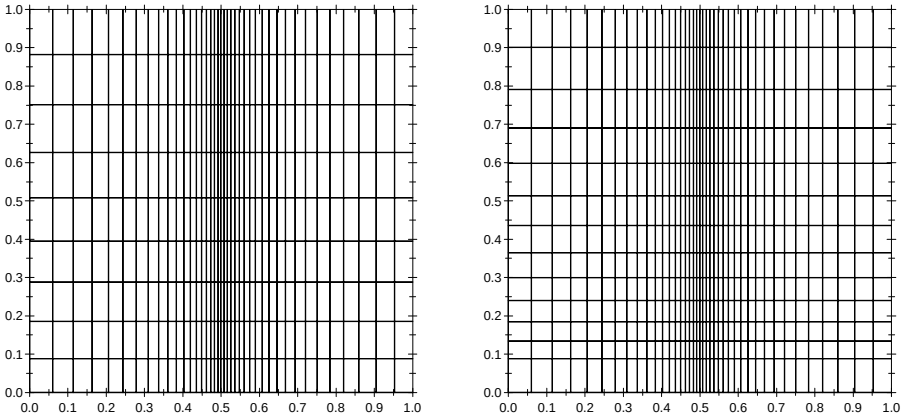

Figure 5.10: Comparison of near-wall region in the impinging jet flow for $DX = 500$ cells with continuous near-wall grid size (left) and 2:1 step change in grid size (right).

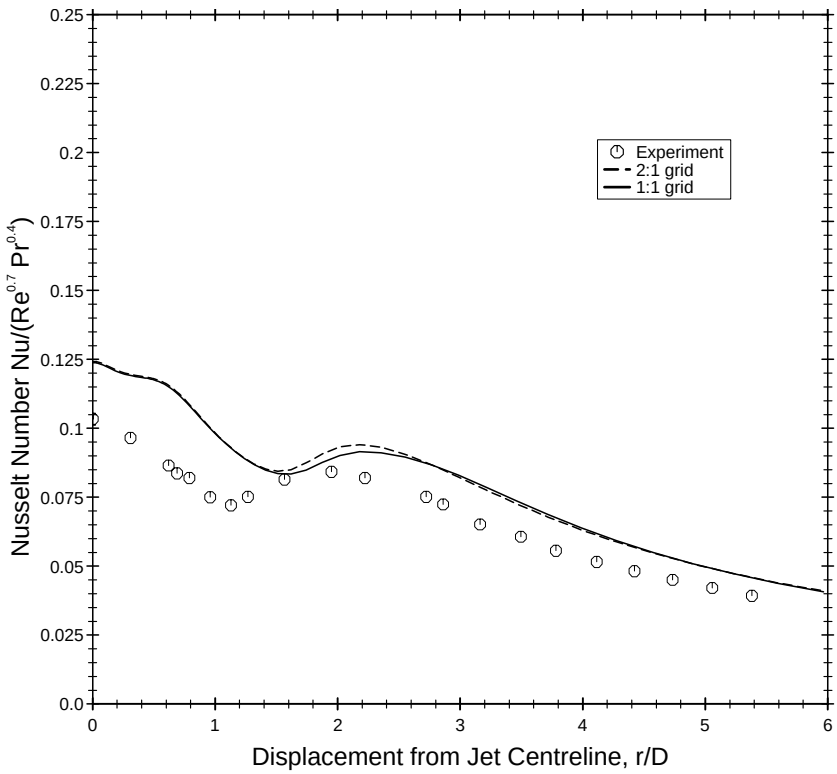

Figure 5.11: Comparison of Nusselt number predictions for the impinging jet flow with the $DX = 500$ continuous (1:1) grid and discontinuous (2:1) grids as shown in Figure 5.10, with the UMIST-*N* wall function, NLEVM of Craft *et al*. [67] and differential Yap correction.

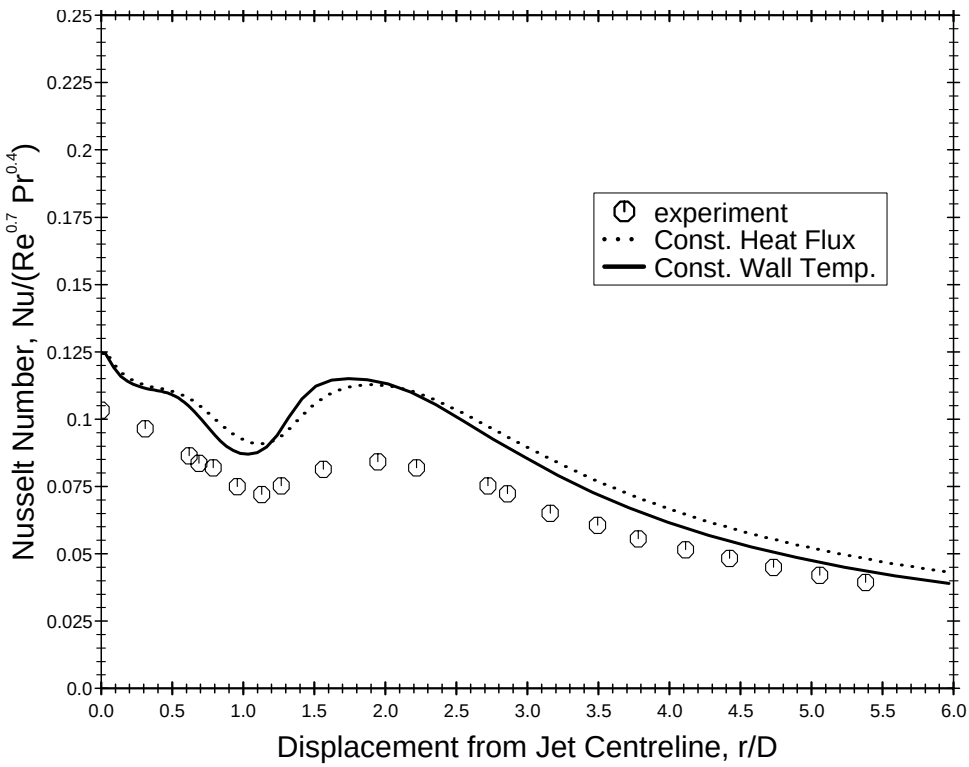

Figure 5.12: Comparison of Nusselt number predictions for the impinging jet flow using constant heat flux and constant wall temperature boundary conditions (broken and solid lines respectively). Both calculations used the low-*Re* non-linear $k-\varepsilon$ model of Craft *et al.* with the "standard" Yap correction. Symbols show the data points of the Baughn *et al*. [94] experiments which used constant wall temperature boundary conditions.

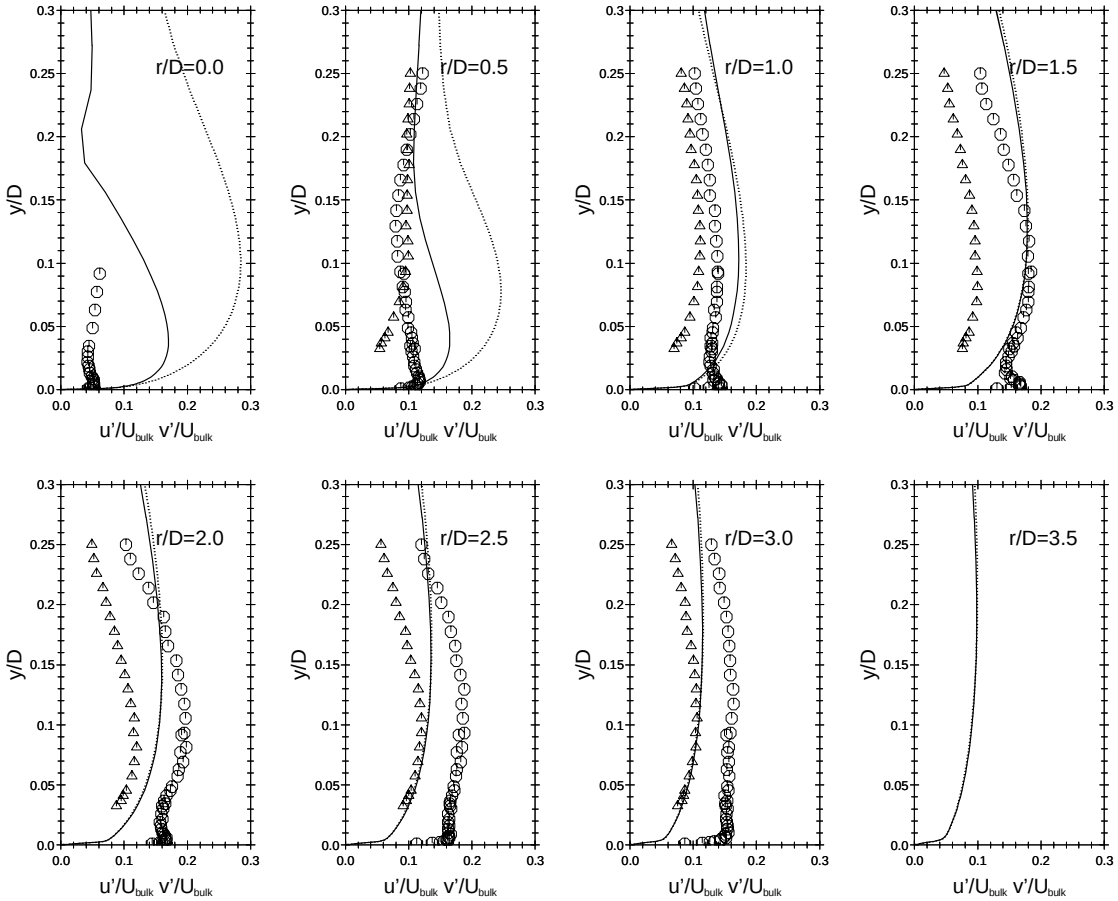

Figure 5.13: Radial (wall-parallel) and axial (wall-normal) RMS velocity components for the impinging jet flow at 8 radial positions using the low-*Re* linear $k-\varepsilon$ model with standard Yap correction. Lines represent the low-*Re* model predictions and symbols the experimental data of Cooper *et al*. [95]. —- and $\ominus$: radial u' component; ..... and $\triangle$: axial v' component.

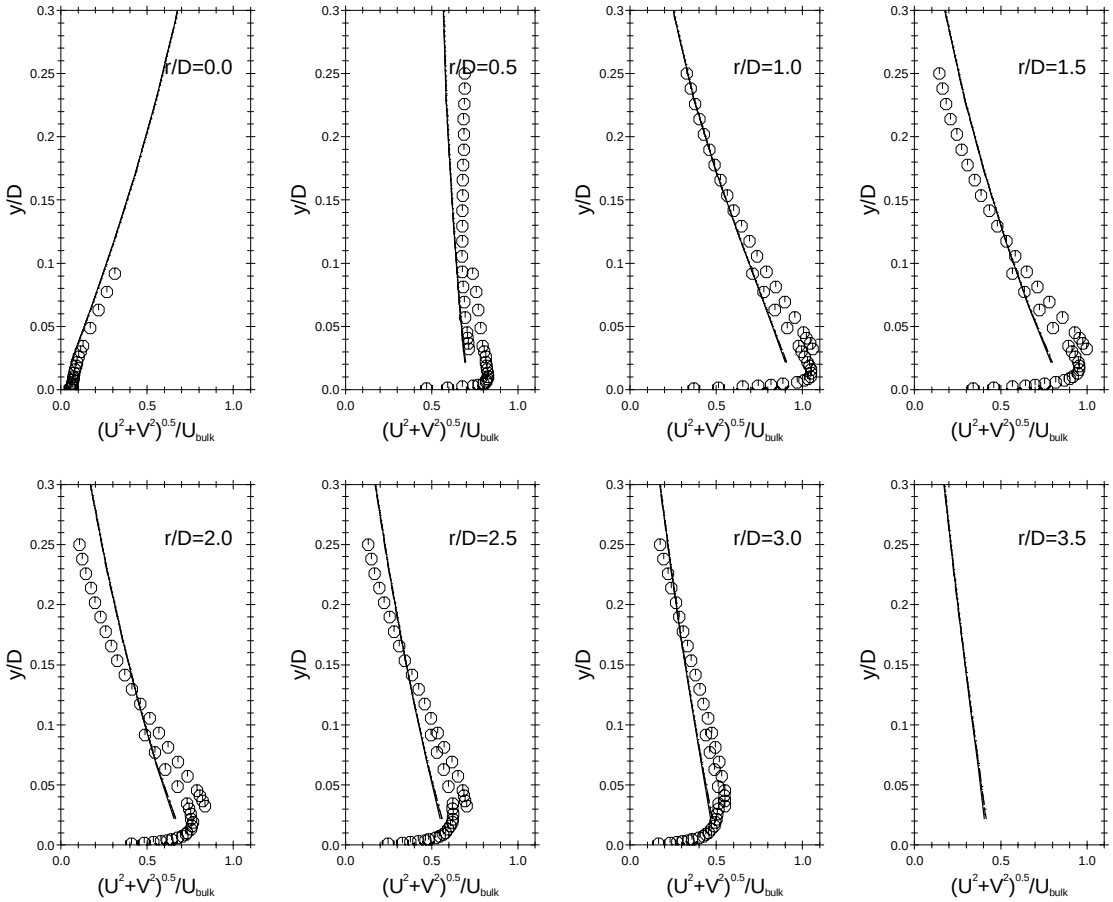

Figure 5.14: Resultant velocity profiles for the impinging jet flow at 6 radial positions using four "standard" wall functions with the linear $k-\varepsilon$ model, standard Yap correction and near-wall cell size $DX = 250$. ——: TEAM; - - -: SCL; – . –: CL; .....: JL; ⊖: experimental data of Cooper *et al*. [95]. Lines from the four wall function calculations lie on top of each other and have been shown up to the position of the near-wall node.

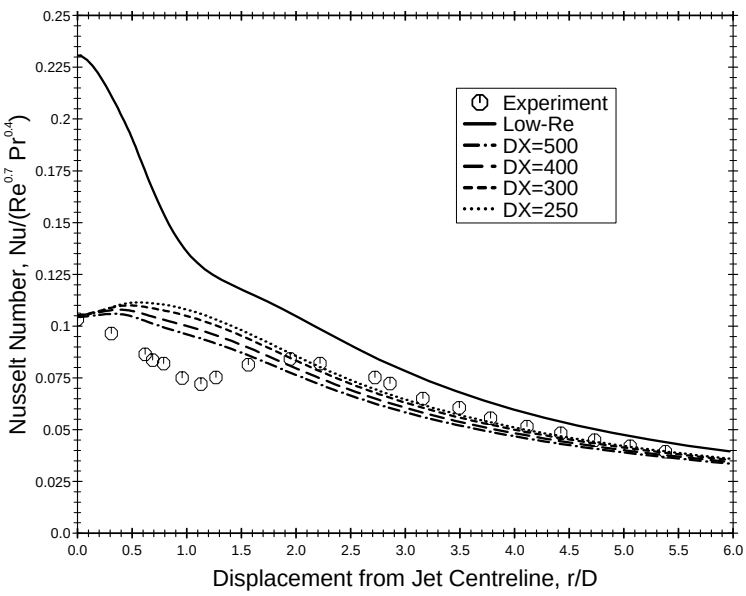

Figure 5.15: Nusselt number profiles obtained for the impinging jet flow using the Launder & Spalding (TEAM) wall function with the linear $k-\varepsilon$ model and standard Yap correction. Solid line: low-Reynolds-number model; broken lines: wall function results for different near-wall cell widths; symbols: experiments of Baughn *et al*. [94]. Normal stress components are included in the cell-averaged production term, $\overline{P_k}$, of the wall function (see Equation 2.49).

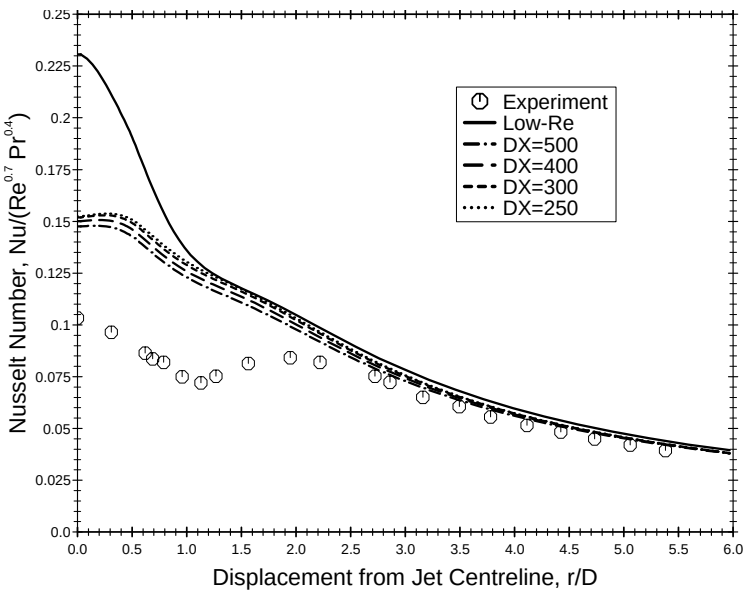

Figure 5.16: Nusselt number profiles obtained for the impinging jet flow using the simplified Chieng & Launder wall function with the linear $k-\varepsilon$ model and standard Yap correction. Solid line: low-Reynolds-number model; broken lines: wall function results for different near-wall cell widths; symbols: experiments of Baughn *et al*. [94]. Normal stress components are included in the cell-averaged production term, $\overline{P_k}$, of the wall function (see Equation 2.49).

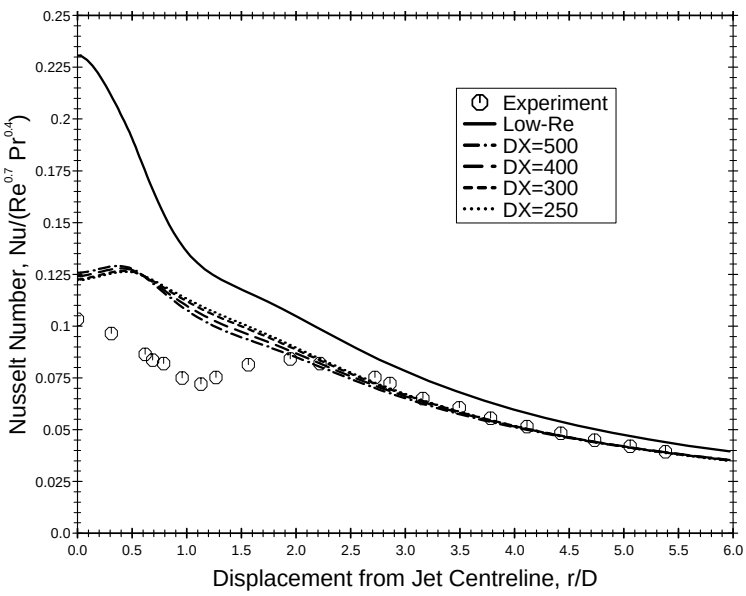

Figure 5.17: Nusselt number profiles obtained for the impinging jet flow using the Chieng & Launder wall function with the linear $k-\varepsilon$ model and standard Yap correction. Solid line: low-Reynolds-number model; broken lines: wall function results for different near-wall cell widths; symbols: experiments of Baughn *et al*. [94]. Normal stress components are included in the cell-averaged production term, $\overline{P_k}$, of the wall function (see Equation 2.49).

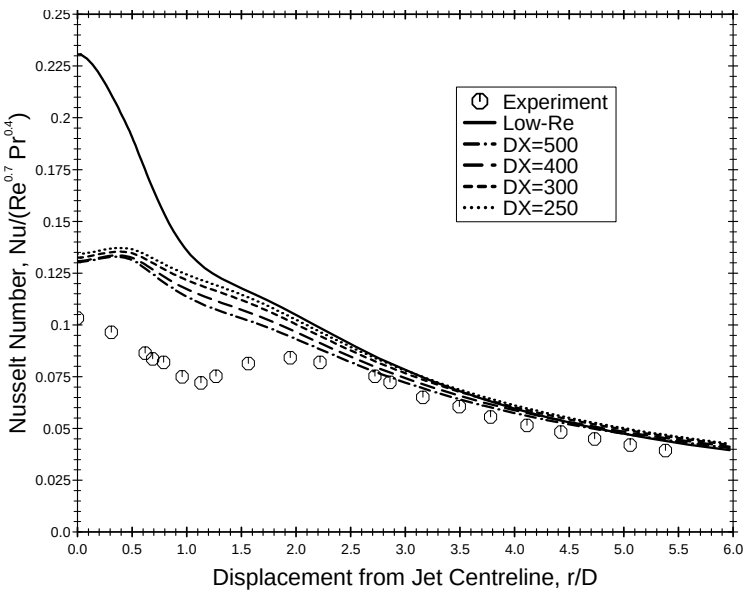

Figure 5.18: Nusselt number profiles obtained for the impinging jet flow using the Johnson & Launder wall function with the linear $k-\varepsilon$ model and standard Yap correction. Solid line: low-Reynolds-number model; broken lines: wall function results for different near-wall cell widths; symbols: experiments of Baughn *et al*. [94]. Normal stress components are included in the cell-averaged production term, $\overline{P_k}$, of the wall function (see Equation 2.49).

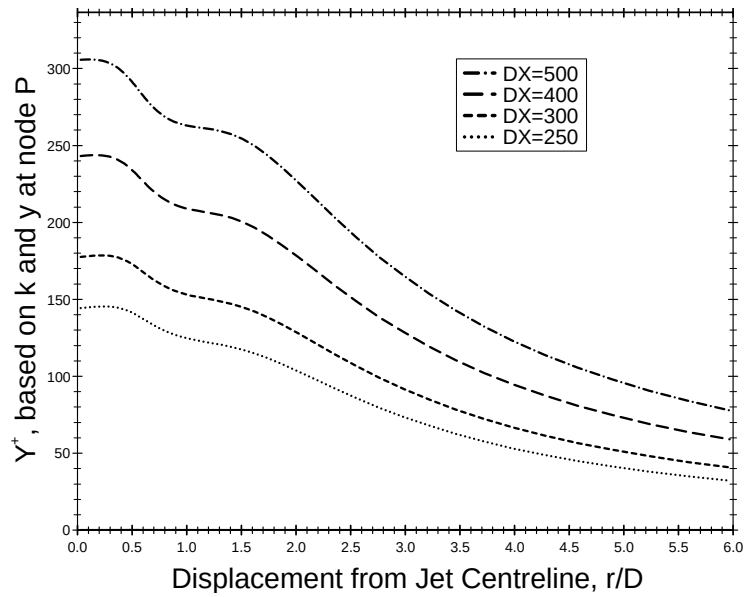

Figure 5.19: Calculated $y^+ \left(= c_\mu^{1/4} k_P^{1/2} y_P / \nu\right)$ profiles obtained for the impinging jet flow using the Chieng & Launder wall function with the linear $k-\varepsilon$ model and standard Yap correction, corresponding to the Nusselt number profiles shown in Figure 5.17. Broken lines show wall function results for different near-wall cell widths.

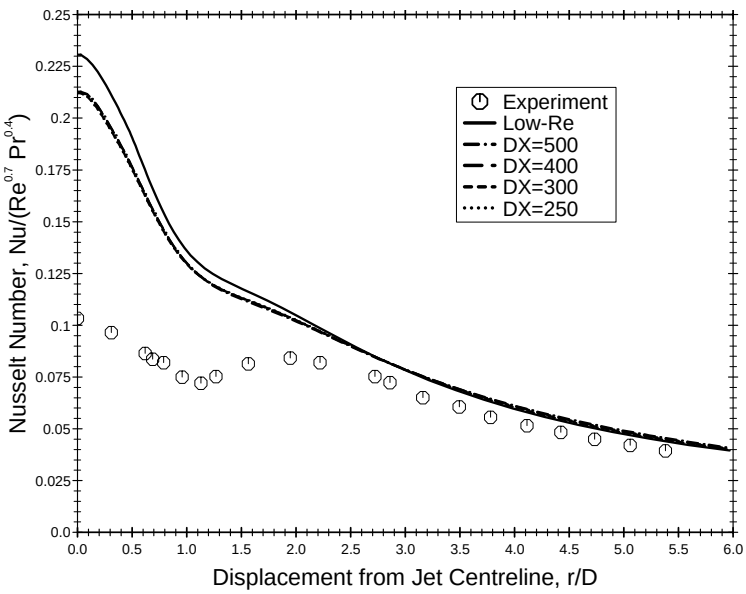

Figure 5.20: Nusselt number profiles obtained for the impinging jet flow using the UMIST-*N* wall function with the linear $k-\varepsilon$ model and standard Yap correction. Solid line: low-Reynolds-number model; broken lines: wall function results for different near-wall cell widths; symbols: experiments of Baughn *et al*. [94].

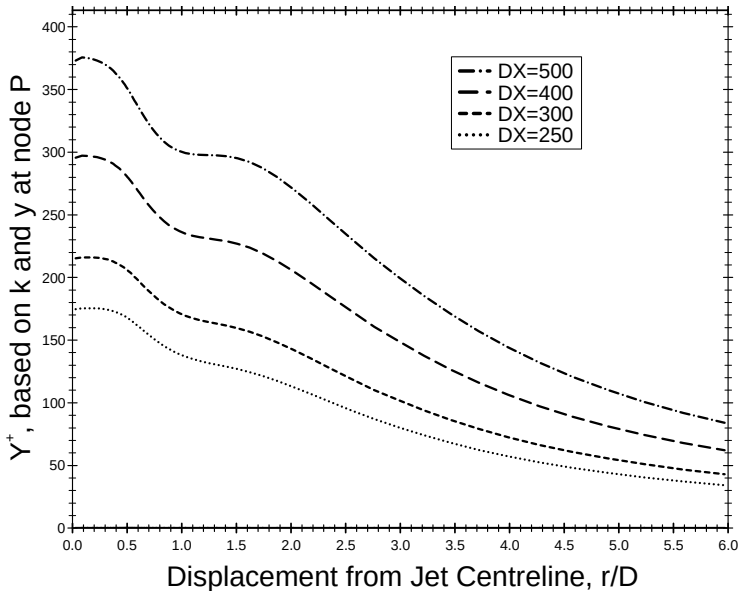

Figure 5.21: Calculated $y^+ \left(= c_\mu^{1/4} k_P^{1/2} y_P / \nu\right)$ profiles obtained for the impinging jet flow using the UMIST-*N* wall function with the linear $k-\varepsilon$ model and standard Yap correction, corresponding to the Nusselt number profiles shown in Figure 5.20. Broken lines show wall function results for different near-wall cell widths.

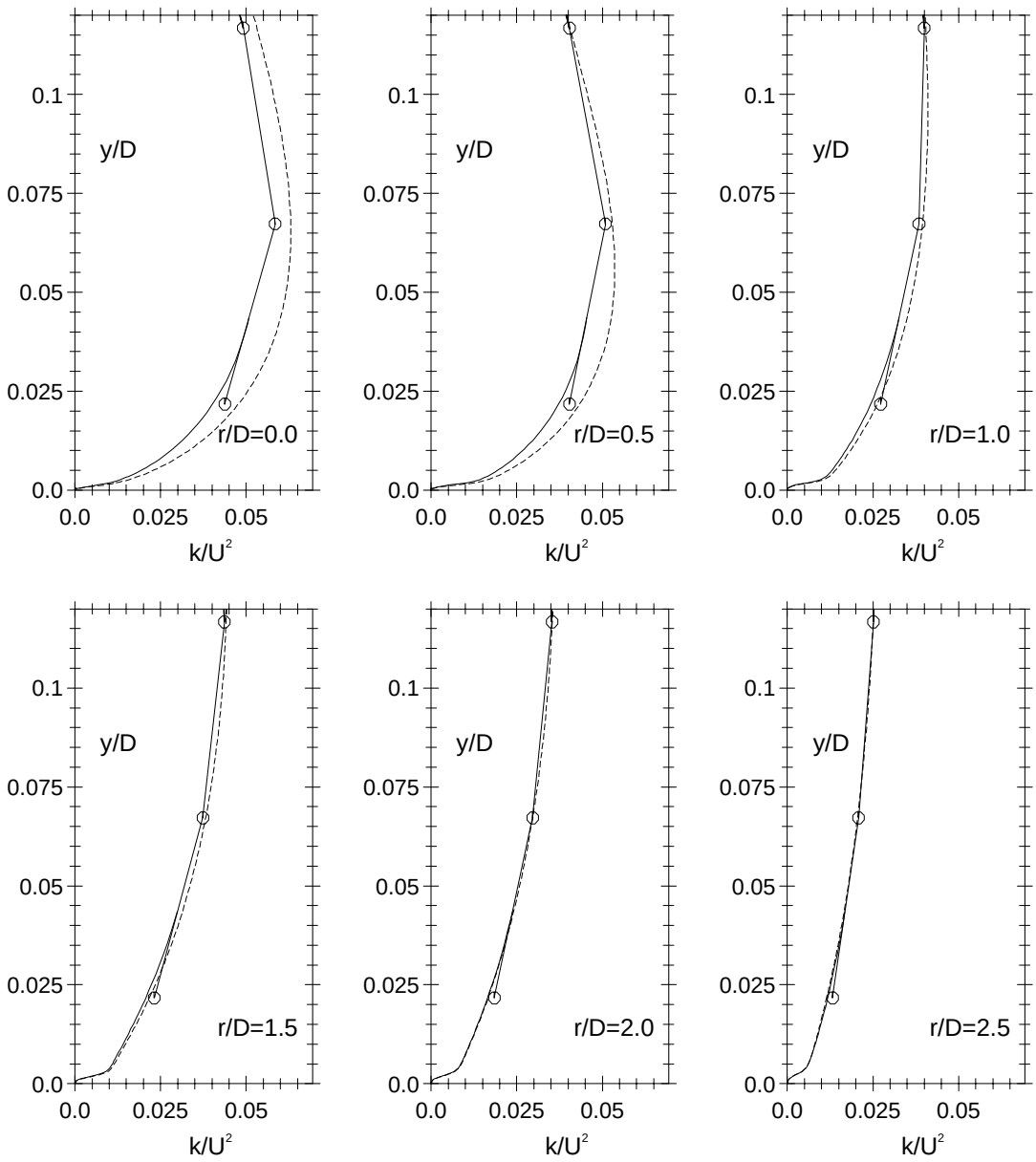

Figure 5.22: Turbulent kinetic energy profiles in the near-wall region (including the subgrid) at 6 different radial positions measured from the axis of the impinging jet, obtained using the linear $k-\varepsilon$ model and standard Yap correction. —-: UMIST-N wall function with near wall cell size $DX = 250$ and grid arrangement as shown in Figure 5.9; - - -: low-Reynolds-number model; symbols: main-grid node values in the wall-function calculation.

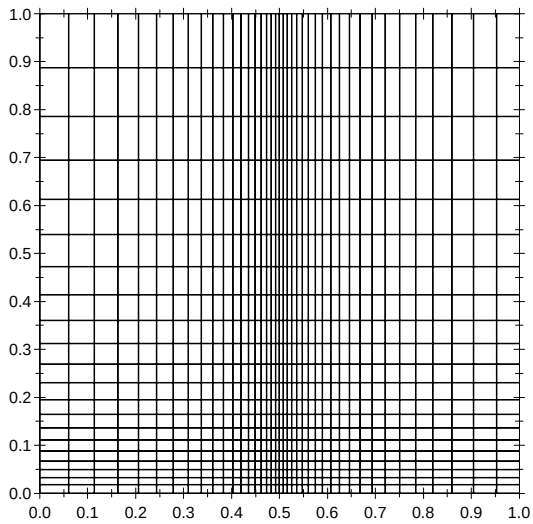

Figure 5.23: Close-up of the wall-bounded region of the impinging jet flow using the high-Reynolds-number 51×70 grid with near-wall cell size $DX = 100$.

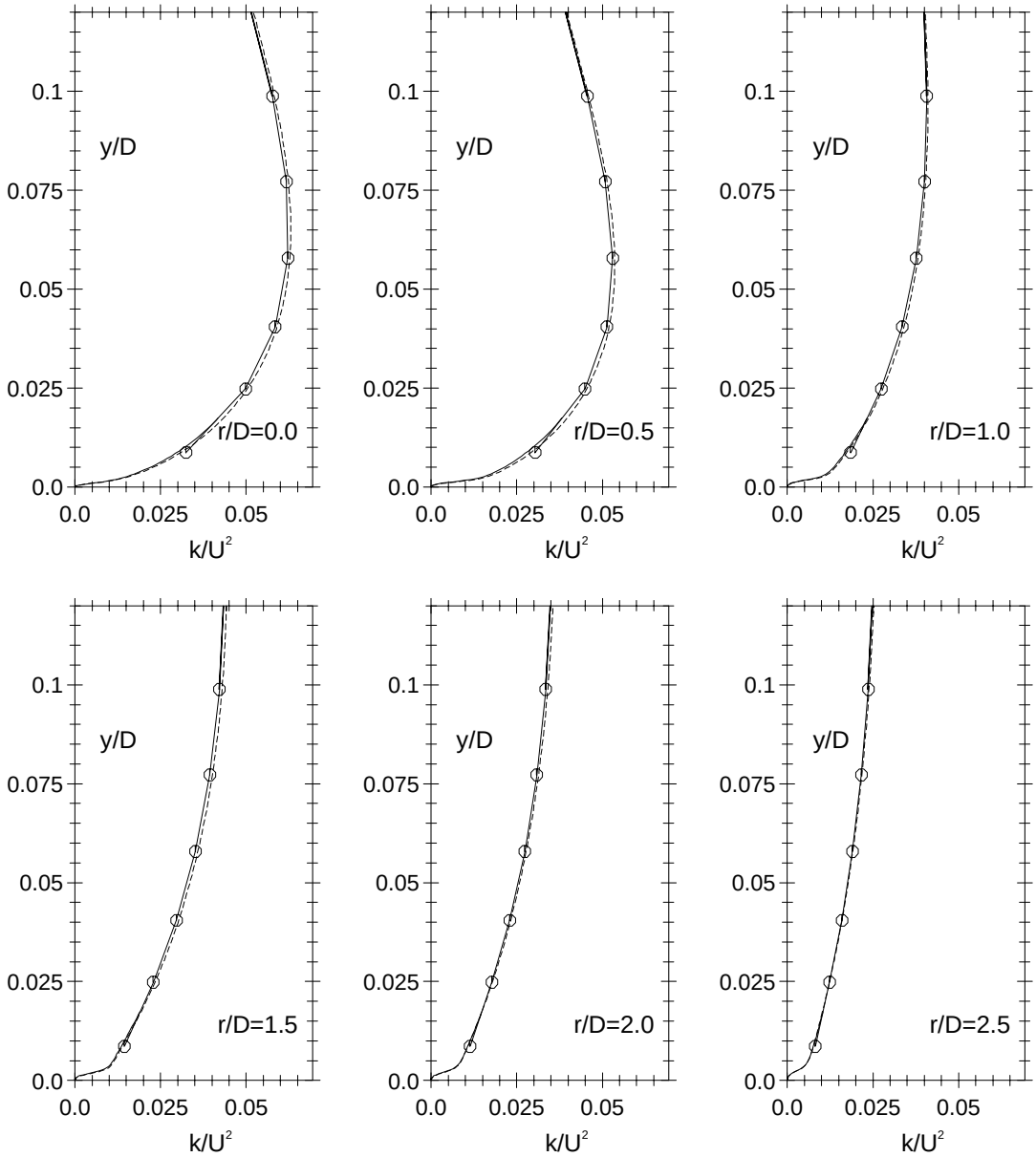

Figure 5.24: Turbulent kinetic energy profiles in the near-wall region (including the subgrid) at 6 different radial positions measured from the axis of the impinging jet, obtained using the linear $k-\varepsilon$ model and standard Yap correction. —-: UMIST-N wall function with near wall cell size $DX = 100$ and grid arrangement as shown in Figure 5.23; - - -: low-Reynolds-number model; symbols: main-grid node values in the wall-function calculation.

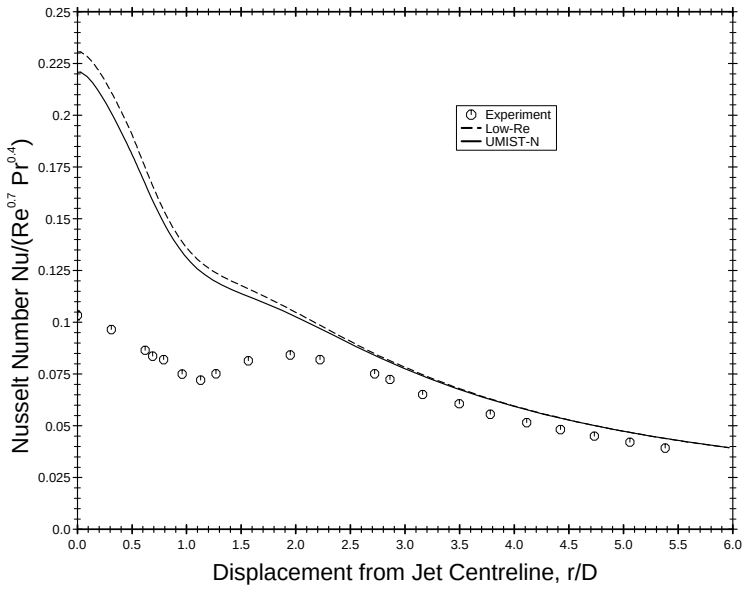

Figure 5.25: Nusselt number profiles obtained for the impinging jet flow with the linear $k-\varepsilon$ model and standard Yap correction. Dashed line: low-Reynolds-number model; solid line: UMIST-*N* wall function result obtained with near wall cell size $DX = 100$ and grid arrangement as shown in Figure 5.23. Symbols: experiments of Baughn *et al*. [94].

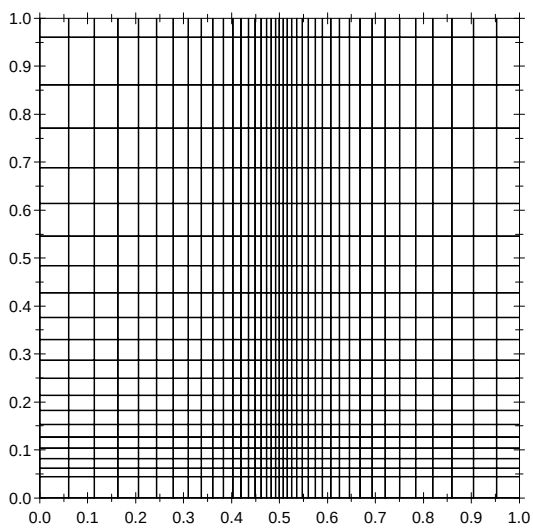

Figure 5.26: Close-up of the wall-bounded region in the impinging jet flow using the high-Reynolds-number 51×70 grid with near-wall cell size $DX = 250$.

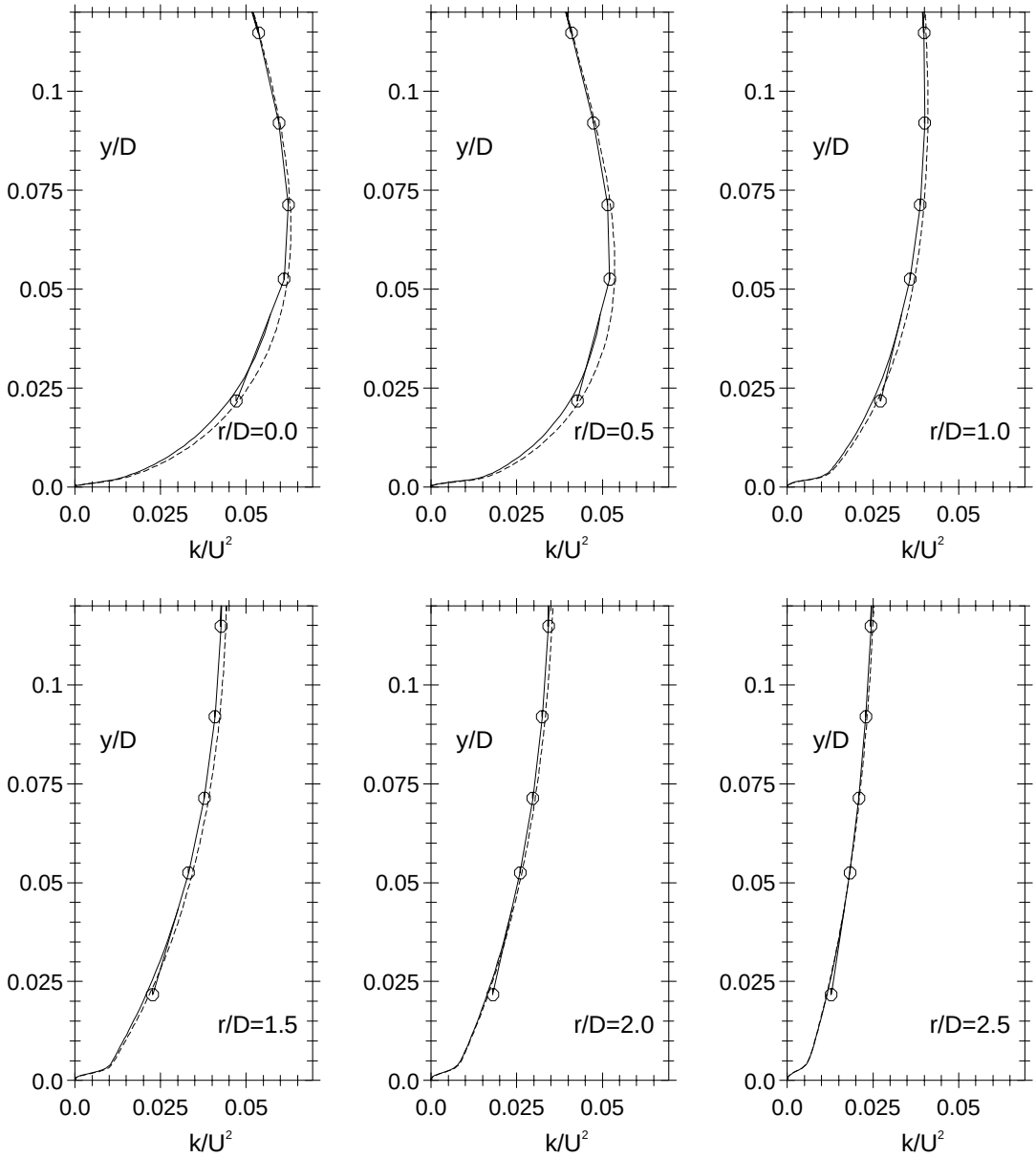

Figure 5.27: Turbulent kinetic energy profiles in the near-wall region (including the subgrid) at 6 different radial positions measured from the axis of the impinging jet, obtained using the linear $k-\varepsilon$ model and standard Yap correction. —-: UMIST-N wall function with near wall cell size $DX = 250$ and grid arrangement as shown in Figure 5.26; - - -: low-Reynolds-number model; symbols: main-grid node values in the wall-function calculation.

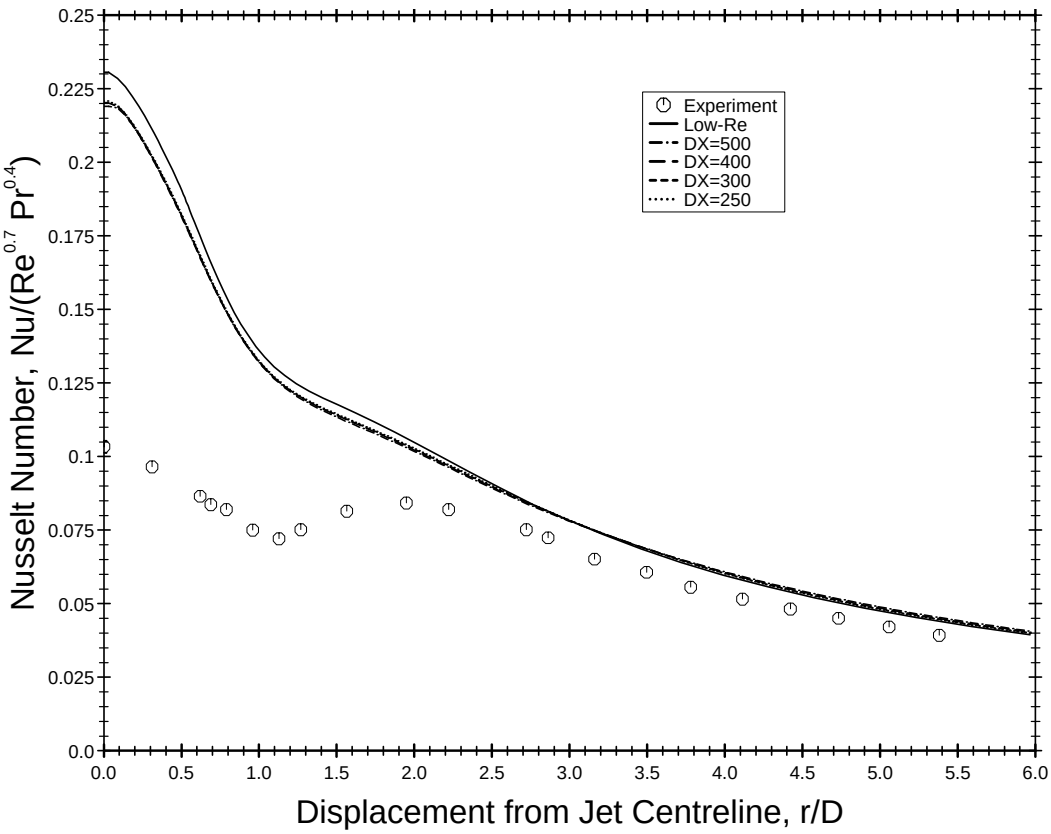

Figure 5.28: Nusselt number profiles obtained for the impinging jet flow using the linear $k-\varepsilon$ model and standard Yap correction. Solid line: low-Reynolds-number model; broken lines: UMIST-*N* wall function results for different near-wall cell widths with the grid arrangement outside the near-wall cell as shown in Figure 5.26 for $DX = 250$; symbols: experiments of Baughn *et al*. [94].

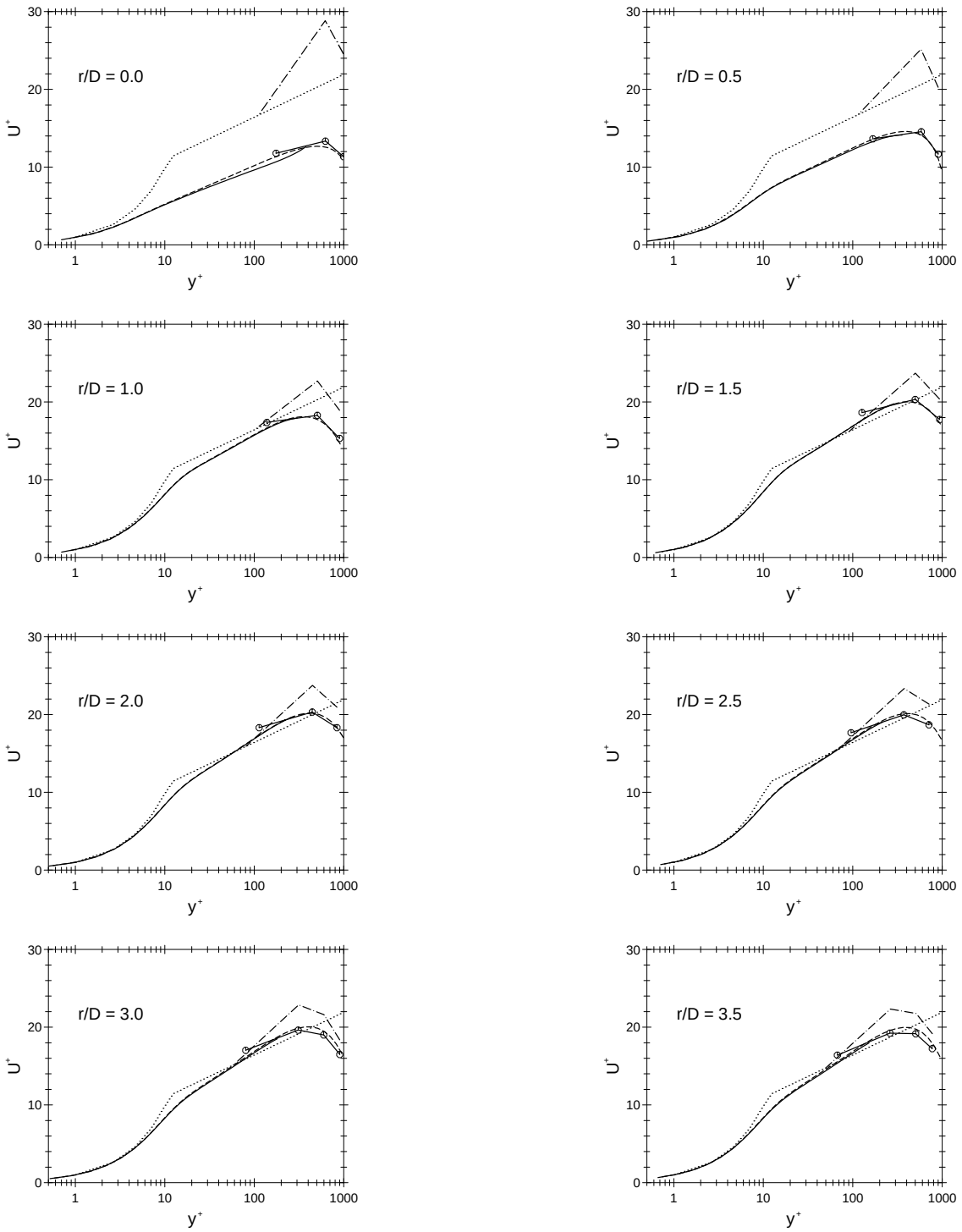

Figure 5.29: Semi-logarithmic velocity profiles for the impinging jet flow at 8 radial locations. —⊖—: UMIST-*N* wall function (circles indicate the position of main-grid nodes); – – –: low-*Re* model; – . –: Chieng & Launder wall function; ....: "universal" log-law. All results shown used the linear $k-\varepsilon$ model and standard Yap correction. Wall function calculations used the $DX = 250$ grid shown in Figure 5.9. Results shown for $r/D = 0$ are taken at the node adjacent to the axis of symmetry. Equation (2.44) is used to define U^+ and y^+.

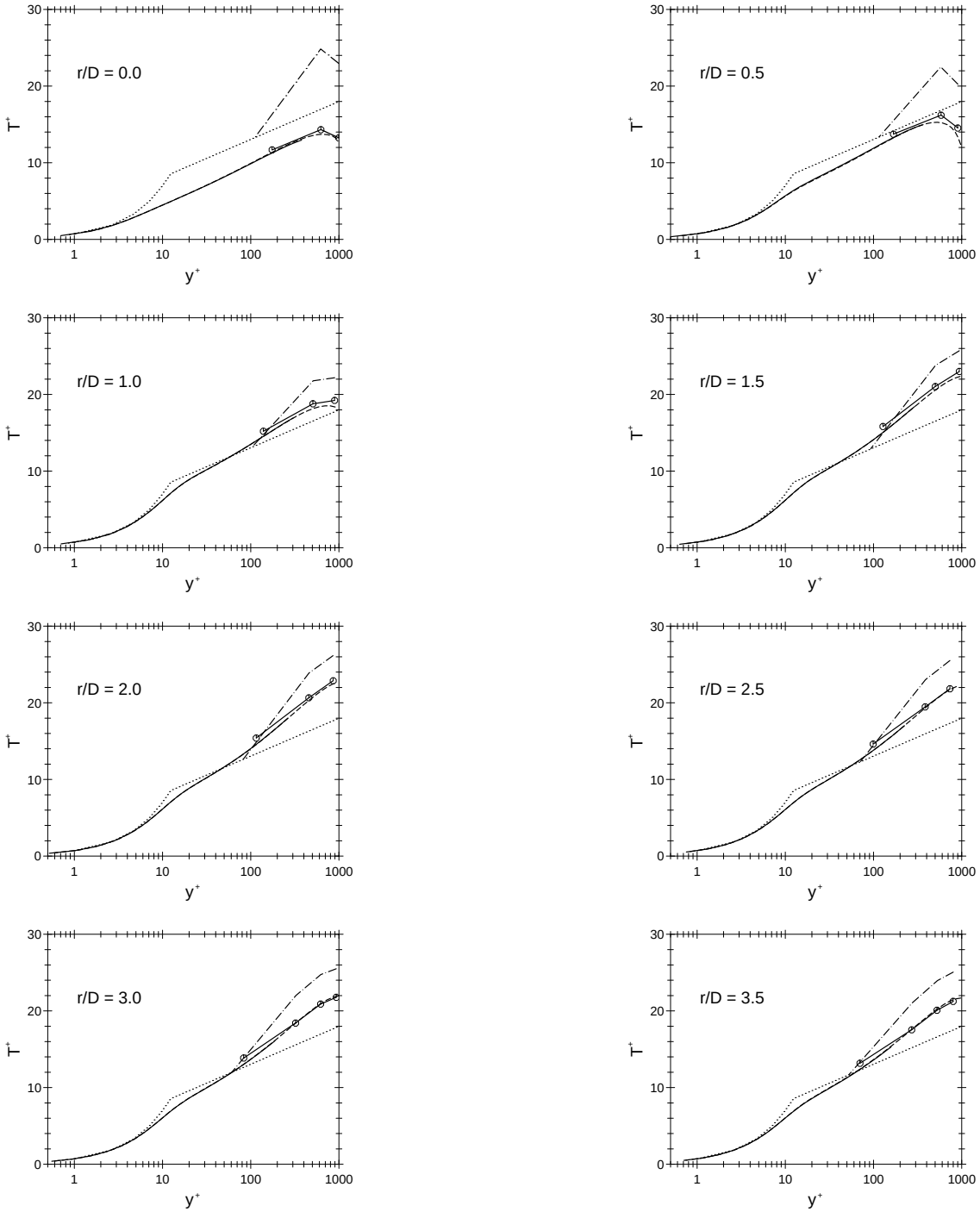

Figure 5.30: Semi-logarithmic temperature profiles for the impinging jet flow at 8 radial locations. —⊖—: UMIST-N wall function (circles indicate the position of main-grid nodes); – – –: low-Re model; – . –: Chieng & Launder wall function; ....: "universal" log-law. All results shown used the linear $k-\varepsilon$ model and standard Yap correction. Wall function calculations were performed using the $DX = 250$ grid shown in Figure 5.9. Results shown for $r/D = 0$ are taken at the node adjacent to the axis of symmetry. The friction velocity used to define y^+ was found from $U_\tau = c_\mu^{1/4} k^{1/2}$.

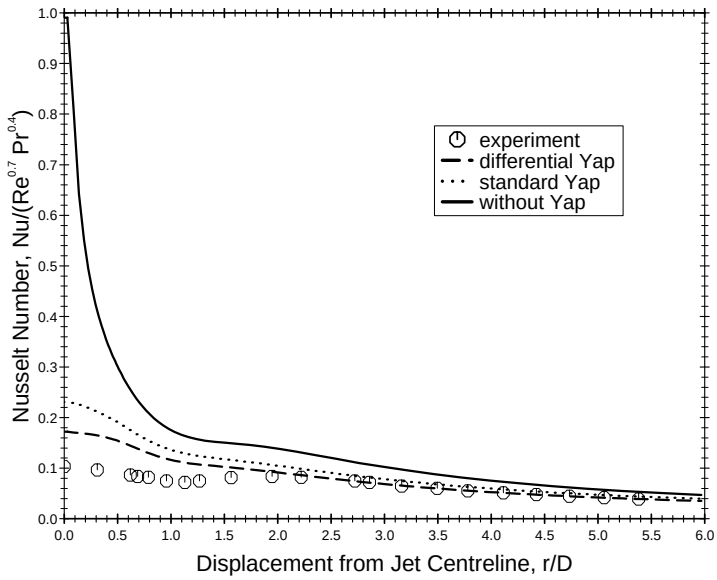

Figure 5.31: Nusselt number profiles for the impinging jet flow obtained using the low-*Re* linear $k-\varepsilon$ model without any Yap correction, with the standard Yap correction (Equation 2.16) and with the differential Yap correction (Equation 2.17). Symbols: experiments of Baughn *et al*. [94].

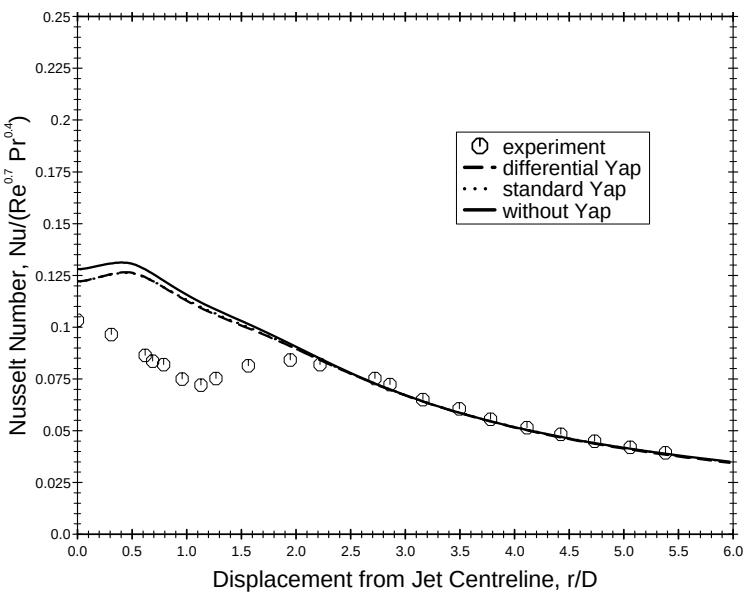

Figure 5.32: Nusselt number profiles for the impinging jet flow obtained using the linear $k-\varepsilon$ model and the Chieng & Launder wall function without any Yap correction, with the standard Yap correction (Equation 2.16) and with the differential Yap correction (Equation 2.17). The standard and differential Yap correction results are practically identical. The wall function grid used a near-wall cell size $DX = 250$. Experimental data points are from of Baughn *et al*. [94].

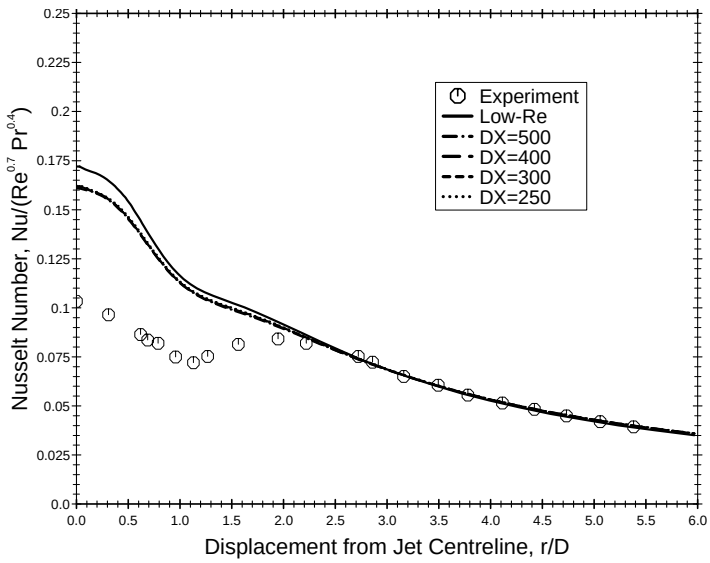

Figure 5.33: Nusselt number profiles for the impinging jet obtained using the linear $k-\varepsilon$ model and the differential Yap correction (Equation 2.17). Solid line: low-Reynolds-number model; broken lines: UMIST-*N* wall function results for different near-wall cell widths; symbols: experiments of Baughn *et al*. [94].

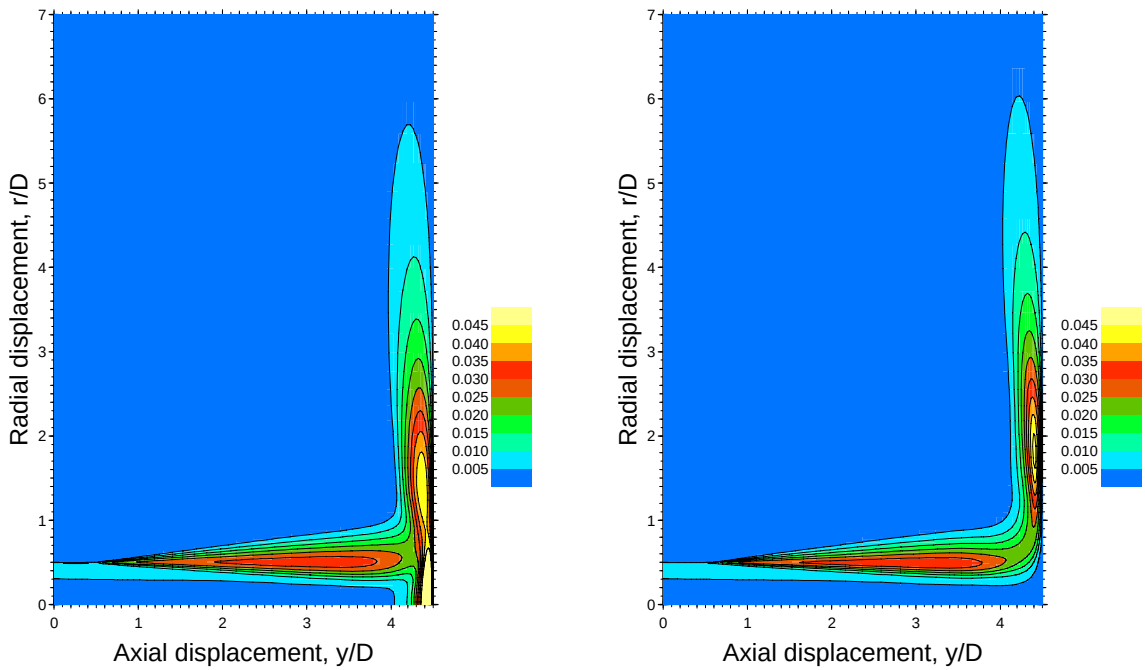

Figure 5.34: Contour plots of the dimensionless turbulent kinetic energy $\left(k/U_{bulk}^2\right)$ for the impinging jet flow obtained using the low-*Re* linear $k-\varepsilon$ model (left) and the low-*Re* NLEVM (right). Axial displacement is measured from the entrainment boundary, i.e. the wall is located at $y/D = 4.5$.

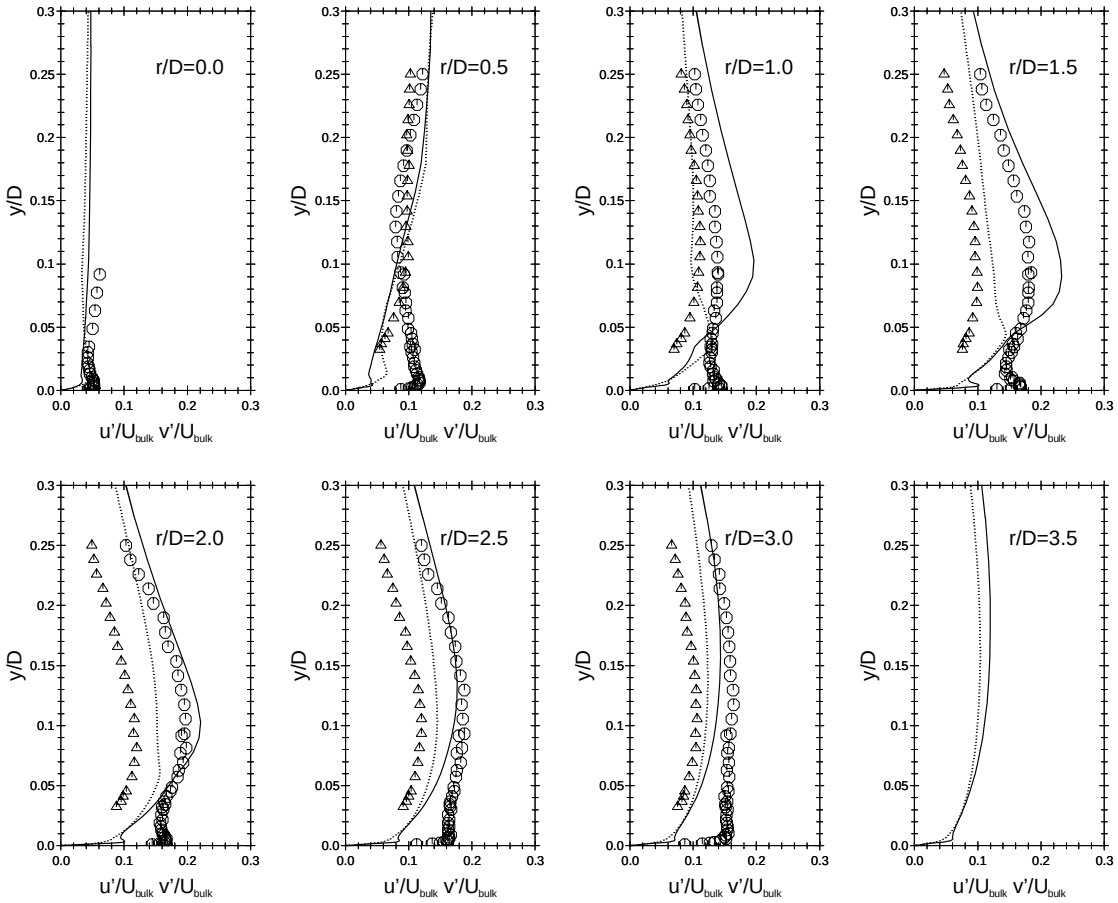

Figure 5.35: Radial (wall-parallel) and axial (wall-normal) RMS velocity components for the impinging jet flow at 8 radial positions using the NLEVM with the differential Yap correction and the c_μ function of Equation (2.36). Lines represent the low-*Re* model predictions and symbols the experimental data of Cooper *et al*. [95]. —- and ⊖: radial u' component; ..... and △: axial v' component.

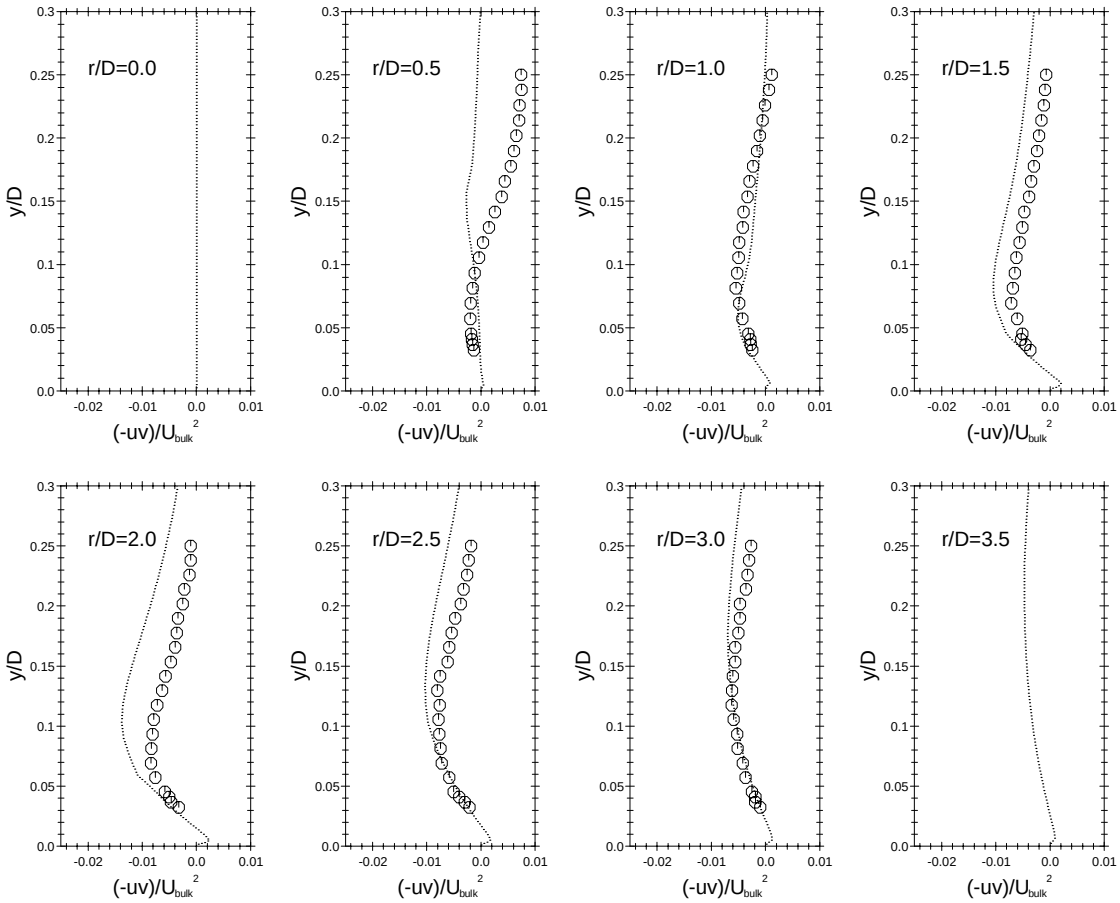

Figure 5.36: Turbulent shear stress (in the axial-radial plane) for the impinging jet flow at 8 radial positions using the NLEVM with the differential Yap correction and the c_μ function of Equation (2.36). Lines represent the low-*Re* model predictions and symbols the experimental data of Cooper *et al*. [95].

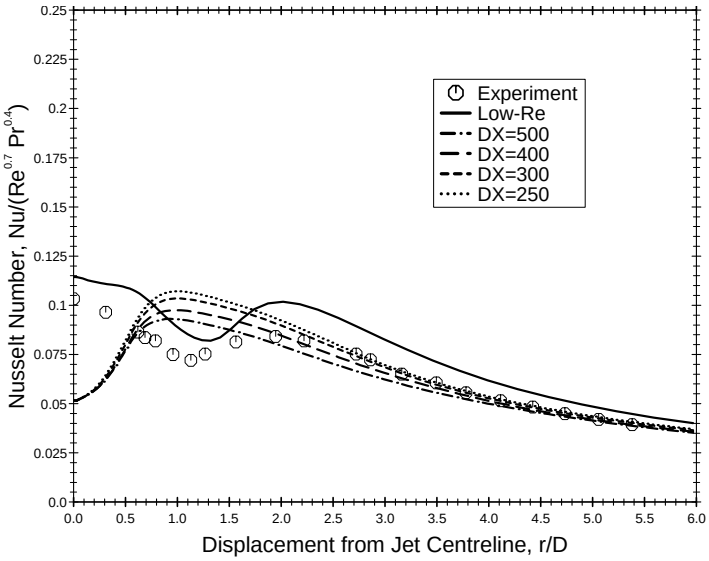

Figure 5.37: Nusselt number profiles obtained for the impinging jet flow using the Launder & Spalding (TEAM) wall function with the non-linear $k-\varepsilon$ model, the c_μ function of Equation (2.36) and differential Yap correction. Solid line: low-Reynolds-number model; broken lines: wall function results for different near-wall cell widths; symbols: experiments of Baughn *et al.* [94]. Normal stress components are included in the cell-averaged production term, $\overline{P_k}$, of the wall function (see Equation 2.49).

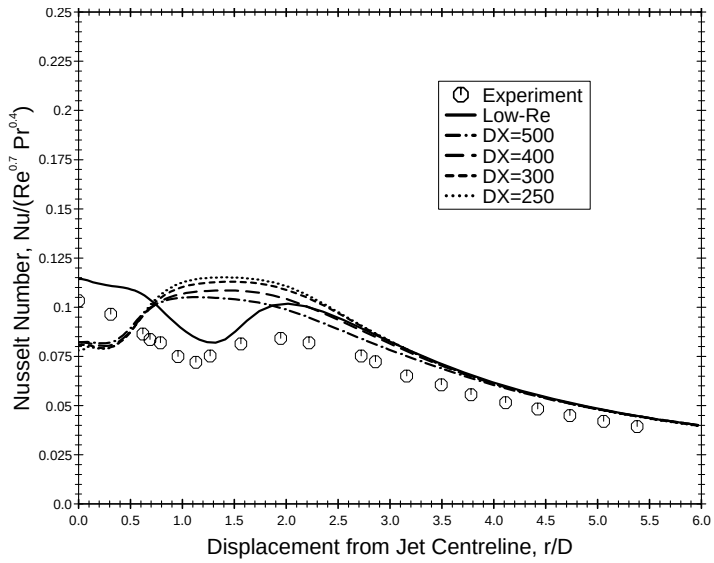

Figure 5.38: Nusselt number profiles obtained for the impinging jet flow using the simplified Chieng & Launder wall function with the non-linear $k-\varepsilon$ model, the c_μ function of Equation (2.36) and differential Yap correction. Solid line: low-Reynolds-number model; broken lines: wall function results for different near-wall cell widths; symbols: experiments of Baughn *et al*. [94]. Normal stress components are included in the cell-averaged production term, $\overline{P_k}$, of the wall function (see Equation 2.49).

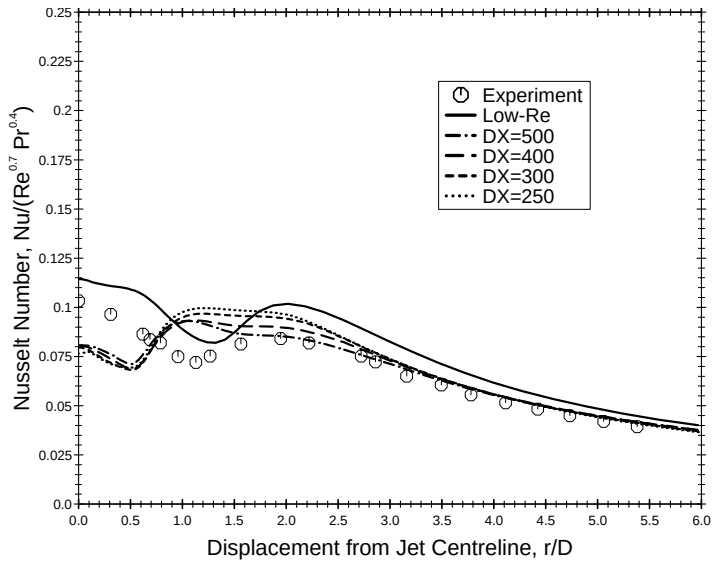

Figure 5.39: Nusselt number profiles obtained for the impinging jet flow using the Chieng & Launder wall function with the non-linear $k-\varepsilon$ model, the c_μ function of Equation (2.36) and differential Yap correction. Solid line: low-Reynolds-number model; broken lines: wall function results for different near-wall cell widths; symbols: experiments of Baughn *et al*. [94]. Normal stress components are included in the cell-averaged production term, $\overline{P_k}$, of the wall function (see Equation 2.49).

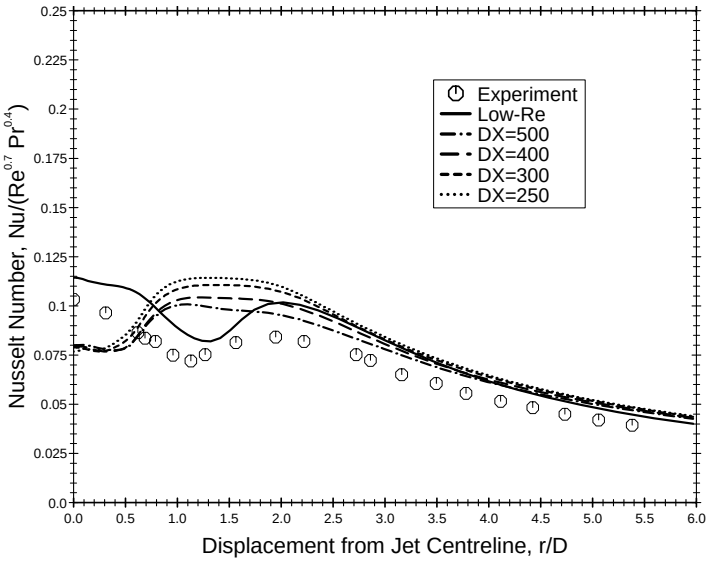

Figure 5.40: Nusselt number profiles obtained for the impinging jet flow using the Johnson & Launder wall function with the non-linear $k-\varepsilon$ model, the c_μ function of Equation (2.36) and differential Yap correction. Solid line: low-Reynolds-number model; broken lines: wall function results for different near-wall cell widths; symbols: experiments of Baughn *et al*. [94]. Normal stress components are included in the cell-averaged production term, $\overline{P_k}$, of the wall function (see Equation 2.49).

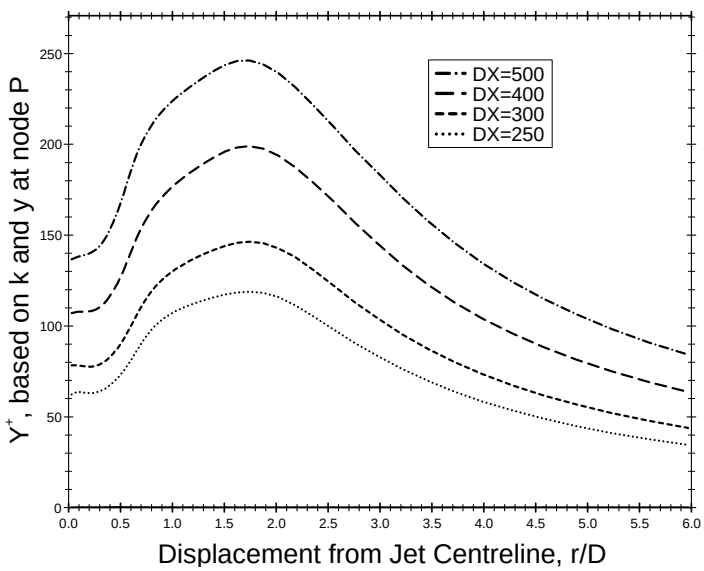

Figure 5.41: Calculated $y^+\left(=c_\mu^{1/4}k_P^{1/2}y_P/\nu\right)$ profiles obtained for the impinging jet flow using the Chieng & Launder wall function with the non-linear $k-\varepsilon$ model, the c_μ function of Equation (2.36) and differential Yap correction, corresponding to the Nusselt number profiles shown in Figure 5.39. Broken lines show wall function results for different near-wall cell widths.

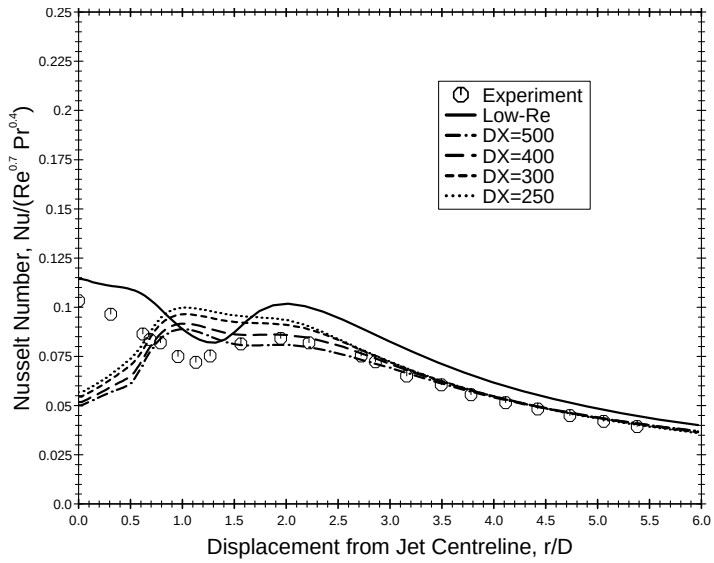

Figure 5.42: Nusselt number profiles obtained for the impinging jet flow using the Chieng & Launder wall function with the NLEVM of Craft *et al*. [67], the c_μ-function given by Equation (2.36) and the differential Yap correction. Solid line: low-Reynolds-number model; broken lines: wall function results for different near-wall cell widths; symbols: experiments of Baughn *et al*. [94]. Normal stress components are *not* included in the cell-averaged production term, $\overline{P_k}$, of the wall function.

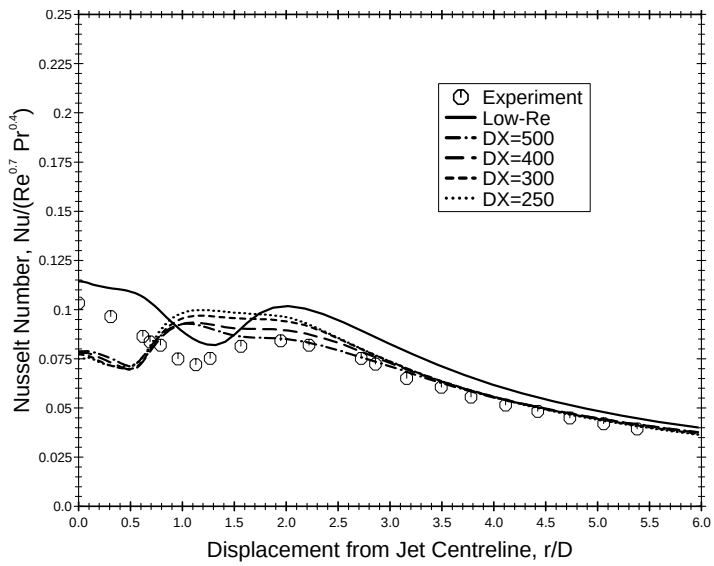

Figure 5.43: Nusselt number profiles obtained for the impinging jet flow using the Chieng & Launder wall function with the NLEVM of Craft *et al*. [67], the c_μ-function given by Equation (2.36) and the differential Yap correction. Solid line: low-Reynolds-number model; broken lines: wall function results for different near-wall cell widths; symbols: experiments of Baughn *et al*. [94]. The cell-averaged production term, $\overline{P_k}$, of the wall function is modified by assuming that the normal stresses vary linearly across the fully-turbulent region of the near-wall cell.

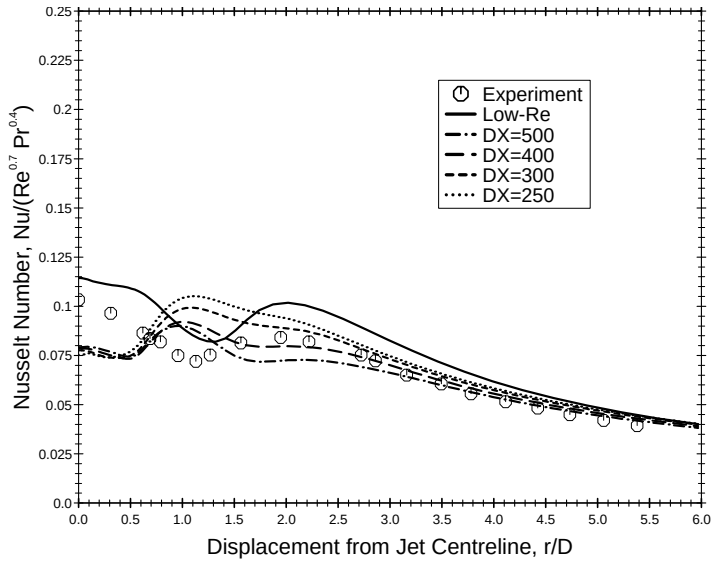

Figure 5.44: Nusselt number profiles obtained for the impinging jet flow using the Chieng & Launder wall function with the NLEVM of Craft *et al*. [67], the c_μ-function given by Equation (2.36) and the differential Yap correction. Solid line: low-Reynolds-number model; broken lines: wall function results for different near-wall cell widths; symbols: experiments of Baughn *et al*. [94]. The cell-averaged production term, $\overline{P_k}$, of the wall function is modified by assuming that the normal stresses vary linearly across the fully-turbulent region of the near-wall cell and that the Reynolds stresses vary according to their wall-limiting behaviour across the viscous sublayer.

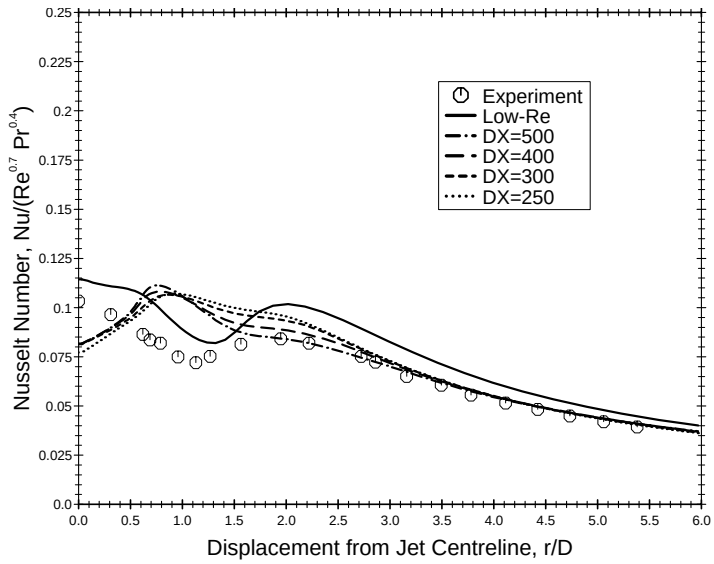

Figure 5.45: Nusselt number profiles obtained for the impinging jet flow using the Chieng & Launder wall function with the NLEVM of Craft *et al*. [67], the c_μ-function given by Equation (2.36) and the differential Yap correction. Solid line: low-Reynolds-number model; broken lines: wall function results for different near-wall cell widths; symbols: experiments of Baughn *et al*. [94]. Wall function results obtained using $\partial U/\partial y$ calculated from the derivative of the log-law in the near-wall cell for the non-linear stress terms and c_μ function.

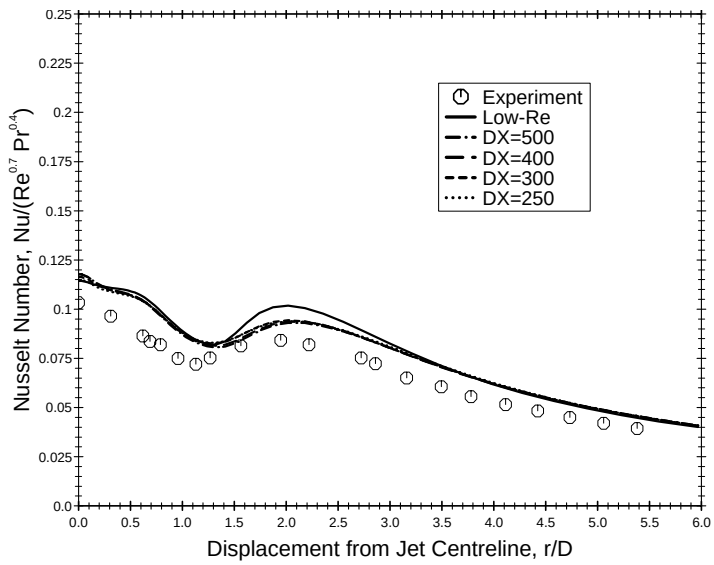

Figure 5.46: Nusselt number profiles obtained for the impinging jet flow using the UMIST-*N* wall function with the NLEVM of Craft *et al*. [67], the c_μ-function given by Equation (2.36) and the differential Yap correction. Solid line: low-Reynolds-number model; broken lines: wall function results for different near-wall cell widths; symbols: experiments of Baughn *et al*. [94].

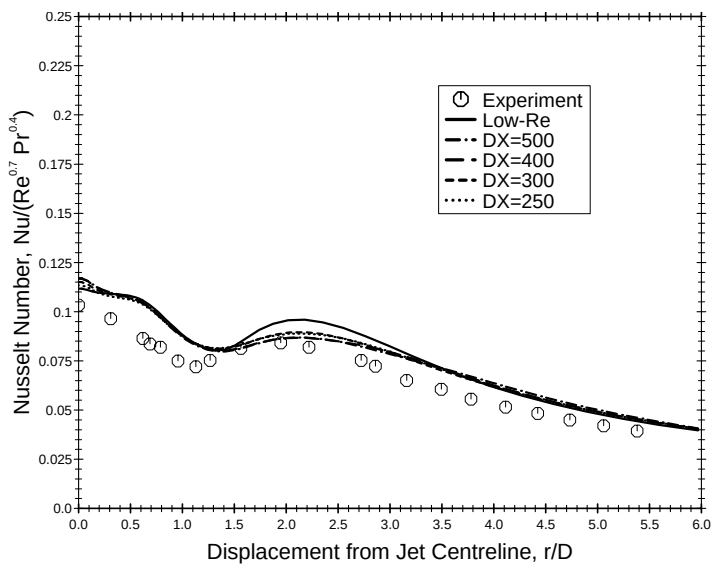

Figure 5.47: Nusselt number profiles obtained for the impinging jet flow using the UMIST-*N* wall function with the NLEVM of Craft *et al*. [30], the c_μ-function given by Equation (2.33) and the differential Yap correction. Solid line: low-Reynolds-number model; broken lines: wall function results for different near-wall cell widths; symbols: experiments of Baughn *et al*. [94].

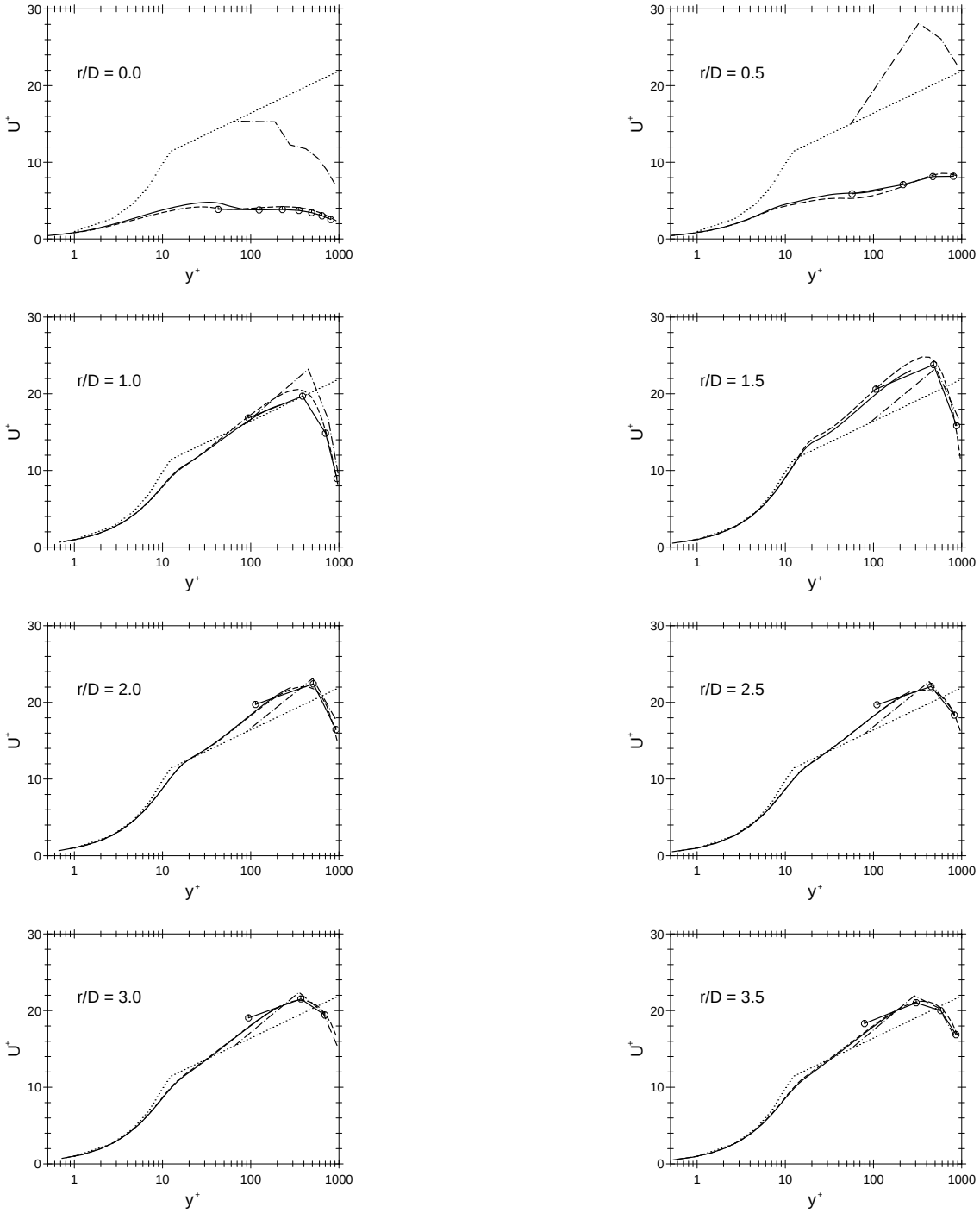

Figure 5.48: Semi-logarithmic velocity profiles for the impinging jet flow at 8 radial locations. —⊖—: UMIST-*N* wall function (circles indicate the position of main-grid nodes); – – –: low-*Re* model; – . –: Chieng & Launder wall function; ....: "universal" log-law. All results shown used the non-linear $k-\varepsilon$ model with the c_μ function given by Equation (2.36) and differential Yap correction. Wall function calculations used the $DX = 250$ grid shown in Figure 5.9. Results shown for $r/D = 0$ are taken at the node adjacent to the axis of symmetry. Equation (2.44) is used to define U^+ and y^+.

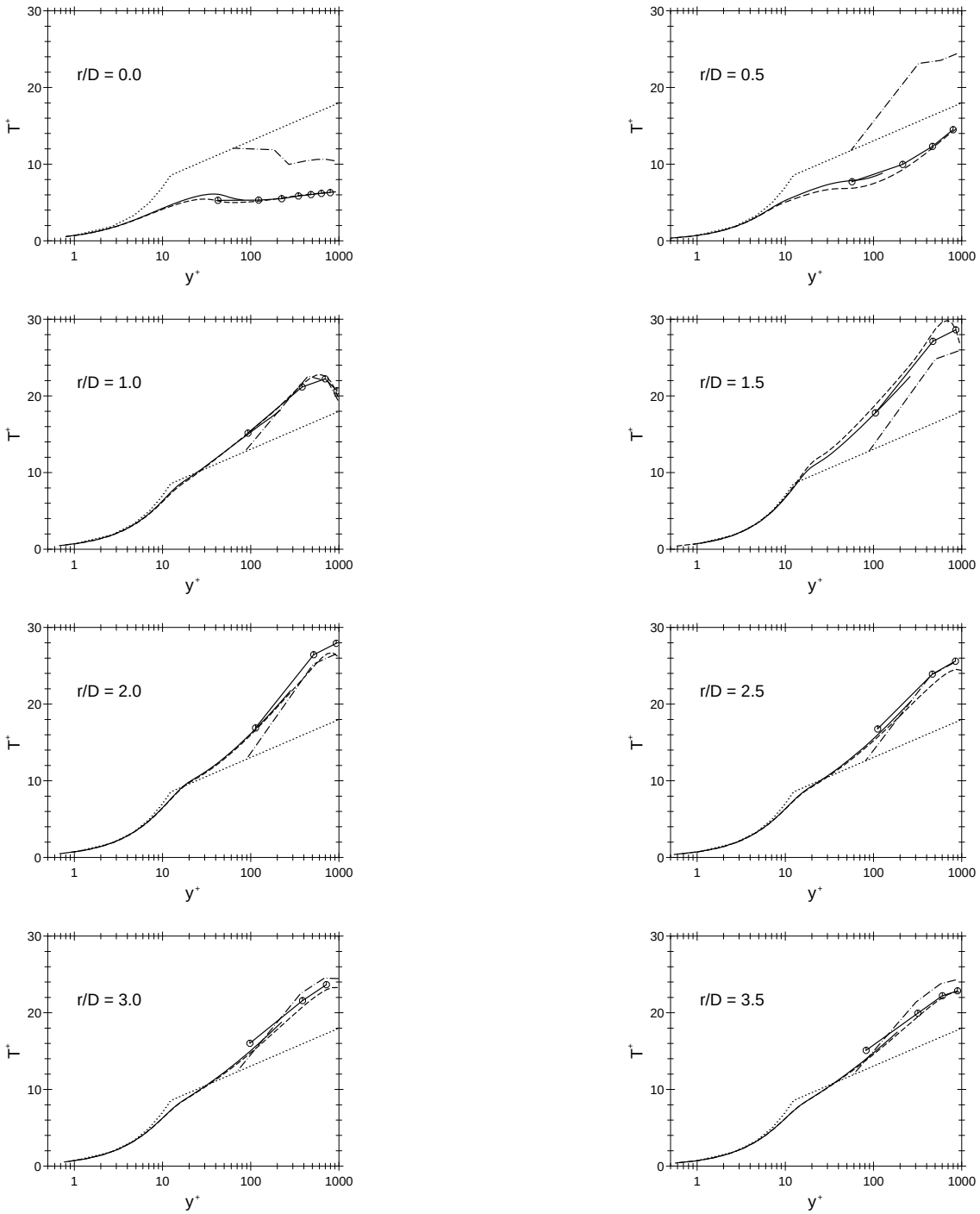

Figure 5.49: Semi-logarithmic temperature profiles for the impinging jet flow at 8 radial locations. —⊖—: UMIST-N wall function (circles indicate the position of main-grid nodes); – – –: low-Re model; – . –: Chieng & Launder wall function; .....: "universal" log-law. All results shown used the non-linear $k-\varepsilon$ model with the c_μ function given by Equation (2.36) and differential Yap correction. Wall function calculations were performed using the $DX = 250$ grid shown in Figure 5.9. Results shown for $r/D = 0$ are taken at the node adjacent to the axis of symmetry. The friction velocity used to define y^+ was found from $U_\tau = c_\mu^{1/4} k^{1/2}$.

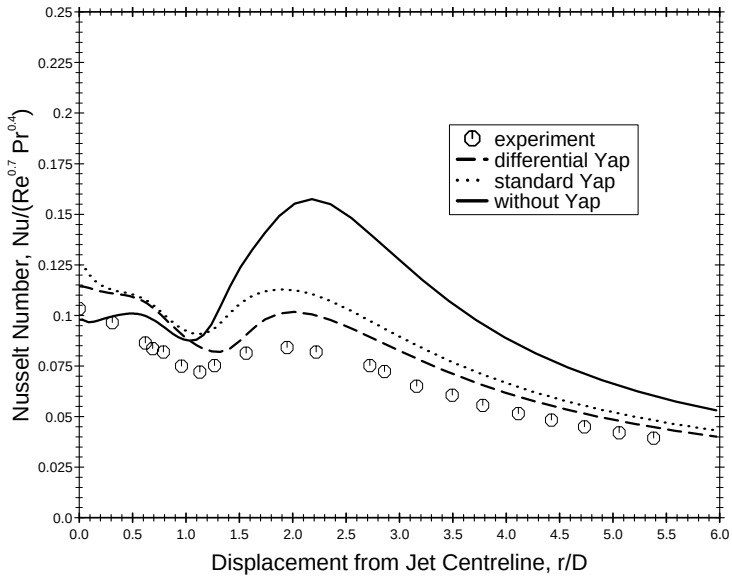

Figure 5.50: Nusselt number profiles for the impinging jet obtained using the low-*Re* NLEVM of Craft *et al*. [67] and the c_μ-function given by Equation (2.36) without any Yap correction, with the standard Yap correction (Equation 2.16) and with the differential Yap correction (Equation 2.17). Symbols: experiments of Baughn *et al*. [94].

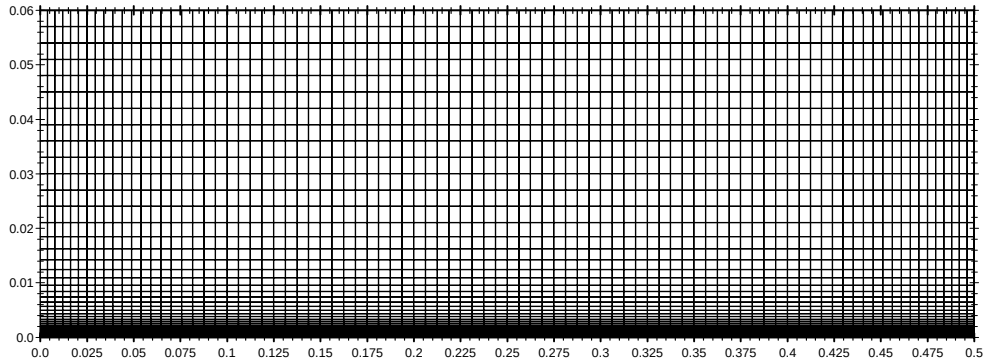

Figure 6.2: Low-Reynolds-number 90×70 (radial$\times$axial) grid used in the free-disc flow.

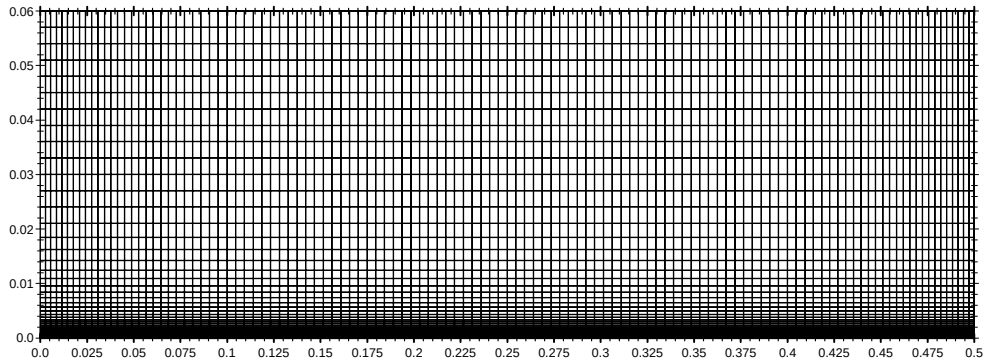

Figure 6.3: Low-Reynolds-number 120×70 (radial$\times$axial) grid used in the free-disc flow.

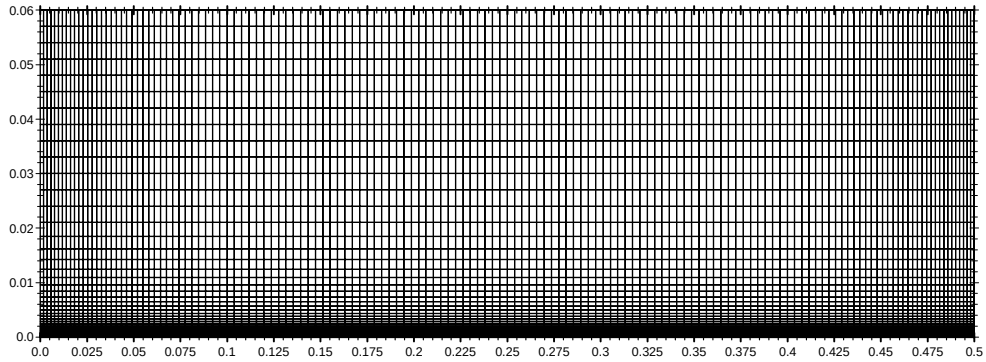

Figure 6.4: Low-Reynolds-number 150×70 (radial$\times$axial) grid used in the free-disc flow.

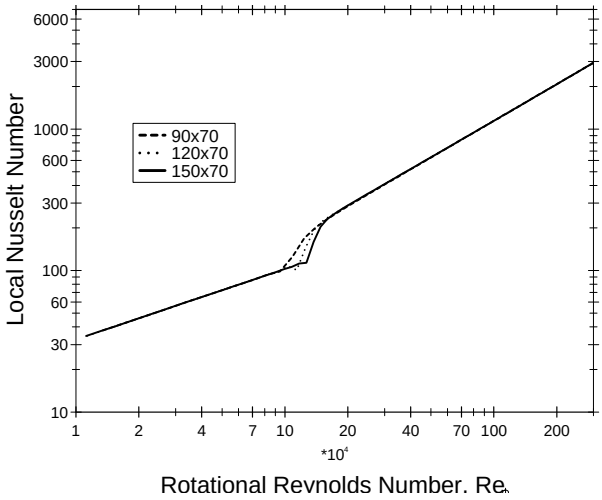

Figure 6.5: Predicted Nusselt number in the free-disc flow with the low-*Re* linear $k-\varepsilon$ model using three different radial grid densities; - - -: 90×70 grid; .....: 120×70 grid; ——: 150×70 grid.

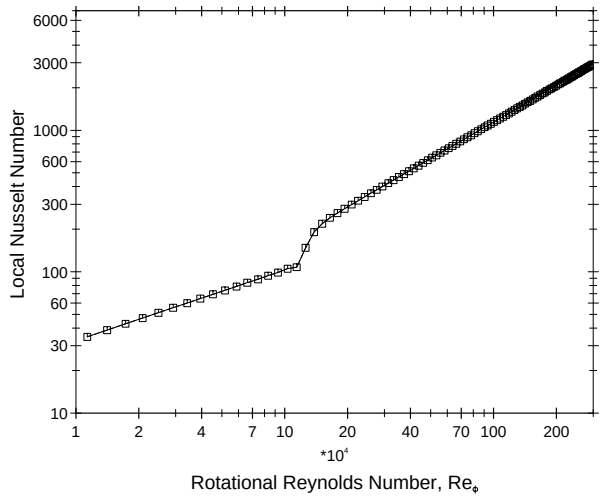

Figure 6.6: Predicted Nusselt number in the free-disc flow with the low-*Re* linear $k-\varepsilon$ model for the 120×70 grid; □: location of radial nodes.

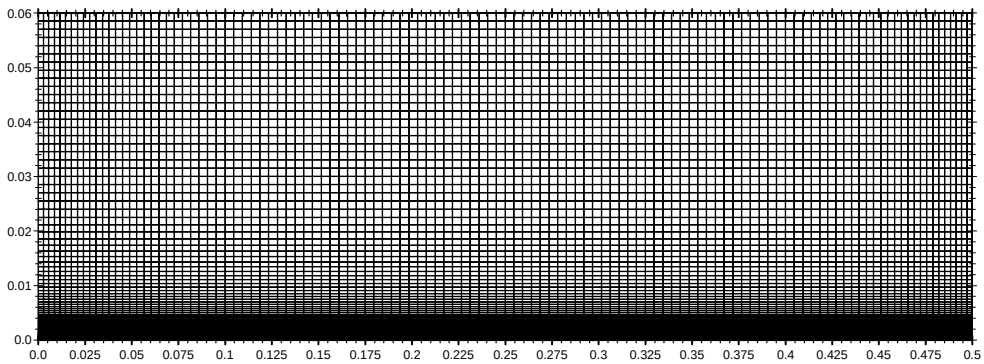

Figure 6.7: Low-Reynolds-number 120×120 grid used in the free-disc flow.

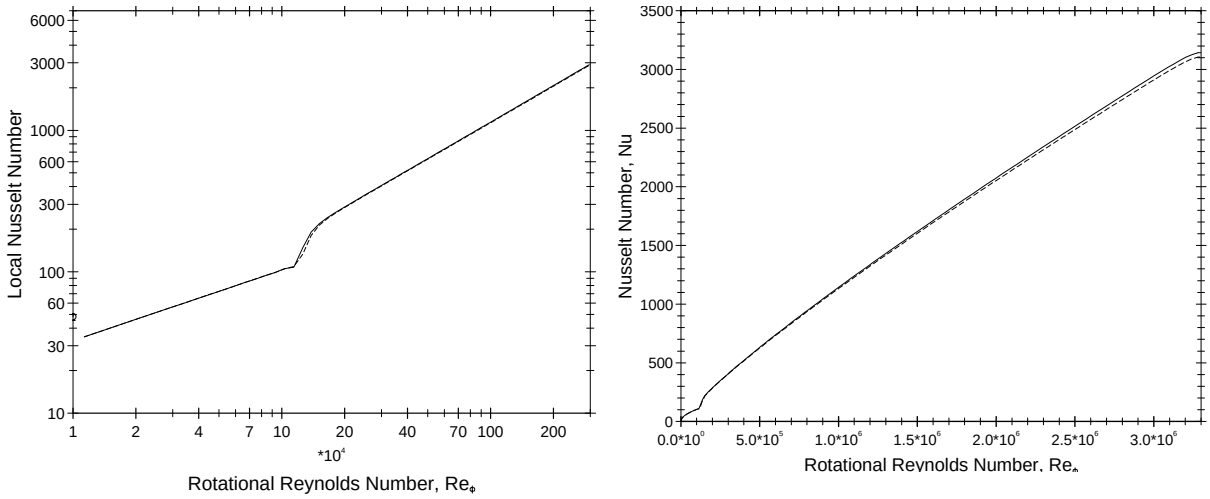

Figure 6.8: Predicted Nusselt number in the free-disc flow with axial refinement of the grid using the low-*Re* Launder & Sharma model; ——: 120×70 (radial$\times$axial) grid; - - -: 120×120 grid; *a*.) semi-log scale (left); *b*.) linear scale (right).

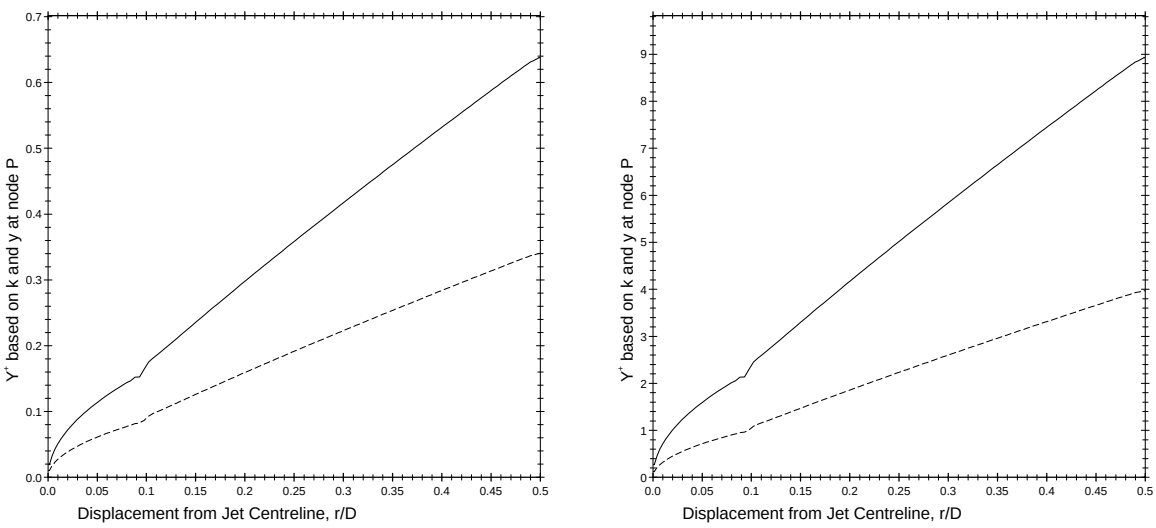

Figure 6.9: Predicted dimensionless wall distance, $y^+ = U_\tau y/\nu$ (where $U_\tau = \sqrt{\tau_{wall}/\rho}$ and τ_{wall} is the resultant wall shear stress), in the free-disc flow with axial refinement of the grid using the low-*Re* Launder & Sharma model; ——: 120×70 (radial$\times$axial) grid; - - -: 120×120 grid; *a*.) wall-adjacent node (left); *b*.) tenth node from the wall (right).

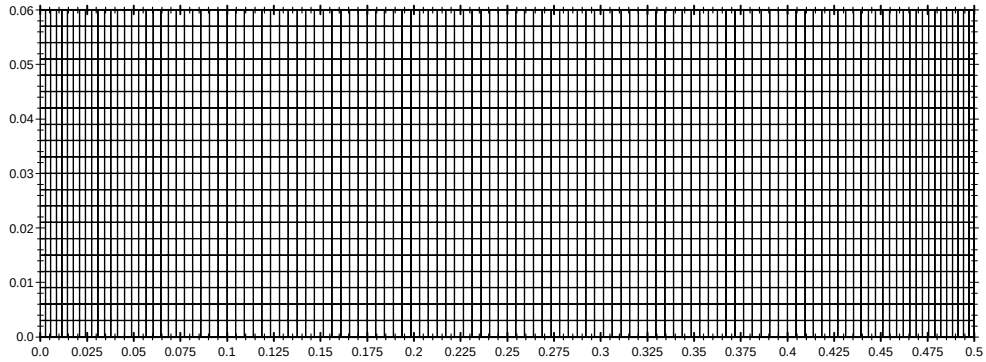

Figure 6.10: High-Reynolds-number 120×22 (radial$\times$axial) grid used in the free-disc flow.

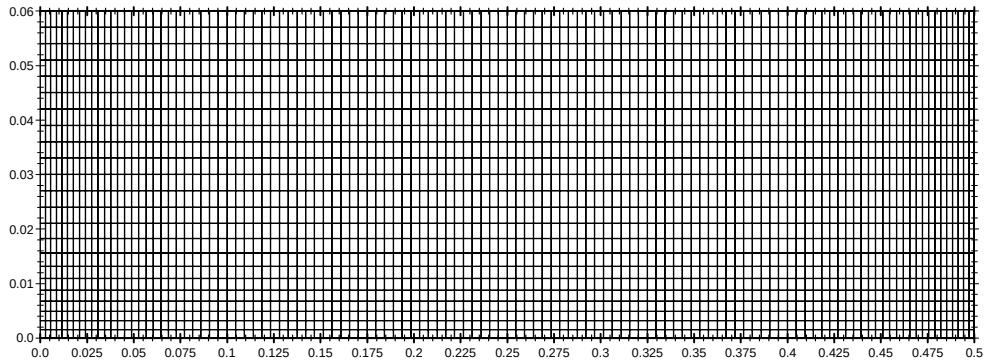

Figure 6.11: High-Reynolds-number 120×25 (radial$\times$axial) grid used in the free-disc flow.

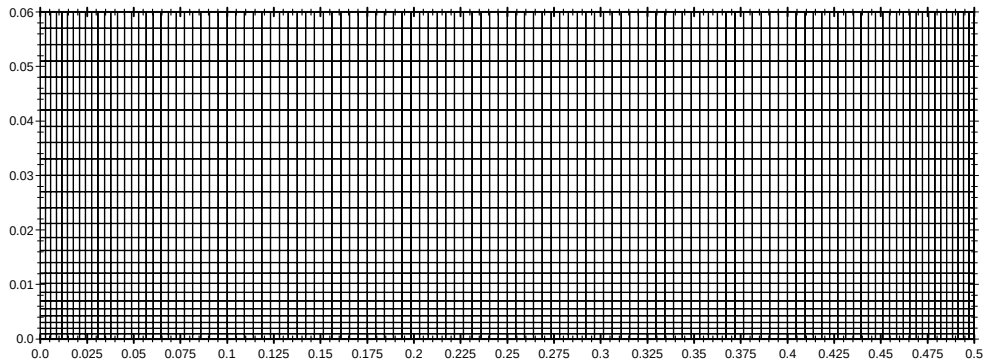

Figure 6.12: High-Reynolds-number 120×28 (radial$\times$axial) grid used in the free-disc flow.

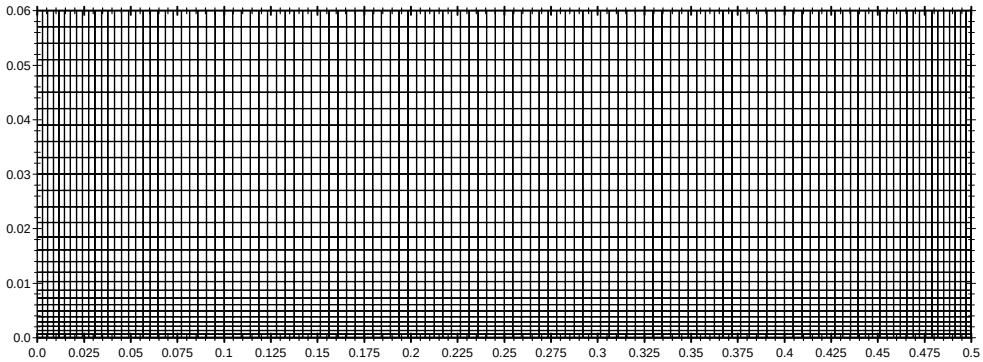

Figure 6.13: High-Reynolds-number 120×30 (radial$\times$axial) grid used in the free-disc flow.

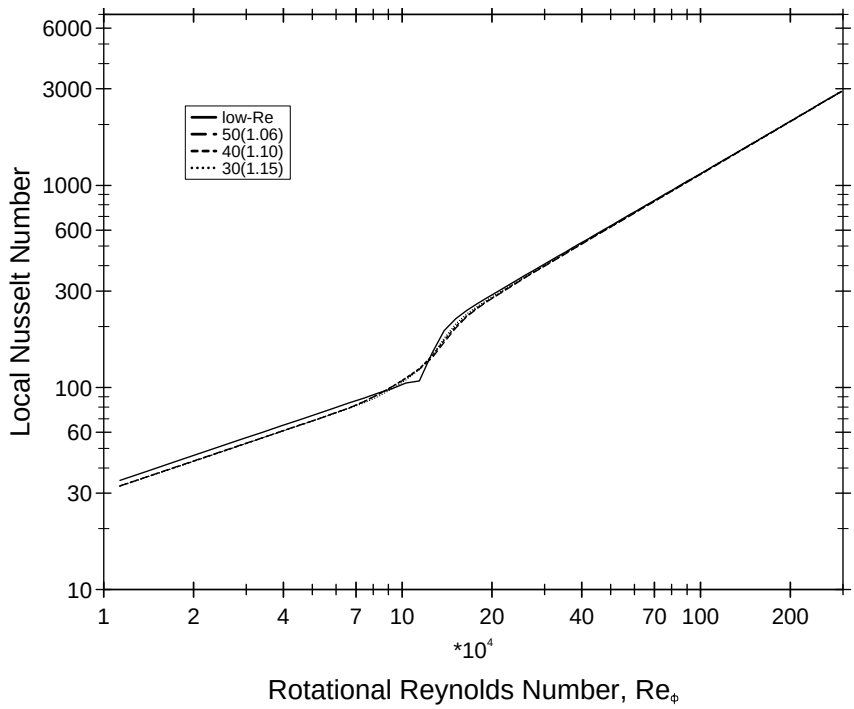

Figure 6.14: Predicted Nusselt number in the free-disc flow using the UMIST-*N* wall function and linear $k-\varepsilon$ model with different subgrid node density for the 120×28 main-grid (the key shows the number of subgrid nodes with the expansion ratio used to generate the subgrid mesh in parentheses).

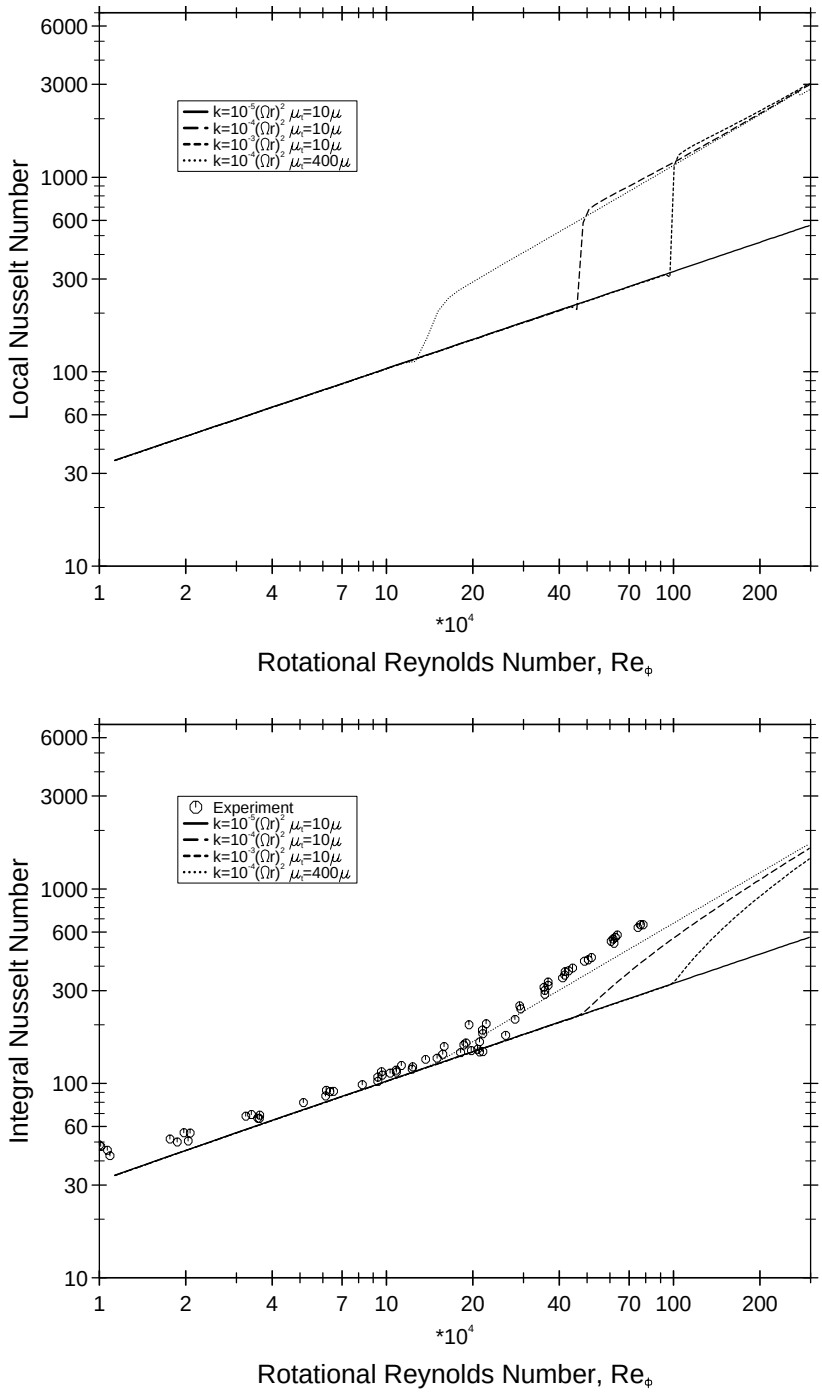

Figure 6.15: Predicted Nusselt number in the free-disc flow using the low-*Re* Launder & Sharma $k-\varepsilon$ model with different initial turbulence levels; ○: Cobb & Saunders experiments; *a*.) local Nusselt number (top); *b*.) integral Nusselt number (bottom).

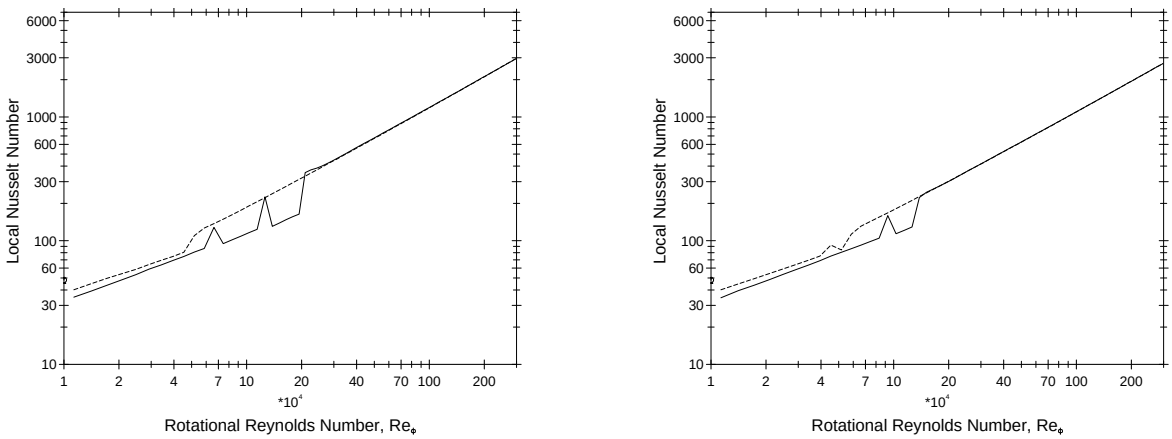

Figure 6.16: Predicted Nusselt number in the free-disc flow with two initial turbulence conditions, ——: $k = 10^{-5}\,(\Omega r_b)^2$ and $\mu_t = 10\mu$; - - -: $k = 10^{-5}\,(\Omega r_b)^2$ and $\mu_t = 400\mu$. Results obtained with the simplified Chieng & Launder (left) and Chieng & Launder wall function (right).

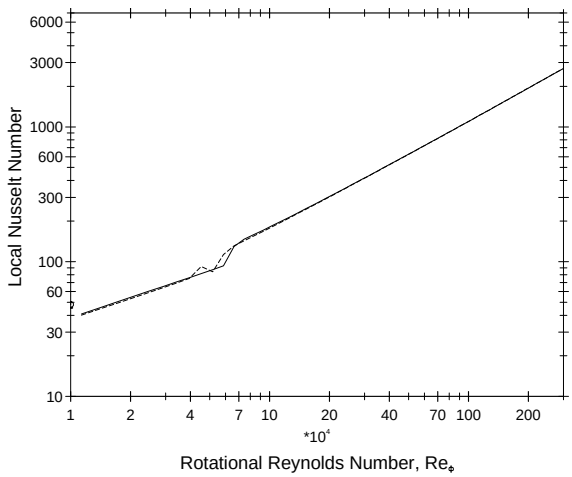

Figure 6.17: Predicted Nusselt number in the free-disc flow using the Chieng & Launder wall function with two different levels of under-relaxation; ——: $\alpha_{U,V,W} = 0.1$, $\alpha_P = 0.2$, $\alpha_{k,\varepsilon} = 0.1$ and $\alpha_T = 0.4$; - - -: $\alpha_{U,V,W} = 0.2$, $\alpha_P = 0.3$, $\alpha_{k,\varepsilon} = 0.1$ and $\alpha_T = 0.4$.

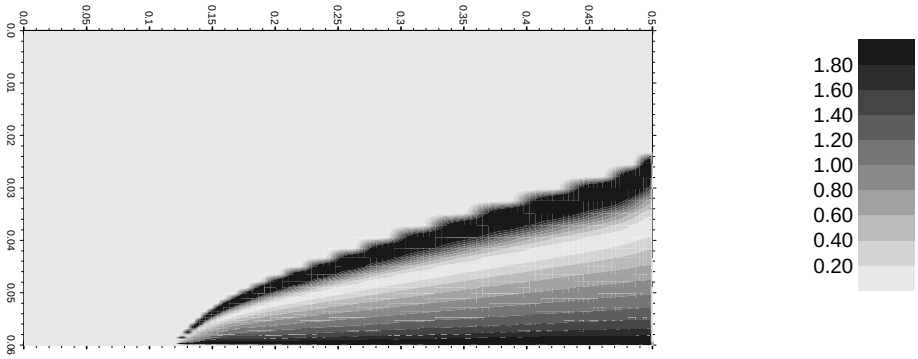

Figure 6.18: Predicted turbulent length scale gradient $\left(\left|\partial l/\partial x_j\right|\right)$ in the free-disc flow. Radial distance (r/D) is on the horizontal axis and axial distance (y/D) on the vertical axis. Transition from laminar to turbulent flow can be seen to occur at $r/D \approx 0.12$.

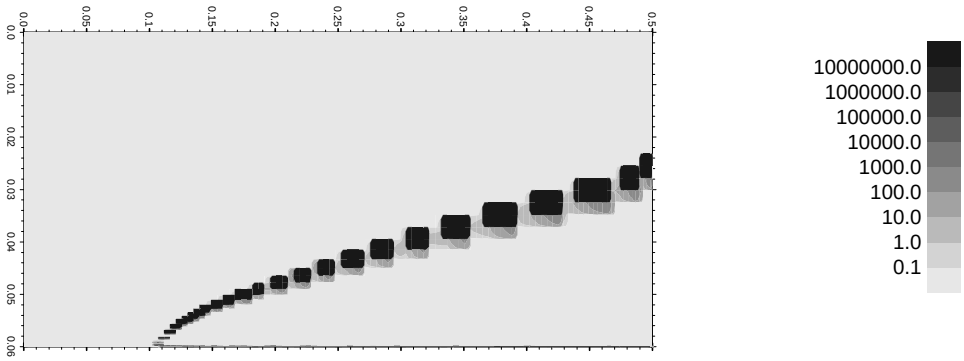

Figure 6.19: Predicted Yap correction using Equation (2.17) and $c_w = 0.83$ in the free-disc flow. Radial distance (r/D) is on the horizontal axis and axial distance (y/D) on the vertical axis.

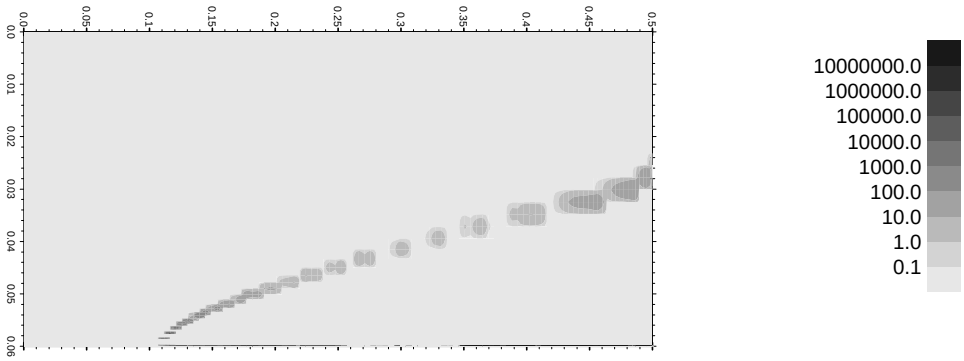

Figure 6.20: Predicted Yap correction in the free-disc flow using Equation (2.17) with c_w given by Equation (2.20). Radial distance (r/D) is on the horizontal axis and axial distance (y/D) on the vertical axis.

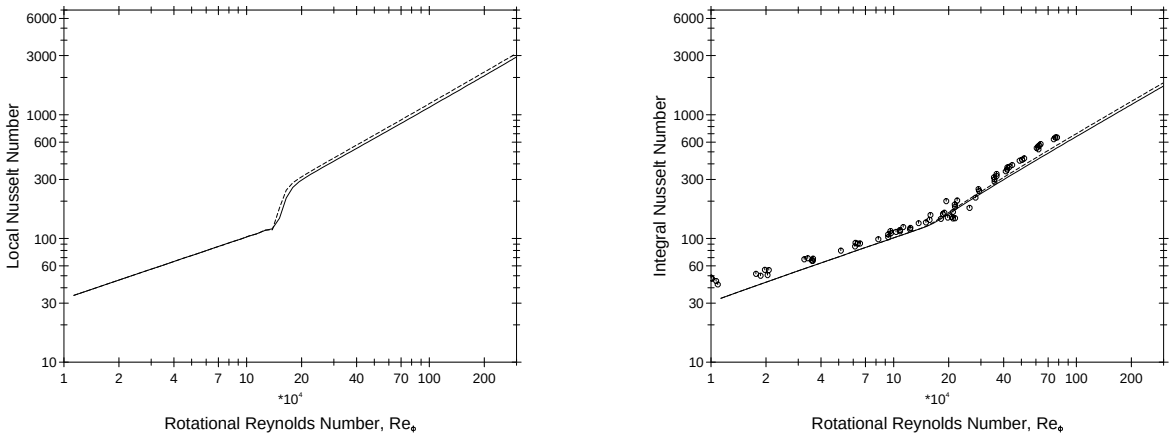

Figure 6.21: Predicted Nusselt number in the free-disc flow using the low-Reynolds-number NLEVM: ——: with differential Yap correction; - - -: without differential Yap correction; ○: experimental values from Cobb & Saunders [130]; *a*.) local Nusselt number (left); *b*.) integral Nusselt number (right).

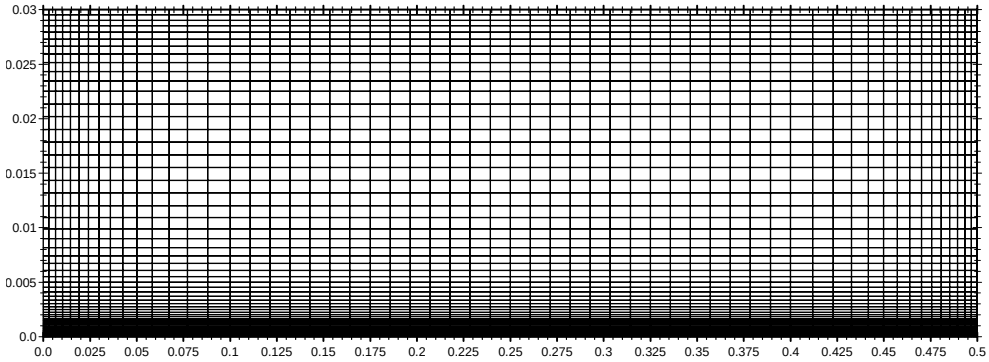

Figure 6.22: 60×60 grid used for laminar free-disc flow validation.

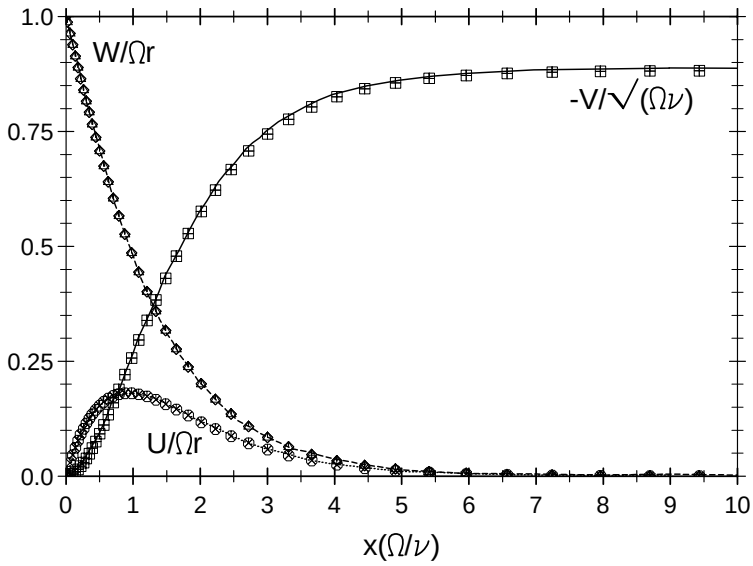

Figure 6.23: Velocity profiles for laminar free-disc flow; lines show the solution of the von Kármán equations by Owen & Rogers [132] ....: $U/\Omega r$; ——: $-V/\sqrt{\Omega\nu}$; - - -: $W/\Omega r$; (where U, V and W are respectively the radial, axial and tangential velocity); symbols indicate corresponding velocity predictions using the linear $k-\varepsilon$ model and the 60×60 grid shown in Figure 6.22 at three different rotational Reynolds numbers, $Re_\phi = 9000$, 25000 and 49000.

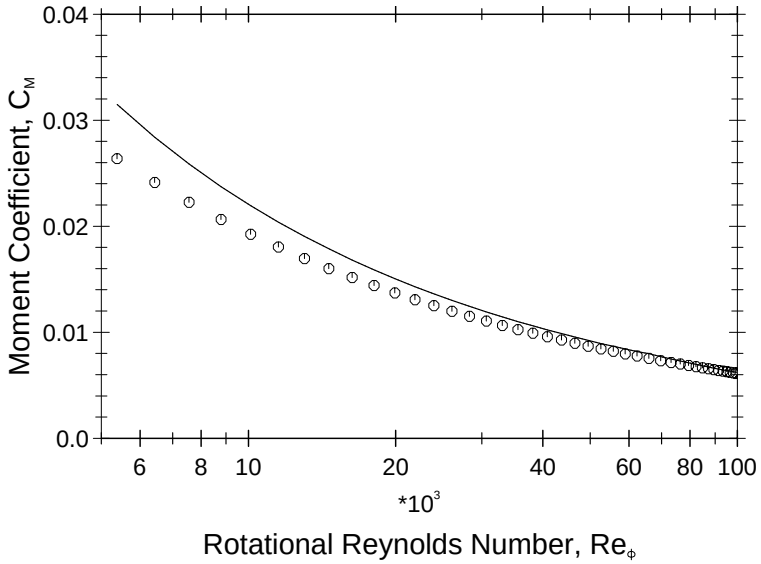

Figure 6.24: Predicted moment coefficient for laminar free-disc flow using the linear $k-\varepsilon$ model and the 60×60 grid shown in Figure 6.22. ○: Cochran's numerical solution of von Kármán's equations for laminar flow over the free-disc [131].

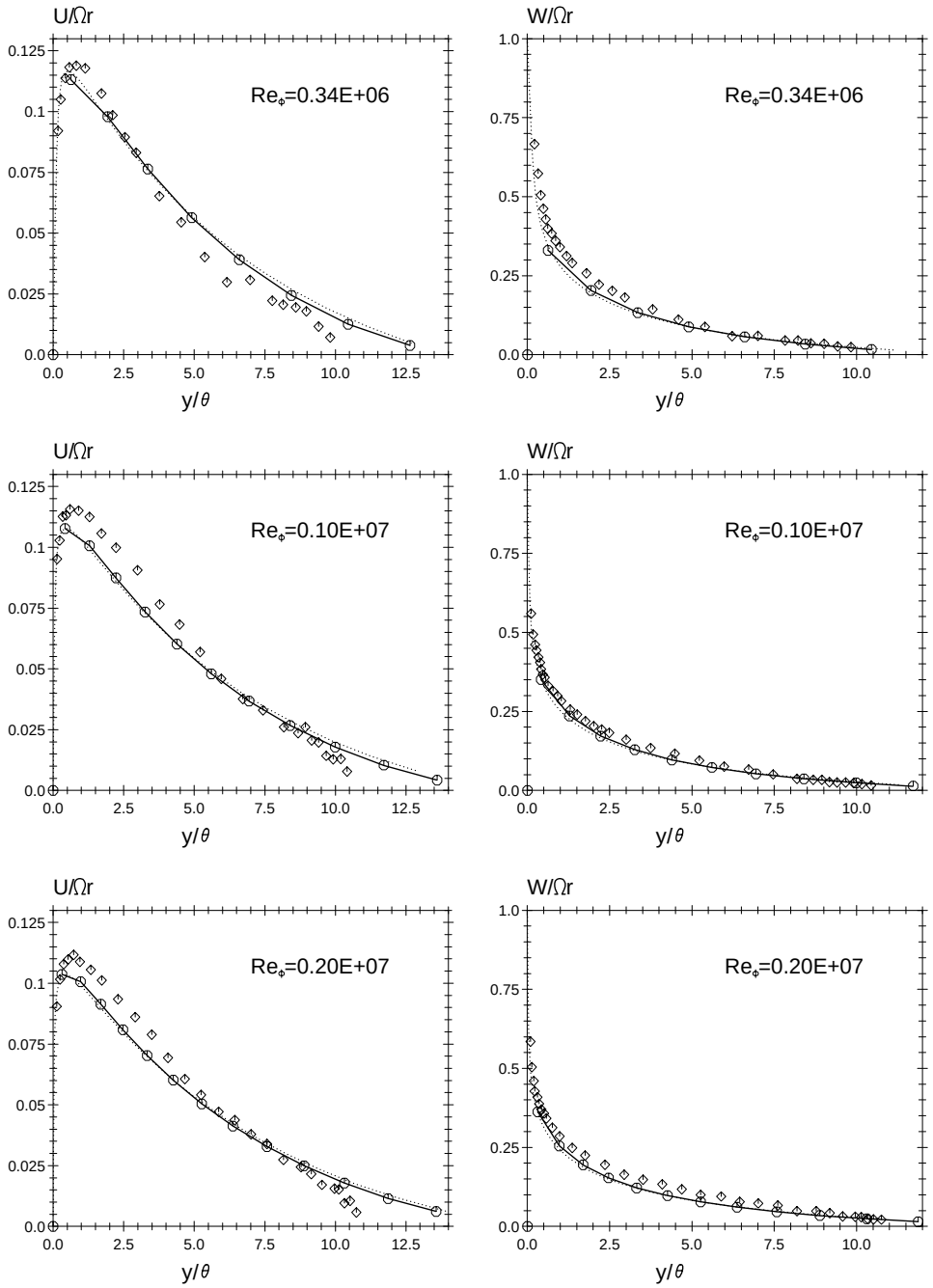

Figure 6.25: Radial and tangential velocity profiles in the free-disc flow using the TEAM wall function and linear $k-\varepsilon$ model with the 120×28 grid; —⊖—: high-*Re* model prediction (circles indicate the position of nodes); .....: low-*Re* model prediction; ◊: Cham & Head experiments.

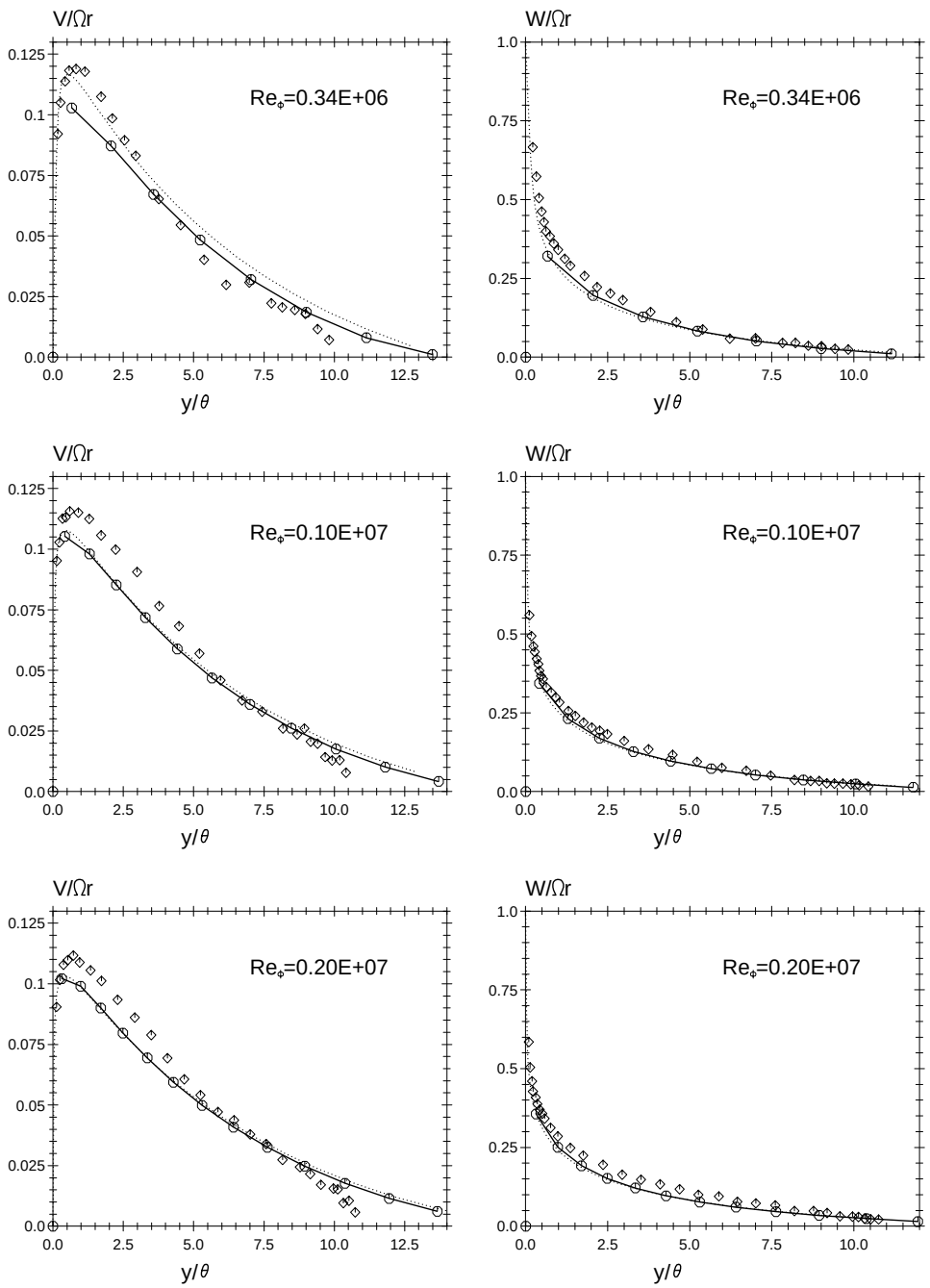

Figure 6.26: Radial and tangential velocity profiles in the free-disc flow using the simplified Chieng & Launder wall function and linear $k-\varepsilon$ model with the 120×28 grid; —⊖—: high-*Re* model prediction (circles indicate the position of nodes); .....: low-*Re* model prediction; ◊: Cham & Head experiments.

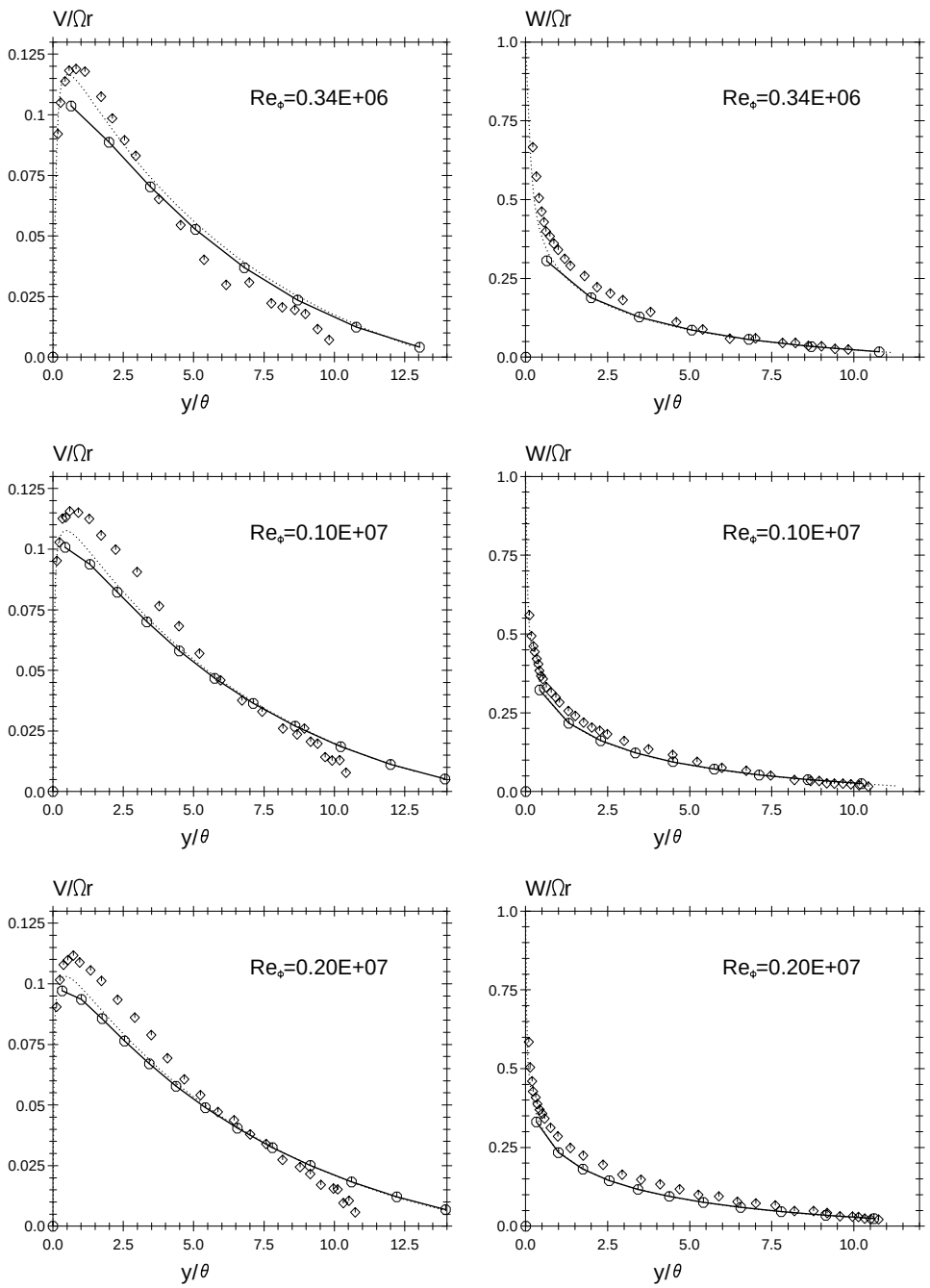

Figure 6.27: Radial and tangential velocity profiles in the free-disc flow using the Chieng & Launder wall function and linear $k-\varepsilon$ model with the 120×28 grid; —⊖—: high-*Re* model prediction (circles indicate the position of nodes); .....: low-*Re* model prediction; ◊: Cham & Head experiments.

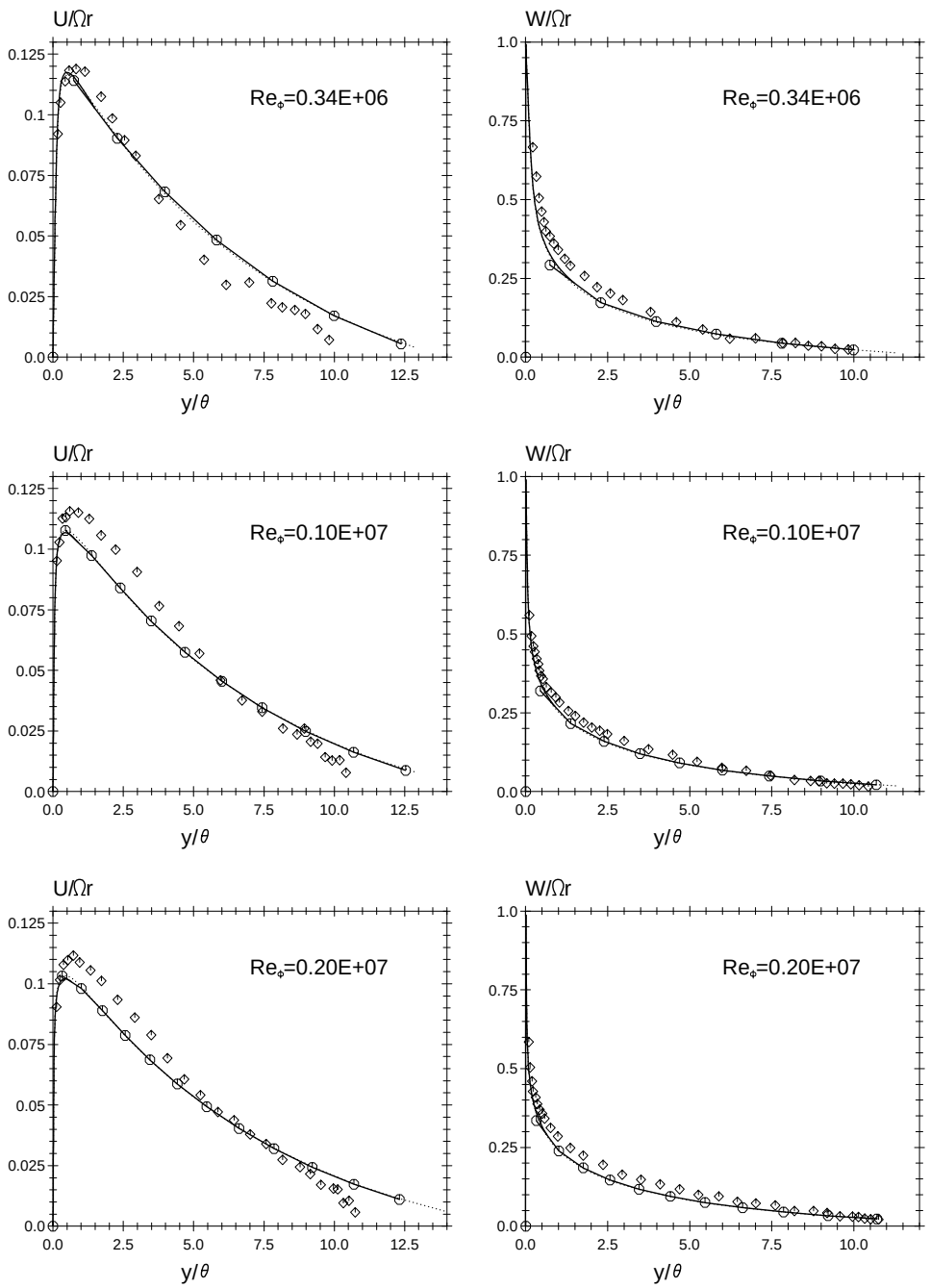

Figure 6.28: Radial and tangential velocity profiles in the free-disc flow using the UMIST-*N* wall function and linear $k-\varepsilon$ model with the 120×28 grid; —⊖—: high-*Re* model prediction (circles indicate the position of nodes); .....: low-*Re* model prediction; ◊: Cham & Head experiments.

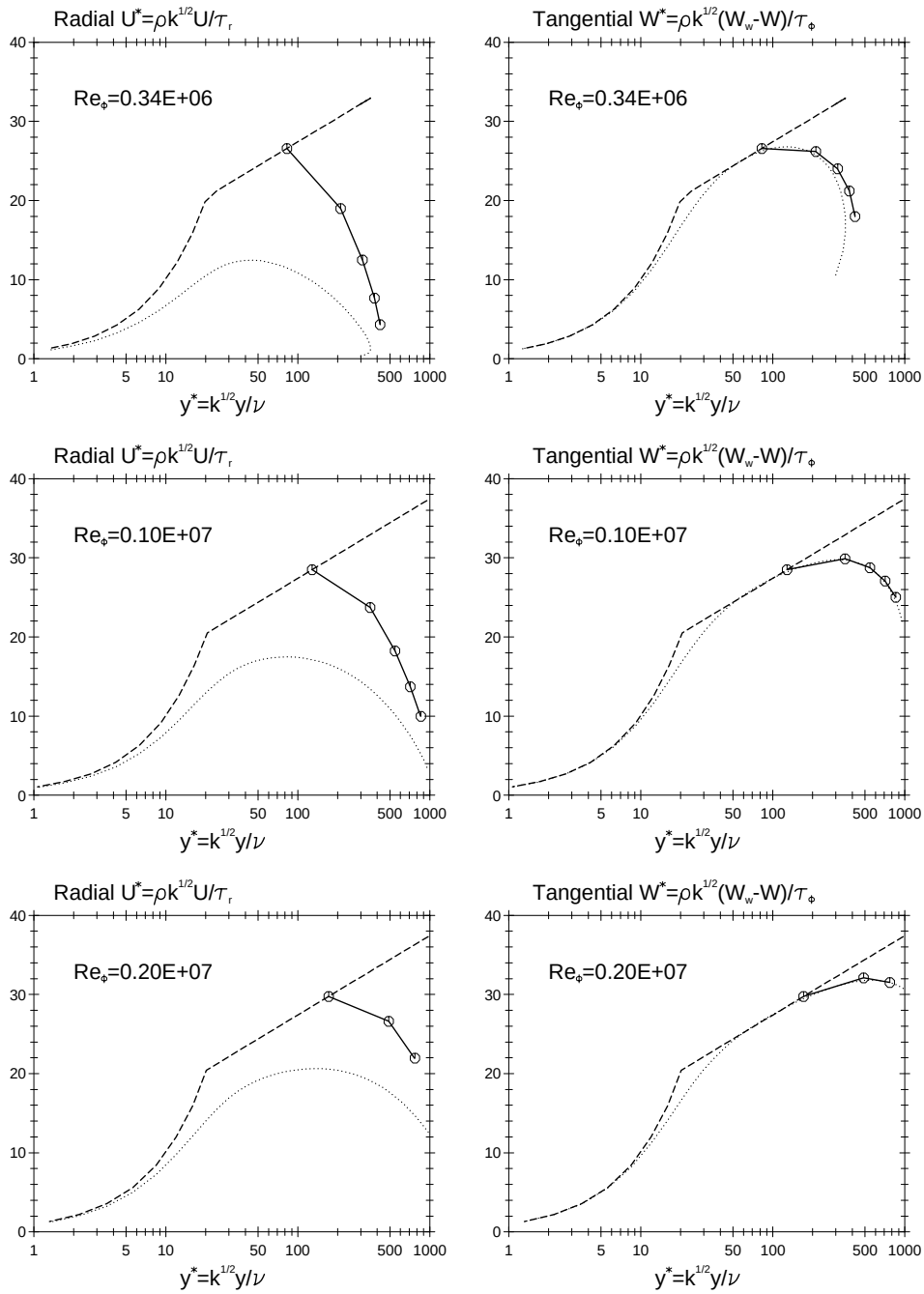

Figure 6.29: Radial and tangential velocity profiles in the free-disc flow using the TEAM wall function and linear $k-\varepsilon$ model with the 120×28 grid; —⊖—: high-*Re* model prediction (circles indicate the position of nodes); .....: low-*Re* model prediction; - - -: "universal" log-law.

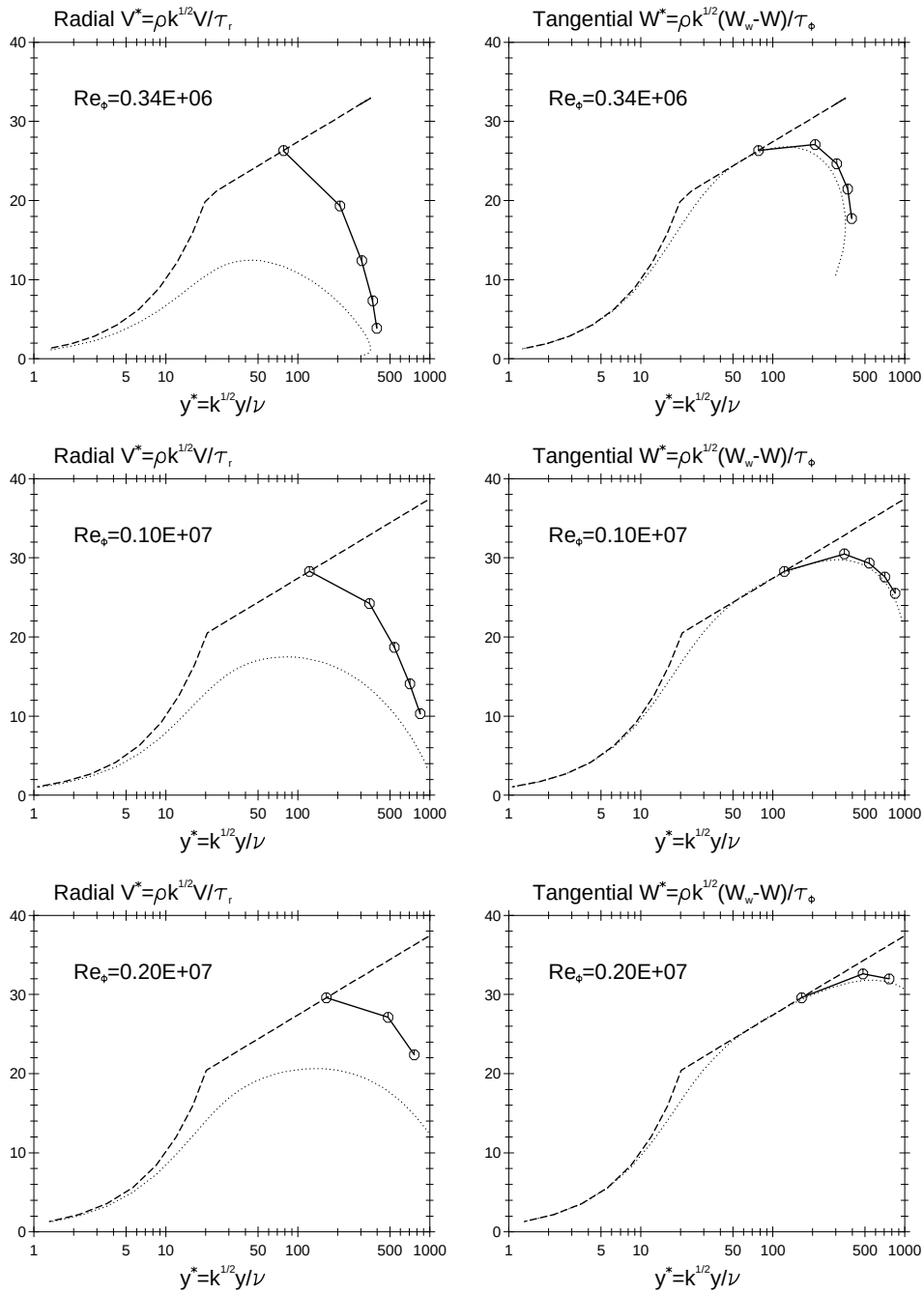

Figure 6.30: Radial and tangential velocity profiles in the free-disc flow using the simplified Chieng & Launder wall function and linear $k-\varepsilon$ model with the 120×28 grid; —⊖—: high-*Re* model prediction (circles indicate the position of nodes); .....: low-*Re* model prediction; - - -: "universal" log-law.

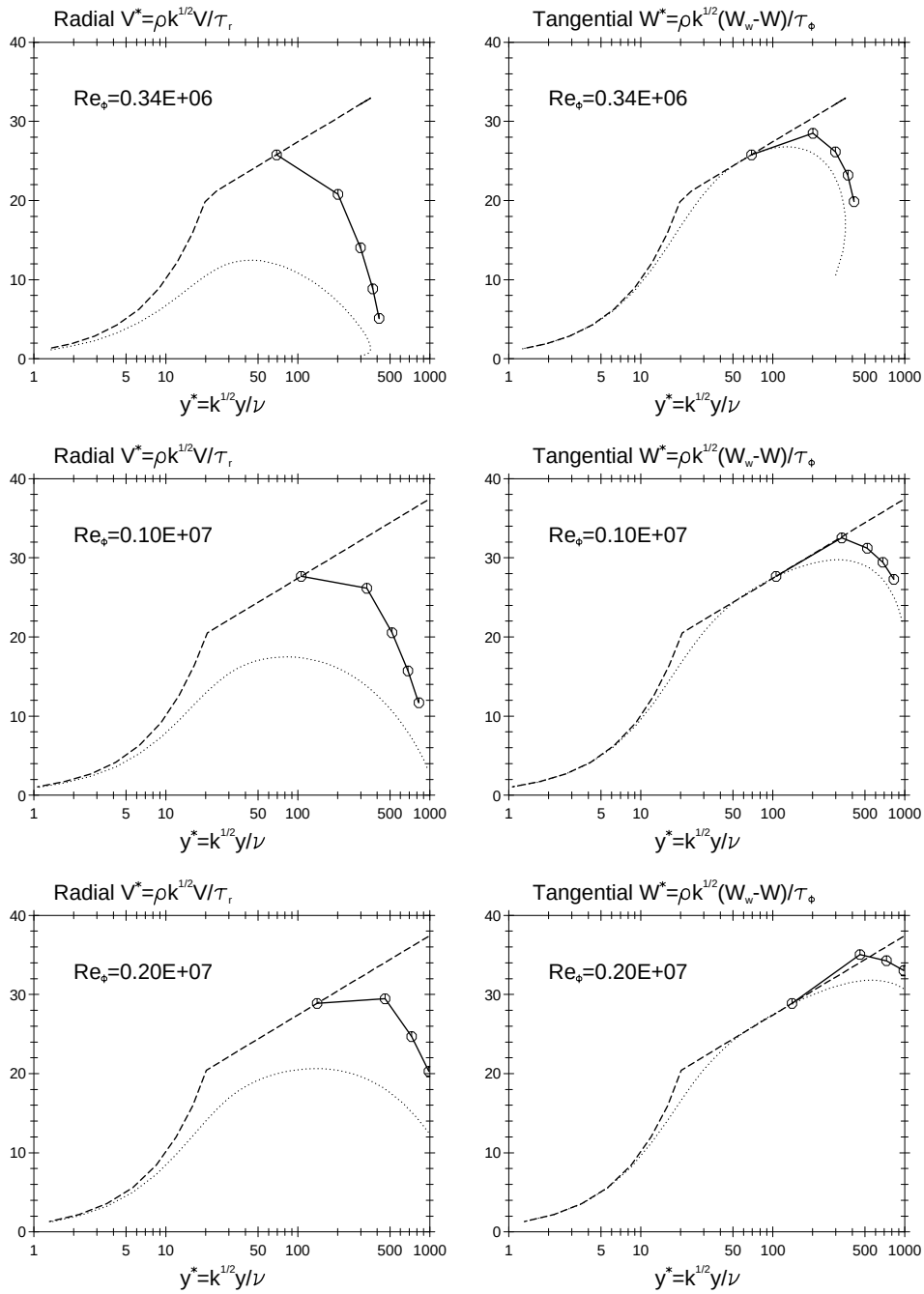

Figure 6.31: Radial and tangential velocity profiles in the free-disc flow using the Chieng & Launder wall function and linear $k-\varepsilon$ model with the 120×28 grid; —⊖—: high-*Re* model prediction (circles indicate the position of nodes); .....: low-*Re* model prediction; - - -: "universal" log-law.

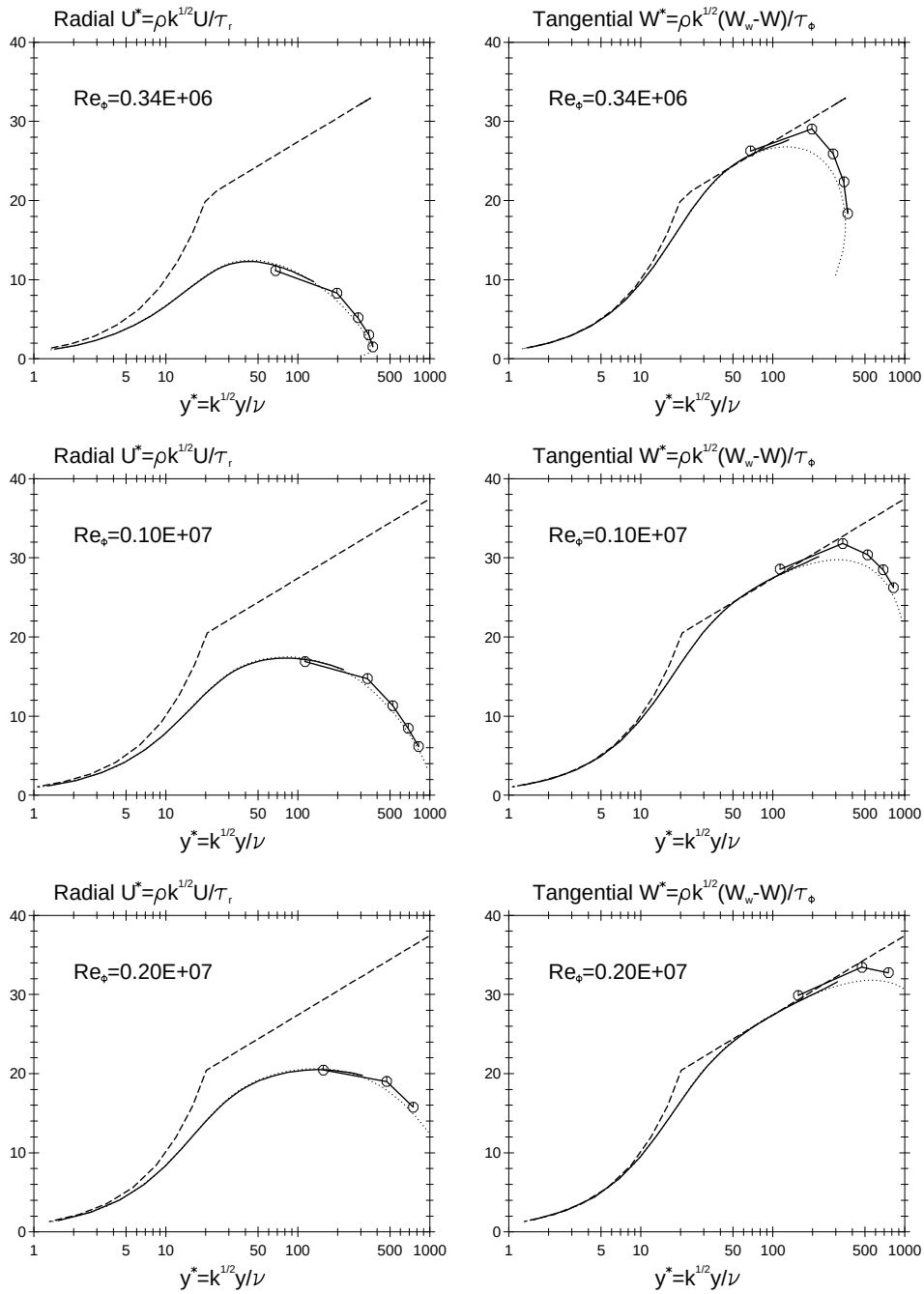

Figure 6.32: Radial and tangential velocity profiles in the free-disc flow using the UMIST-*N* wall function and linear $k-\varepsilon$ model with the 120×28 grid; —⊖—: high-*Re* model prediction (circles indicate the position of nodes); .....: low-*Re* model prediction; - - -: "universal" log-law.

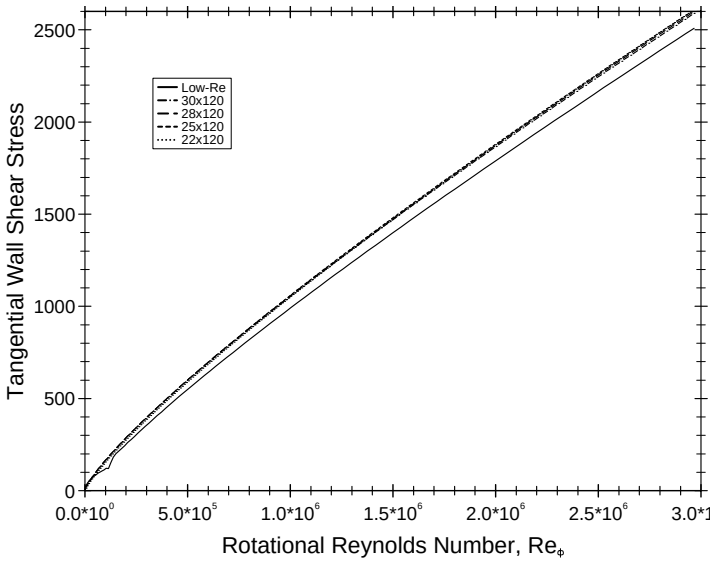

Figure 6.33: Predicted tangential wall shear stress, given by $\tau_{wall,\phi} / \left[0.5\rho\left(\Omega r_b\right)^2\right] \times 10^6$, in the free-disc flow using the TEAM wall function and linear $k-\varepsilon$ model. Solid line: low-*Re* model; broken lines: wall function results for different grid arrangements (for corresponding y^+ values for these grids see Figure 6.50).

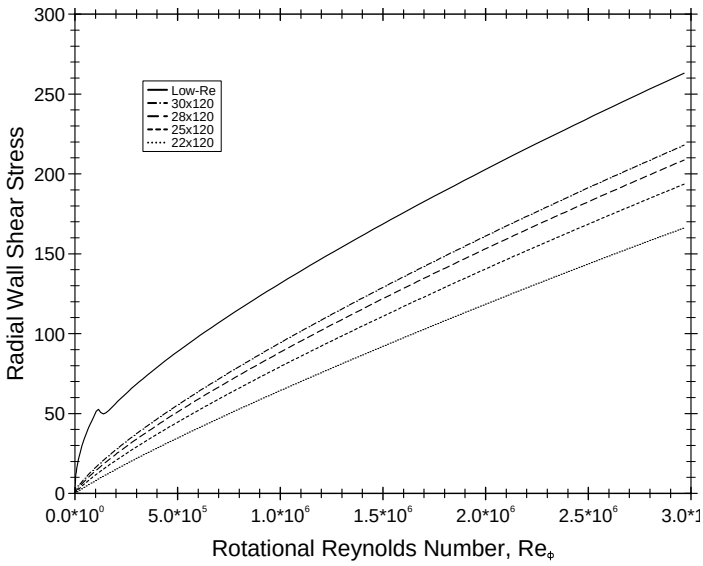

Figure 6.34: Predicted radial wall shear stress, given by $\tau_{wall,r} / \left[0.5\rho\left(\Omega r_b\right)^2\right] \times 10^6$, in the free-disc flow using the TEAM wall function and linear $k-\varepsilon$ model. Solid line: low-*Re* model; broken lines: wall function results for different grid arrangements (for corresponding y^+ values for these grids see Figure 6.50).

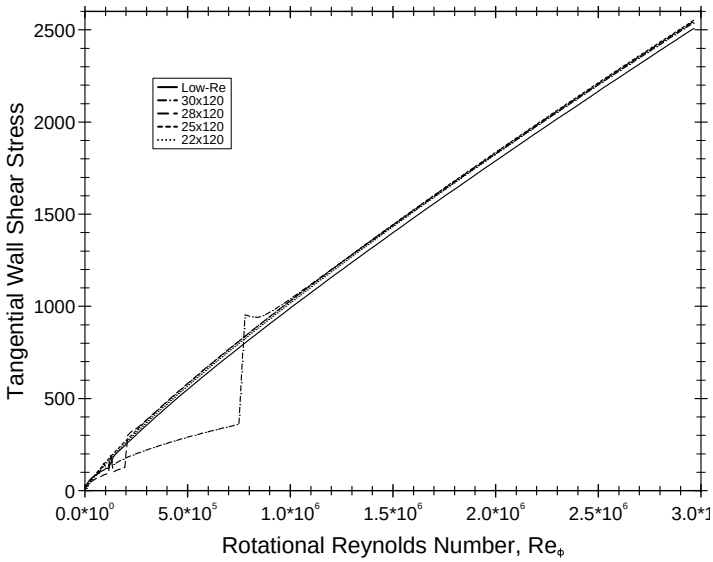

Figure 6.35: Predicted tangential wall shear stress, given by $\tau_{wall,\phi} / \left[0.5\rho\left(\Omega r_b\right)^2\right] \times 10^6$, in the free-disc flow using the simplified Chieng & Launder wall function and linear $k-\varepsilon$ model. Solid line: low-*Re* model; broken lines: wall function results for different grid arrangements (for corresponding y^+ values for these grids see Figure 6.51).

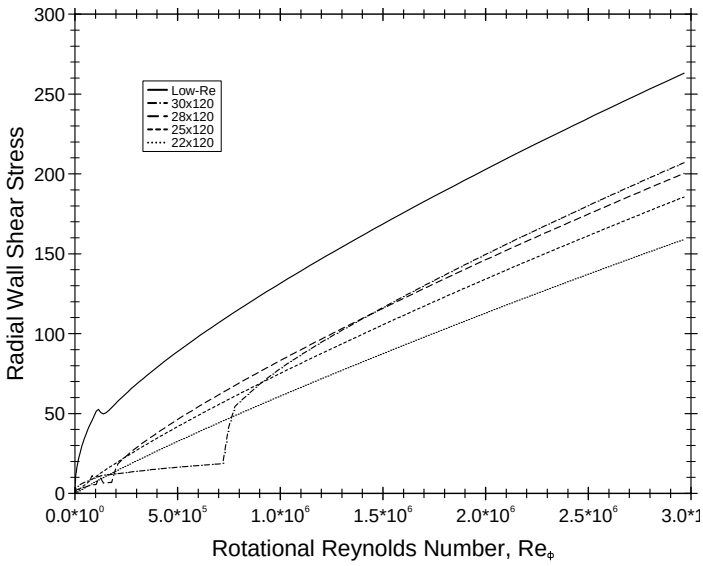

Figure 6.36: Predicted radial wall shear stress, given by $\tau_{wall,r} / \left[0.5\rho\left(\Omega r_b\right)^2\right] \times 10^6$, in the free-disc flow using the simplified Chieng & Launder wall function and linear $k-\varepsilon$ model. Solid line: low-*Re* model; broken lines: wall function results for different grid arrangements (for corresponding y^+ values for these grids see Figure 6.51).

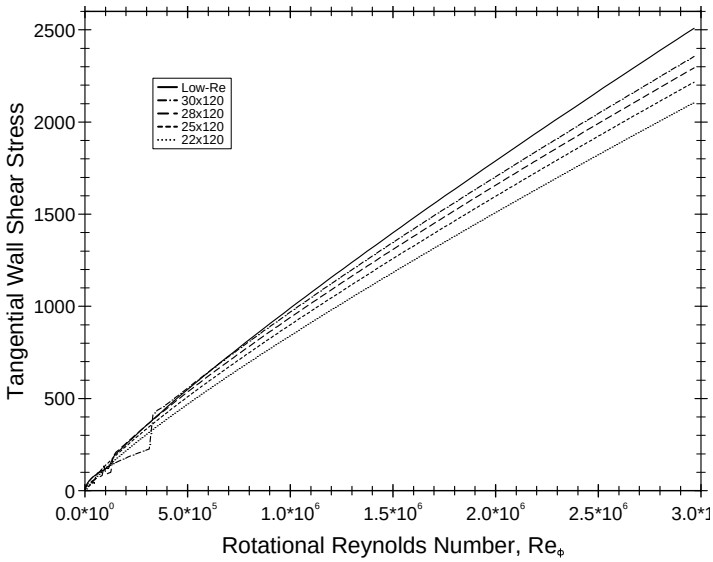

Figure 6.37: Predicted tangential wall shear stress, given by $\tau_{wall,\phi} / \left[0.5\rho\left(\Omega r_b\right)^2\right] \times 10^6$, in the free-disc flow using the Chieng & Launder wall function and linear $k-\varepsilon$ model. Solid line: low-*Re* model; broken lines: wall function results for different grid arrangements (for corresponding y^+ values for these grids see Figure 6.52).

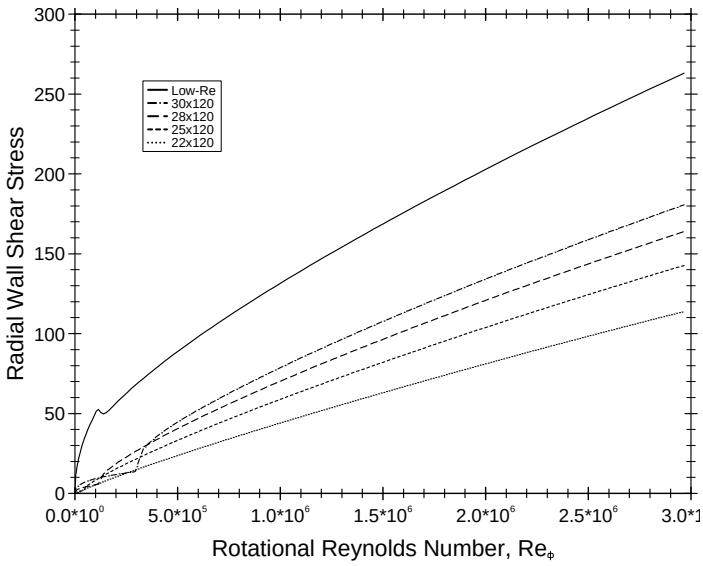

Figure 6.38: Predicted radial wall shear stress, given by $\tau_{wall,r} / \left[0.5\rho\left(\Omega r_b\right)^2\right] \times 10^6$, in the free-disc flow using the Chieng & Launder wall function and linear $k-\varepsilon$ model. Solid line: low-*Re* model; broken lines: wall function results for different grid arrangements (for corresponding y^+ values for these grids see Figure 6.52).

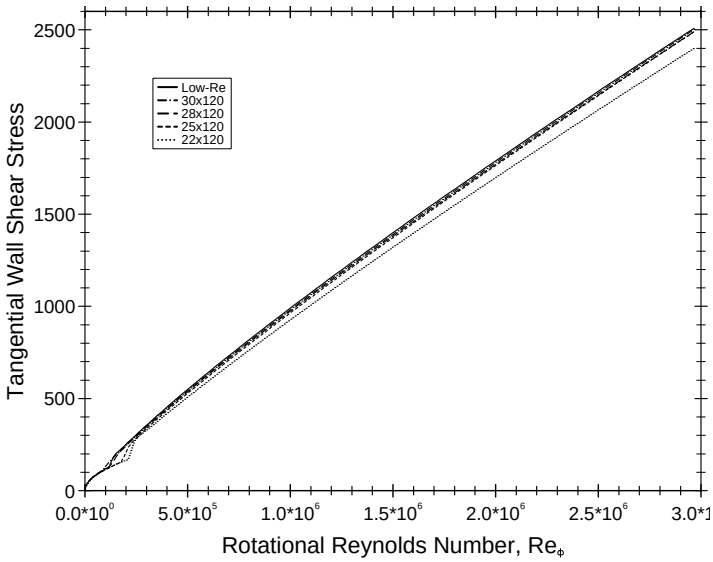

Figure 6.39: Predicted tangential wall shear stress, given by $\tau_{wall,\phi} / \left[0.5\rho\left(\Omega r_b\right)^2\right] \times 10^6$, in the free-disc flow using the UMIST-*N* wall function and linear $k-\varepsilon$ model. Solid line: low-*Re* model; broken lines: wall function results for different grid arrangements (for corresponding y^+ values for these grids see Figure 6.53).

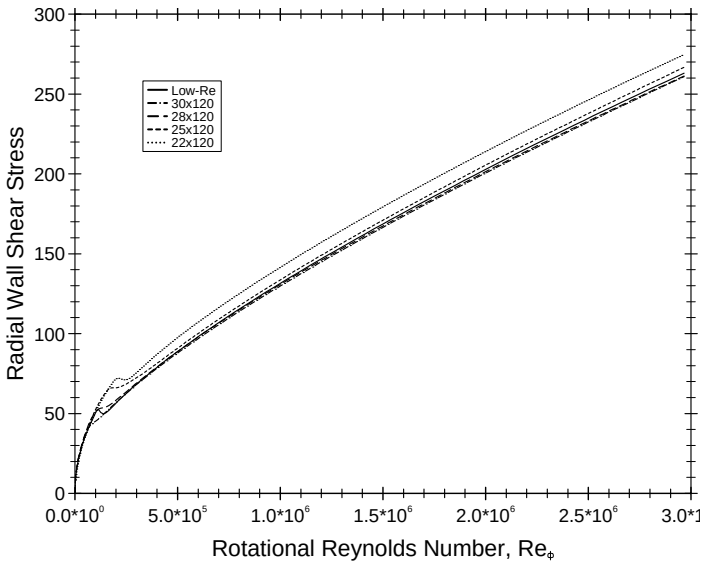

Figure 6.40: Predicted radial wall shear stress, given by $\tau_{wall,r} / \left[0.5\rho\left(\Omega r_b\right)^2\right] \times 10^6$, in the free-disc flow using the UMIST-*N* wall function and linear $k-\varepsilon$ model. Solid line: low-*Re* model; broken lines: wall function results for different grid arrangements (for corresponding y^+ values for these grids see Figure 6.53).

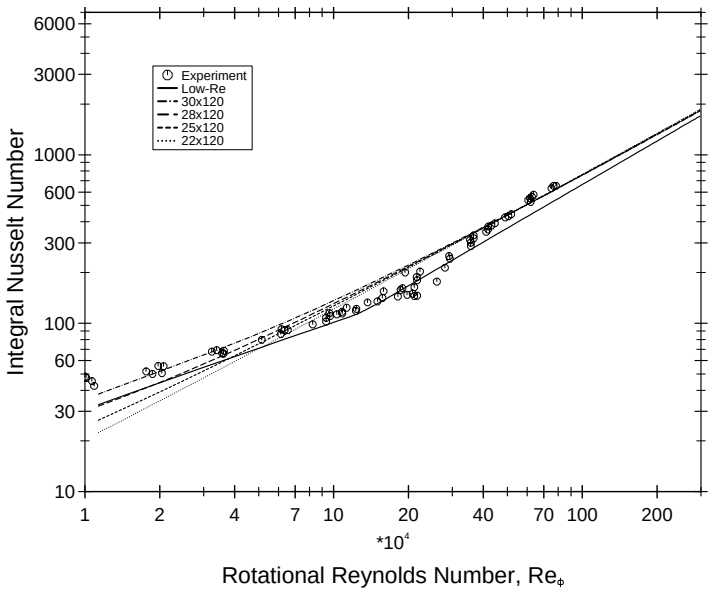

Figure 6.41: Predicted integral Nusselt number in the free-disc flow using the TEAM wall function and linear $k-\varepsilon$ model. Solid line: low-*Re* model; broken lines: wall function results for different grid arrangements (for corresponding y^+ values for these grids see Figure 6.50); ○: experimental values from Cobb & Saunders [130].

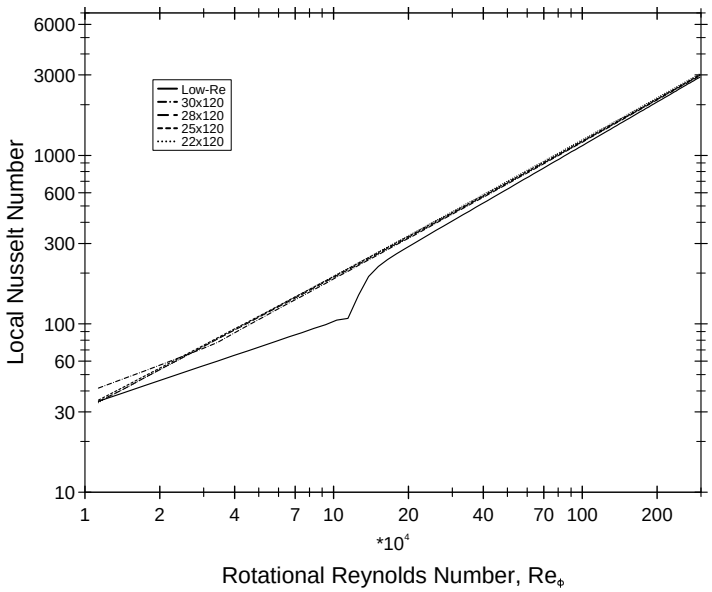

Figure 6.42: Predicted local Nusselt number in the free-disc flow using the TEAM wall function and linear $k-\varepsilon$ model. Solid line: low-*Re* model; broken lines: wall function results for different grid arrangements (for corresponding y^+ values for these grids see Figure 6.50).

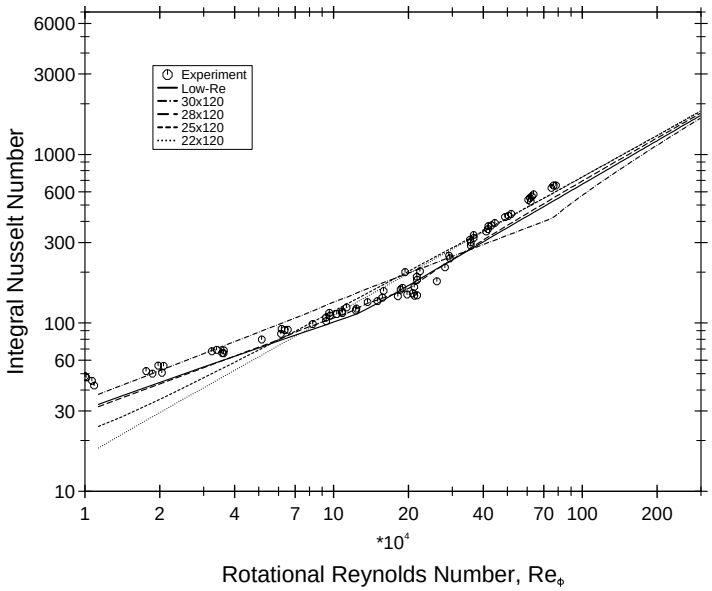

Figure 6.43: Predicted integral Nusselt number in the free-disc flow using the simplified Chieng & Launder wall function and linear $k-\varepsilon$ model. Solid line: low-*Re* model; broken lines: wall function results for different grid arrangements (for corresponding y^+ values for these grids see Figure 6.51); ○: experimental values from Cobb & Saunders [130].

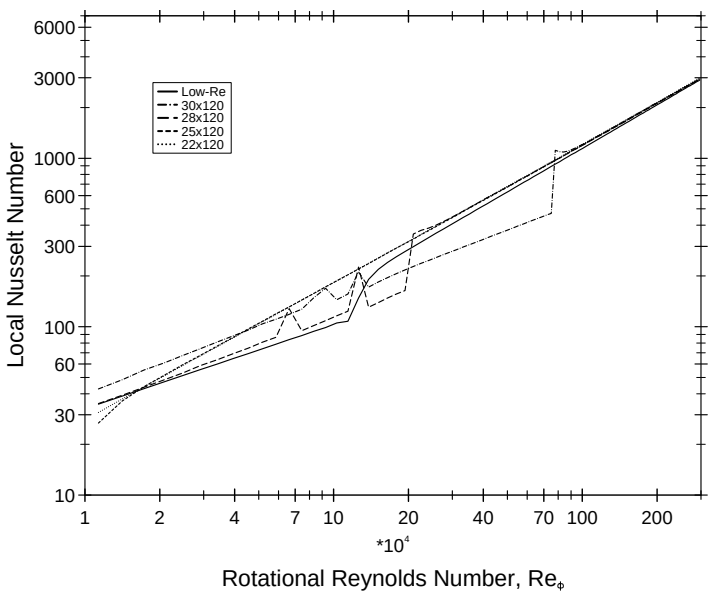

Figure 6.44: Predicted local Nusselt number in the free-disc flow using the simplified Chieng & Launder wall function and linear $k-\varepsilon$ model. Solid line: low-*Re* model; broken lines: wall function results for different grid arrangements (for corresponding y^+ values for these grids see Figure 6.51).

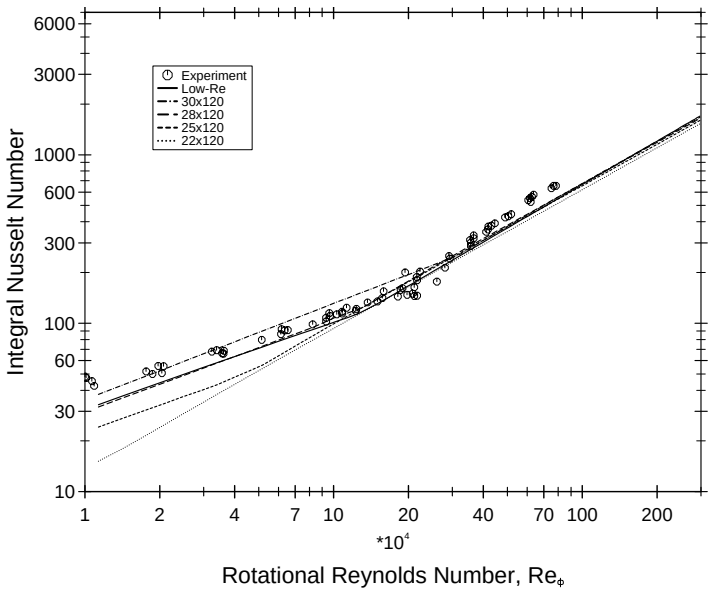

Figure 6.45: Predicted integral Nusselt number in the free-disc flow using the Chieng & Launder wall function and linear $k-\varepsilon$ model. Solid line: low-*Re* model; broken lines: wall function results for different grid arrangements (for corresponding y^+ values for these grids see Figure 6.52); ○: experimental values from Cobb & Saunders [130].

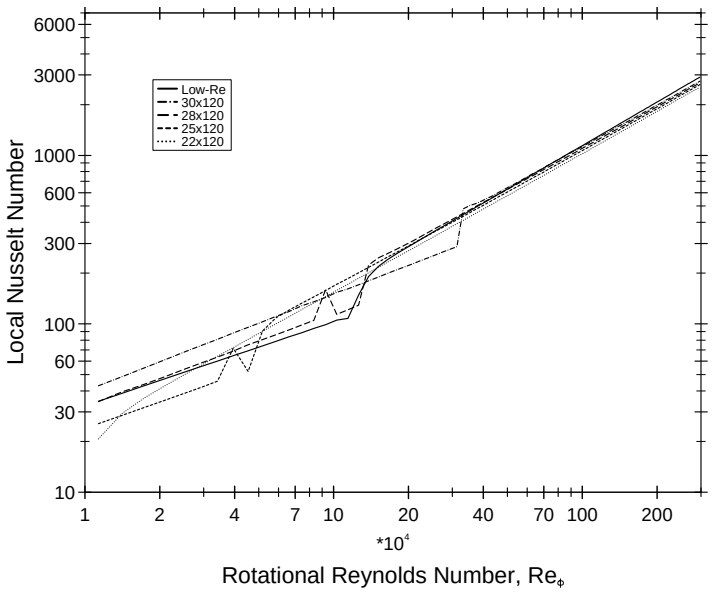

Figure 6.46: Predicted local Nusselt number in the free-disc flow using the Chieng & Launder wall function and linear $k-\varepsilon$ model. Solid line: low-*Re* model; broken lines: wall function results for different grid arrangements (for corresponding y^+ values for these grids see Figure 6.52).

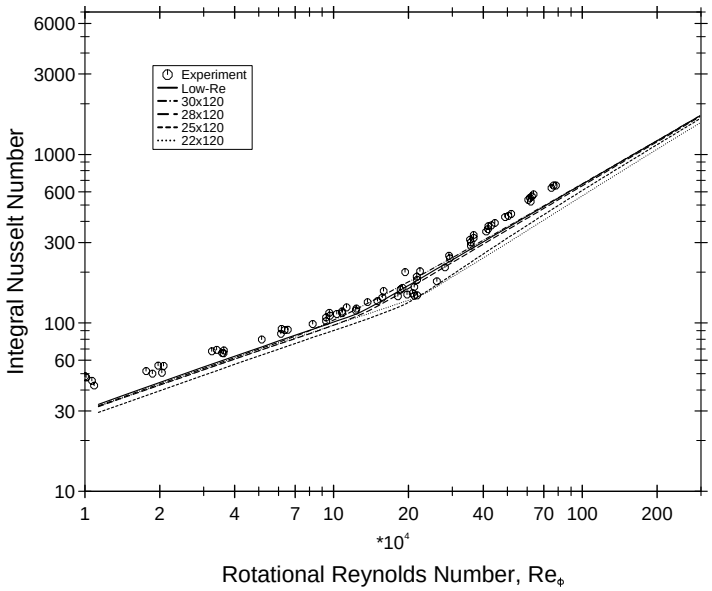

Figure 6.47: Predicted integral Nusselt number in the free-disc flow using the UMIST-*N* wall function and linear $k-\varepsilon$ model. Solid line: low-*Re* model; broken lines: wall function results for different main-grid arrangements (for corresponding y^+ values for these grids see Figure 6.53); ○: experimental values from Cobb & Saunders [130].

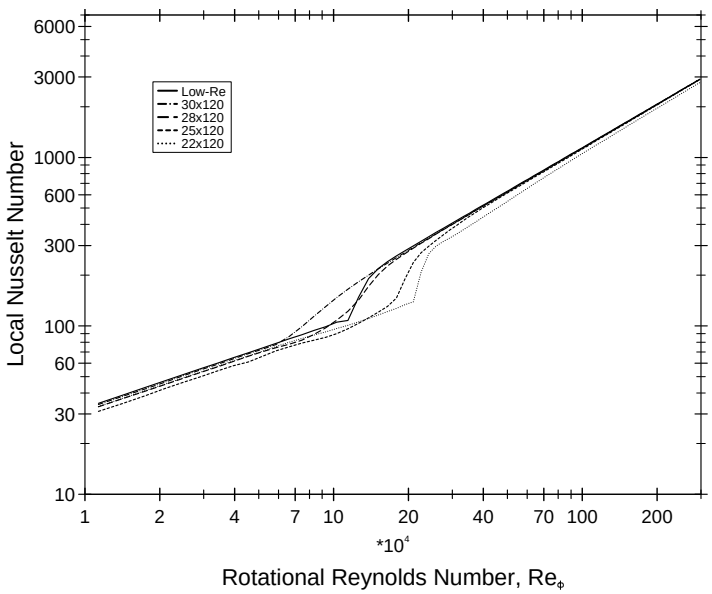

Figure 6.48: Predicted local Nusselt number in the free-disc flow using the UMIST-*N* wall function and linear $k-\varepsilon$ model. Solid line: low-*Re* model; broken lines: wall function results for different main-grid arrangements (also shown on linear axes in Figure 6.49). For corresponding y^+ values for these grids see Figure 6.53.

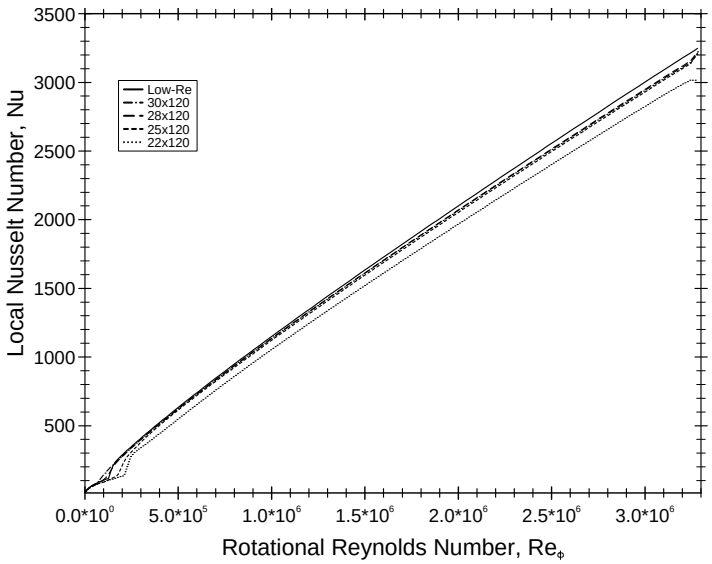

Figure 6.49: Predicted Nusselt number in the free-disc flow using the UMIST-*N* wall function and linear $k-\varepsilon$ model. Solid line: low-*Re* model; broken lines: wall function results for different main-grid arrangements (also shown on log-axes in Figure 6.48).

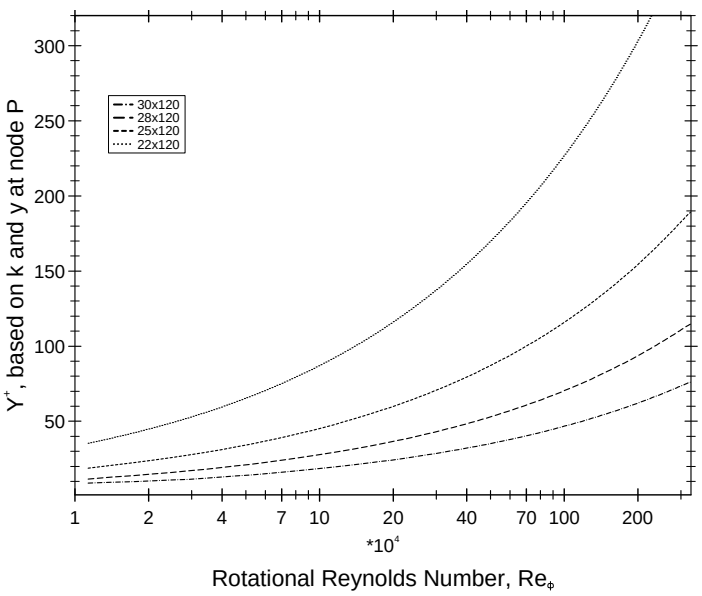

Figure 6.50: Dimensionless wall distance, $y^+ = c_\mu^{1/4} k^{1/2} y/\nu$, of the wall adjacent node in the free-disc flow using the TEAM wall function and linear $k-\varepsilon$ model with different grid arrangements, corresponding to the Nusselt number predictions shown in Figure 6.41 and 6.42.

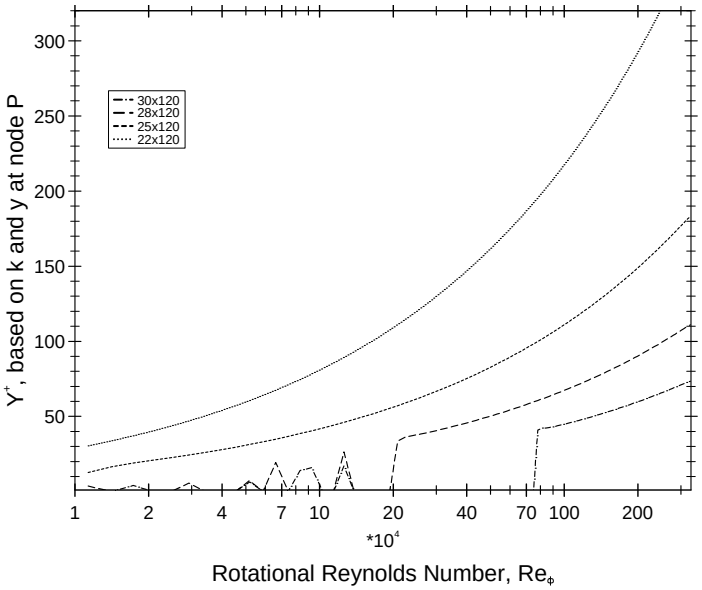

Figure 6.51: Dimensionless wall distance, $y^+ = c_\mu^{1/4} k^{1/2} y/\nu$, of the wall adjacent node in the free-disc flow using the simplified Chieng & Launder wall function and linear $k-\varepsilon$ model with different grid arrangements, corresponding to the Nusselt number predictions shown in Figure 6.43 and 6.44.

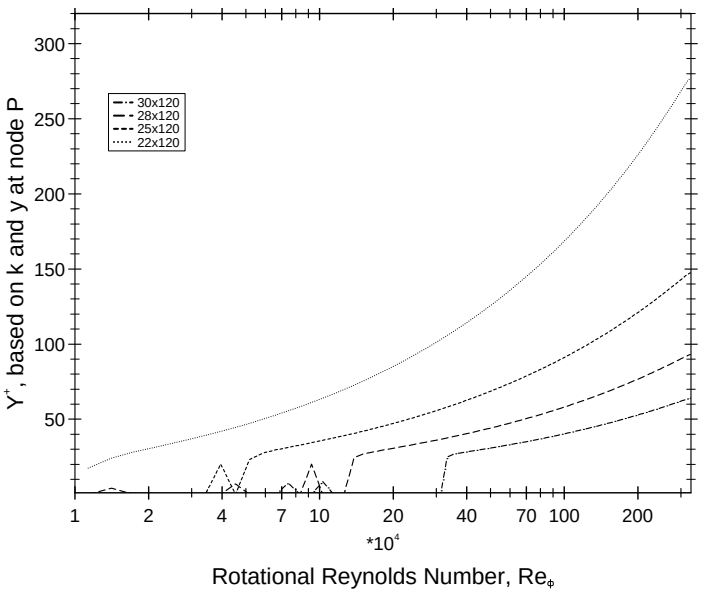

Figure 6.52: Dimensionless wall distance, $y^+ = c_\mu^{1/4} k^{1/2} y/\nu$, of the wall adjacent node in the free-disc flow using the Chieng & Launder wall function and linear $k-\varepsilon$ model with different grid arrangements, corresponding to the Nusselt number predictions shown in Figure 6.45 and 6.46.

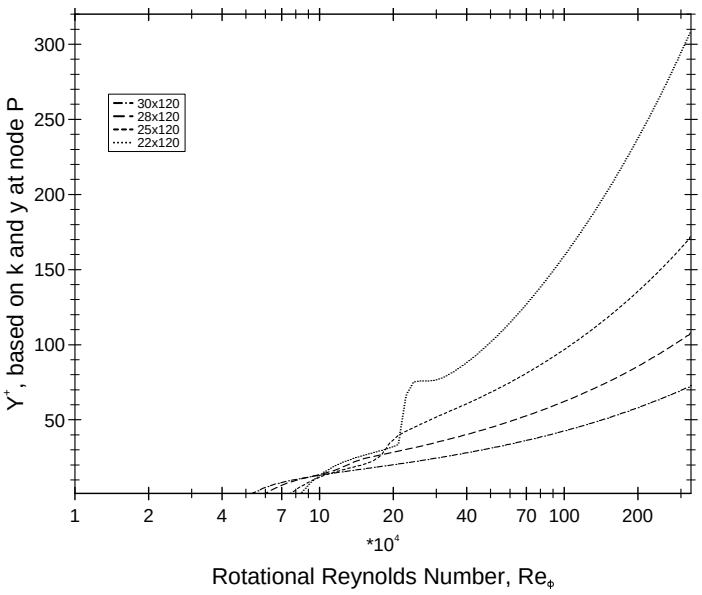

Figure 6.53: Dimensionless wall distance, $y^+ = c_\mu^{1/4} k^{1/2} y/\nu$, of the wall adjacent node in the free-disc flow using the UMIST-N wall function and linear $k-\varepsilon$ model with different main-grid arrangements corresponding to the Nusselt number predictions shown in Figures 6.47, 6.48 and 6.49.

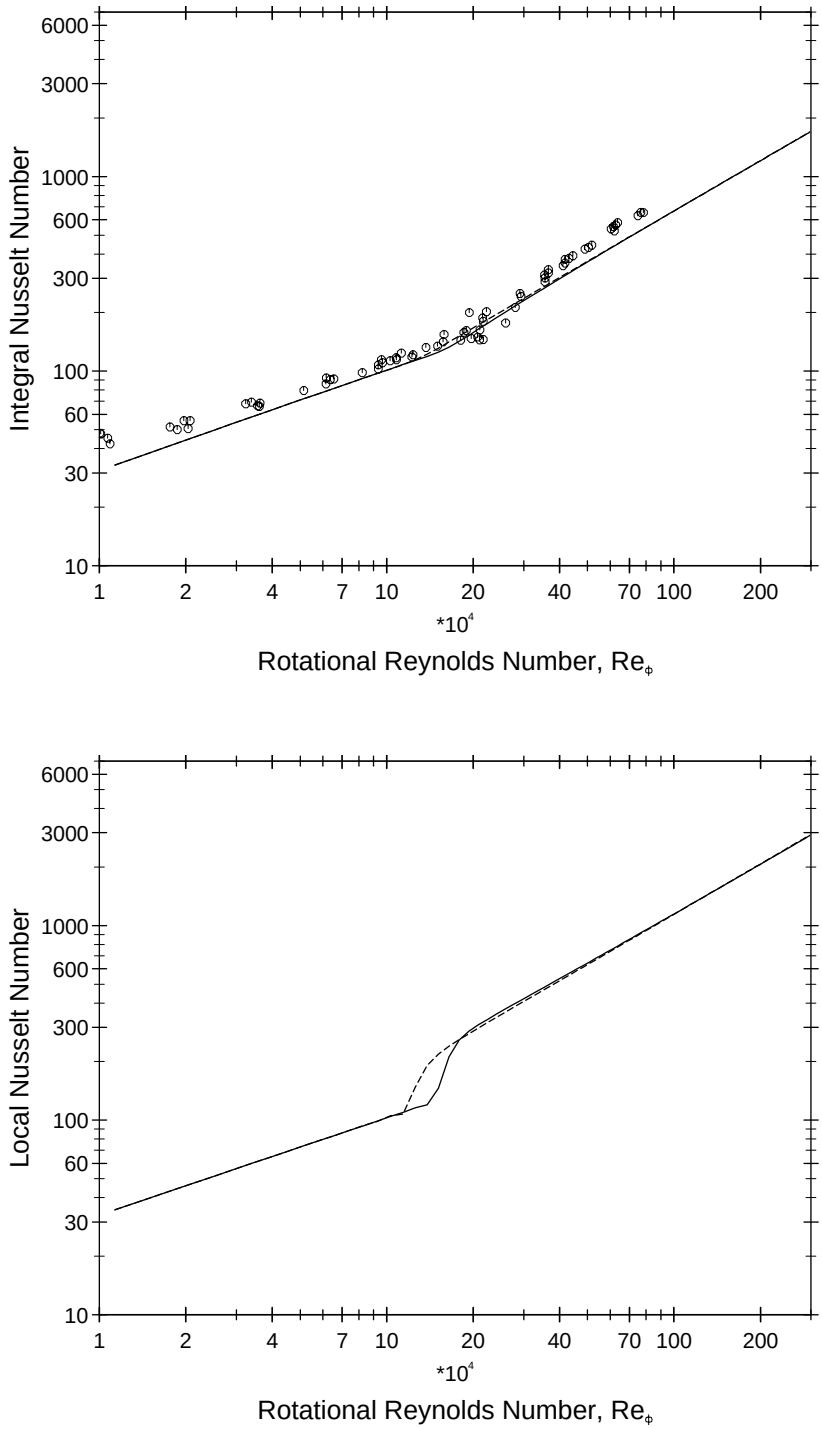

Figure 6.54: Predicted Nusselt number in the free-disc flow using the low-Reynolds-number linear $k-\varepsilon$ model of Launder & Sharma and the non-linear $k-\varepsilon$ model of Craft *et al*. [67]; ——: NLEVM; - - -: linear $k-\varepsilon$; ○: Cobb & Saunders experiments; *a*.) integral Nusselt number (top) *b*.) local Nusselt number (bottom).

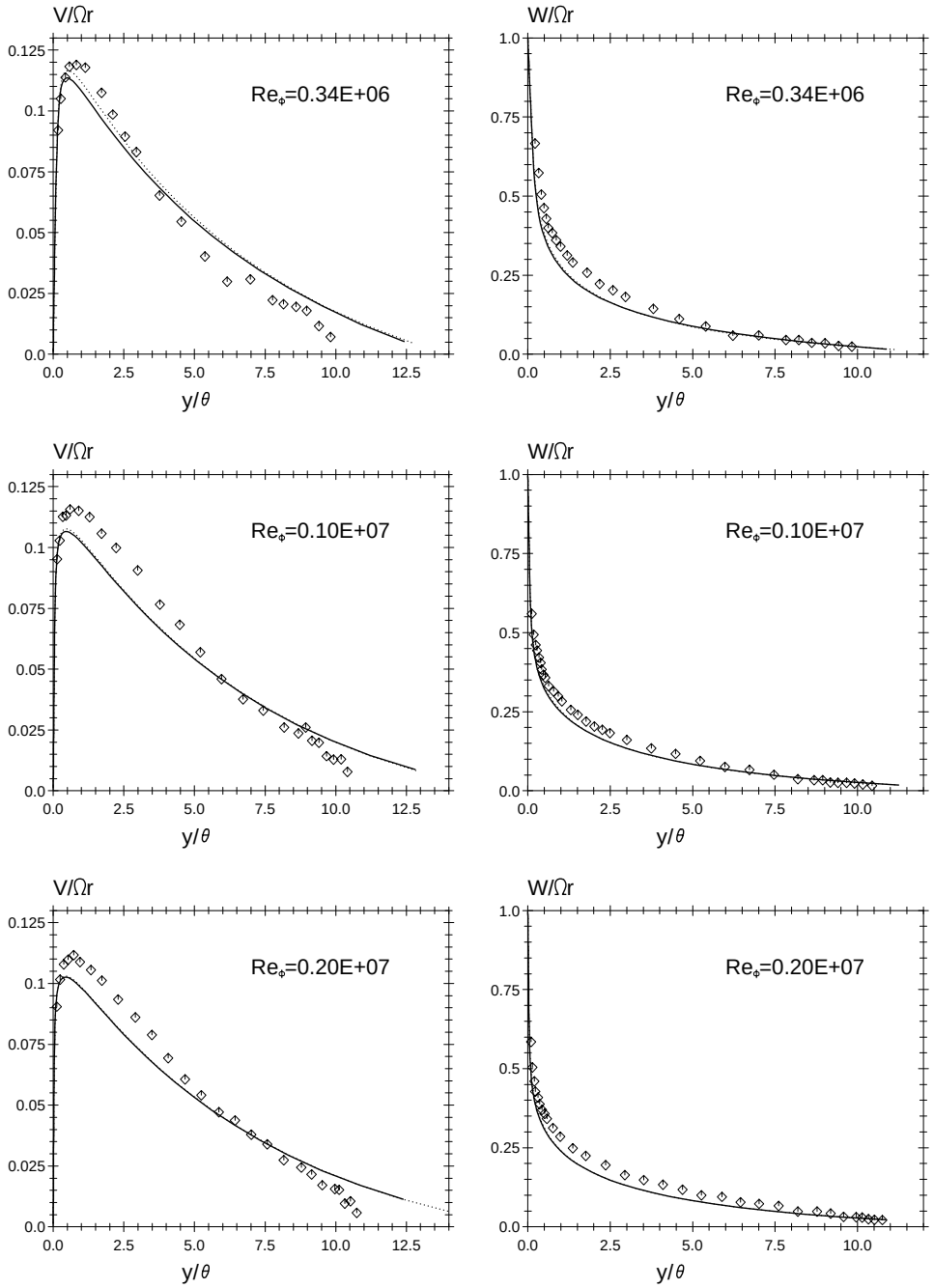

Figure 6.55: Radial and tangential velocity profiles in the free-disc flow using the low-Reynolds-number linear $k-\varepsilon$ model of Launder & Sharma and the non-linear $k-\varepsilon$ model of Craft *et al*. [67] at three different rotational Reynolds numbers; ——: NLEVM; .....: linear $k-\varepsilon$; ◊: Cham & Head experiments.

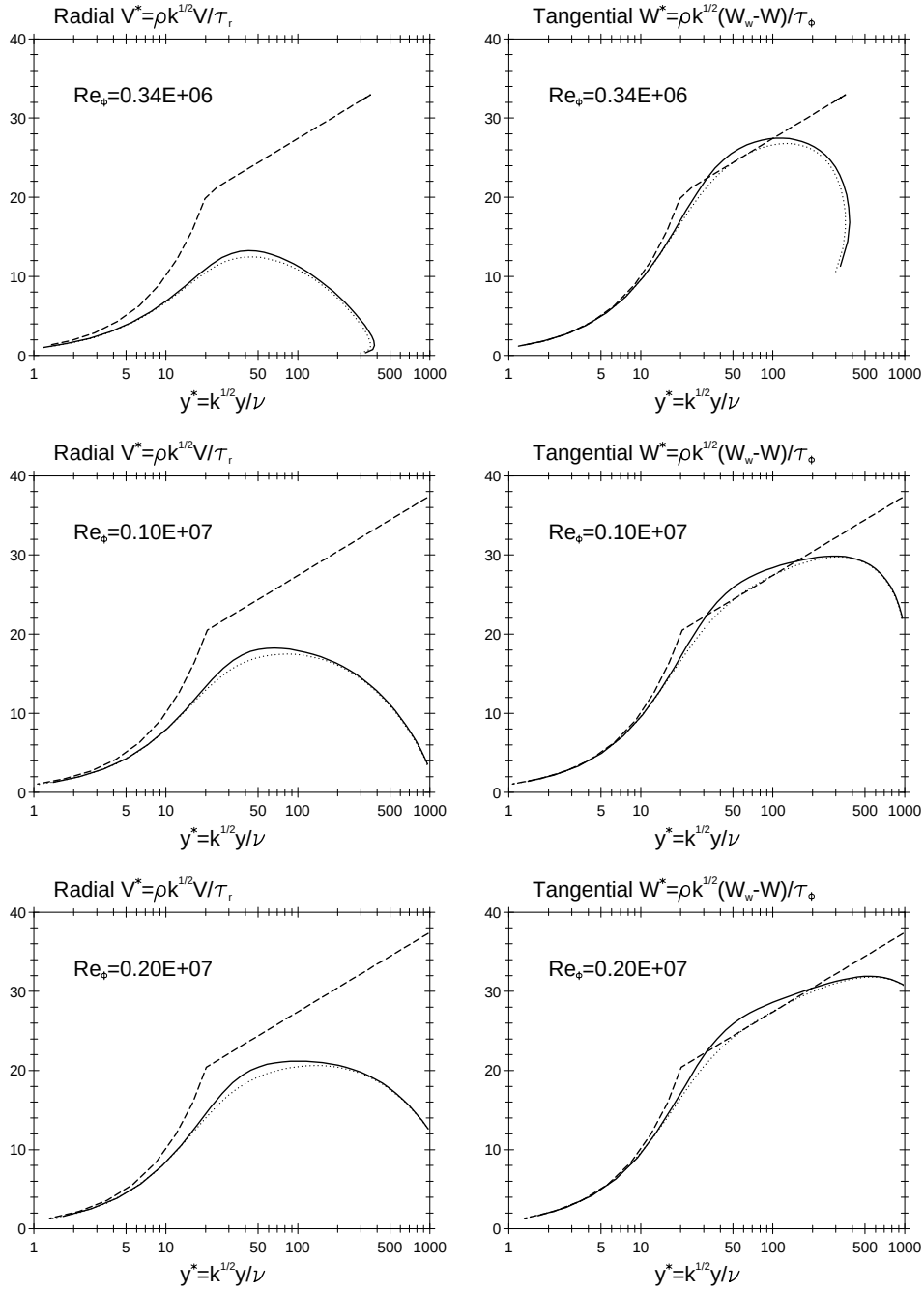

Figure 6.56: Radial and tangential velocity profiles in the free-disc flow using the low-Reynolds-number linear $k-\varepsilon$ model of Launder & Sharma and the non-linear $k-\varepsilon$ model of Craft *et al*. [67] at three different rotational Reynolds numbers; ——: NLEVM; .....: linear $k-\varepsilon$; - - -: "universal" log-law.

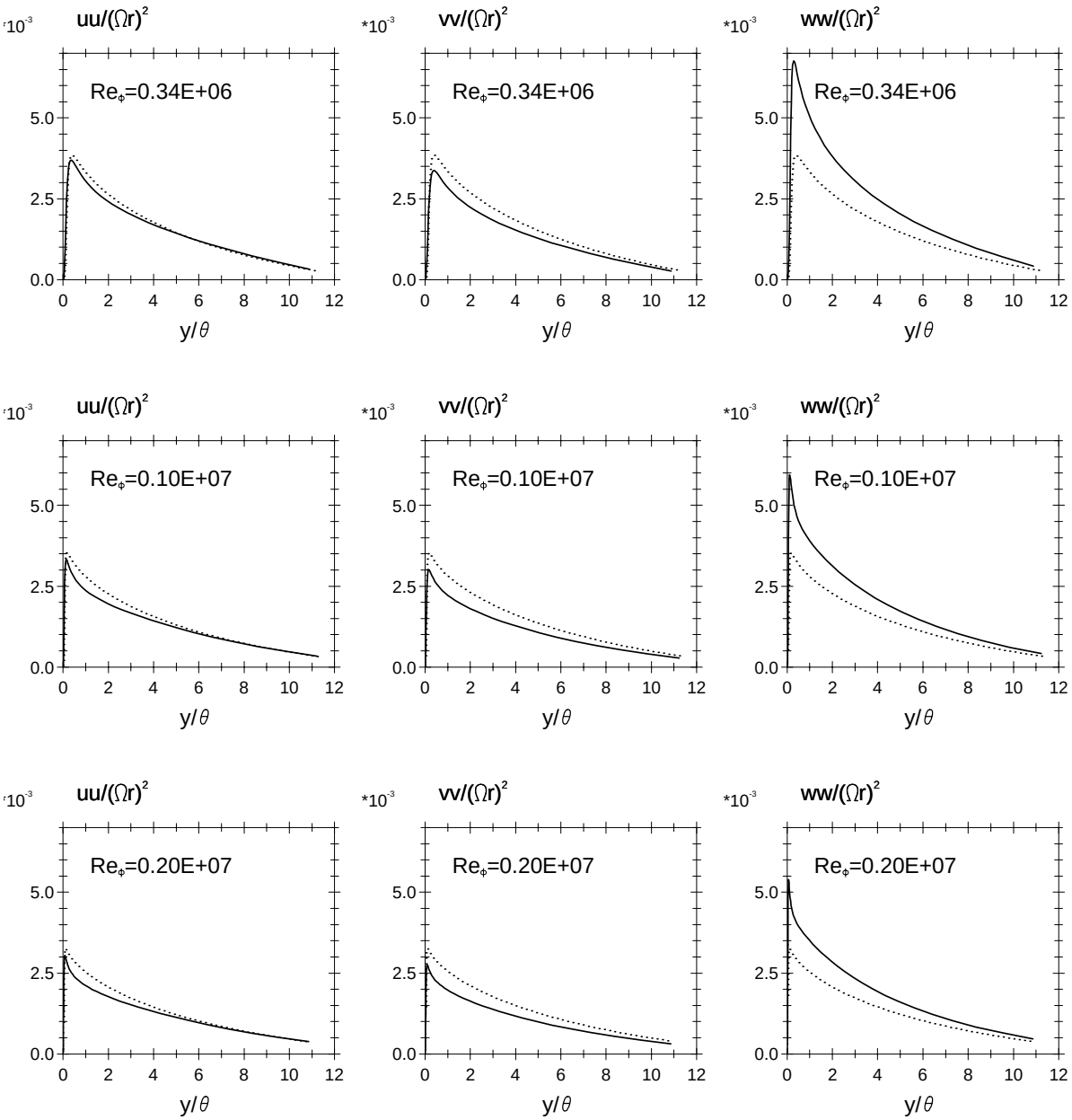

Figure 6.57: Predicted normal stresses (non-dimensionalized with the square of the local wall velocity) in the free-disc flow using the low-Reynolds-number linear $k-\varepsilon$ model of Launder & Sharma and the non-linear $k-\varepsilon$ model of Craft *et al*. [67] at three different rotational Reynolds numbers; ——: NLEVM; .....: linear $k-\varepsilon$.

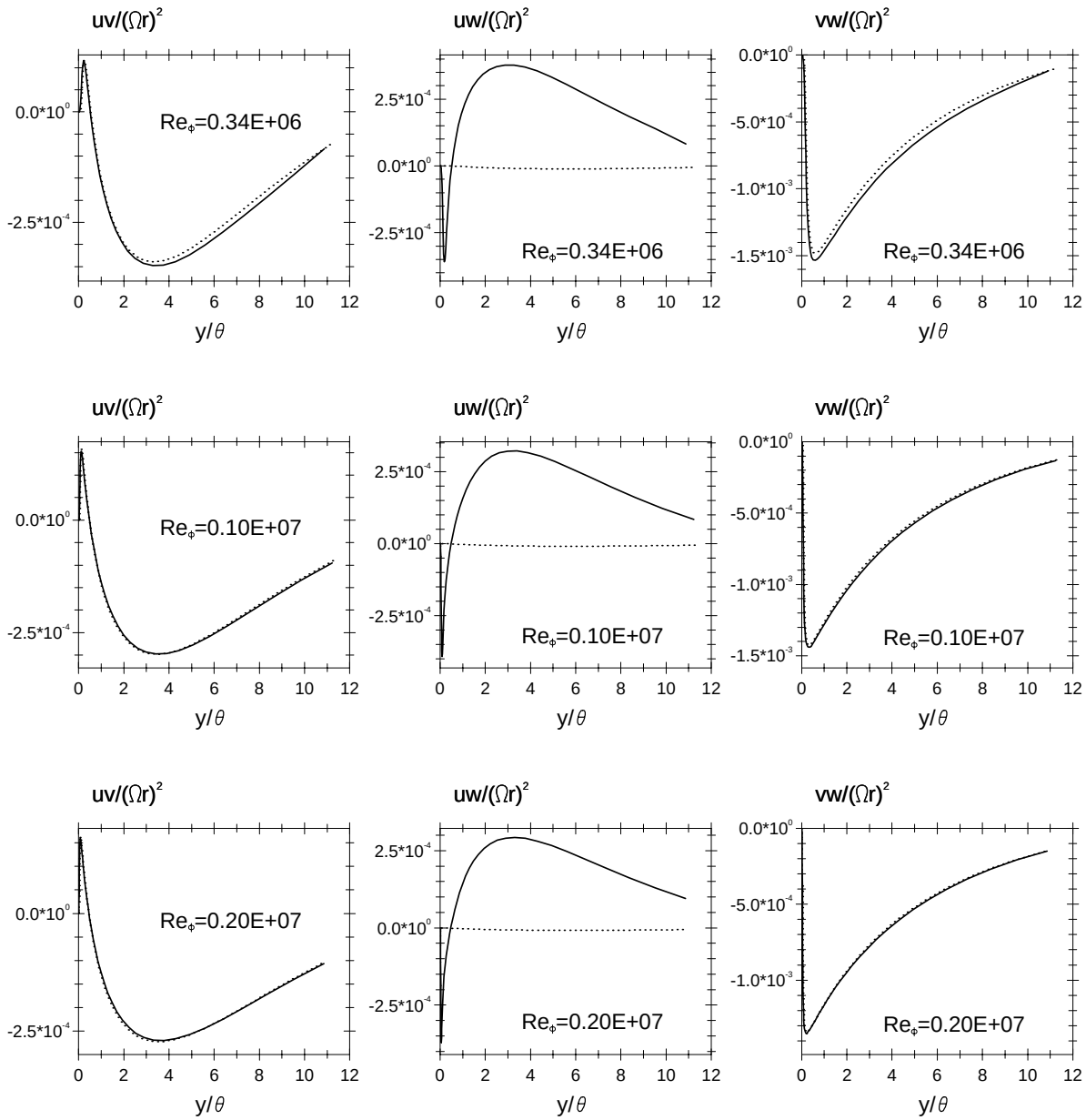

Figure 6.58: Predicted shear stresses (non-dimensionalized with the square of the local wall velocity) in the free-disc flow using the low-Reynolds-number linear $k-\varepsilon$ model of Launder & Sharma and the non-linear $k-\varepsilon$ model of Craft *et al*. [67] at three different rotational Reynolds numbers; ——: NLEVM; .....: linear $k-\varepsilon$.

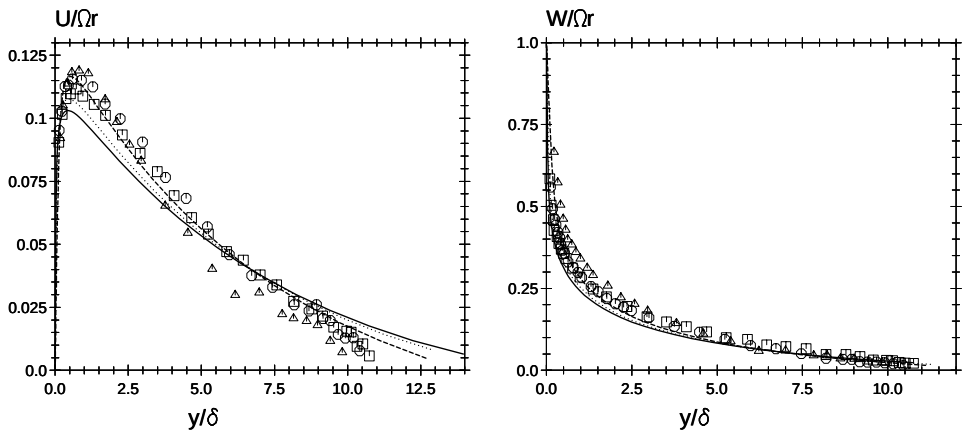

Figure 6.59: Radial and tangential velocity profiles in the free-disc flow using the low-Reynolds-number linear $k-\varepsilon$ model of Launder & Sharma at three different rotational Reynolds numbers, shown in Figure 6.55, overlaid on the same set of axes (lines indicate computational results and symbols are experimental measurements by Cham & Head); —— and □: $Re_\phi = 2\times10^6$; ..... and ○: $Re_\phi = 1\times10^6$; - - - and △: $Re_\phi = 3.4\times10^5$.

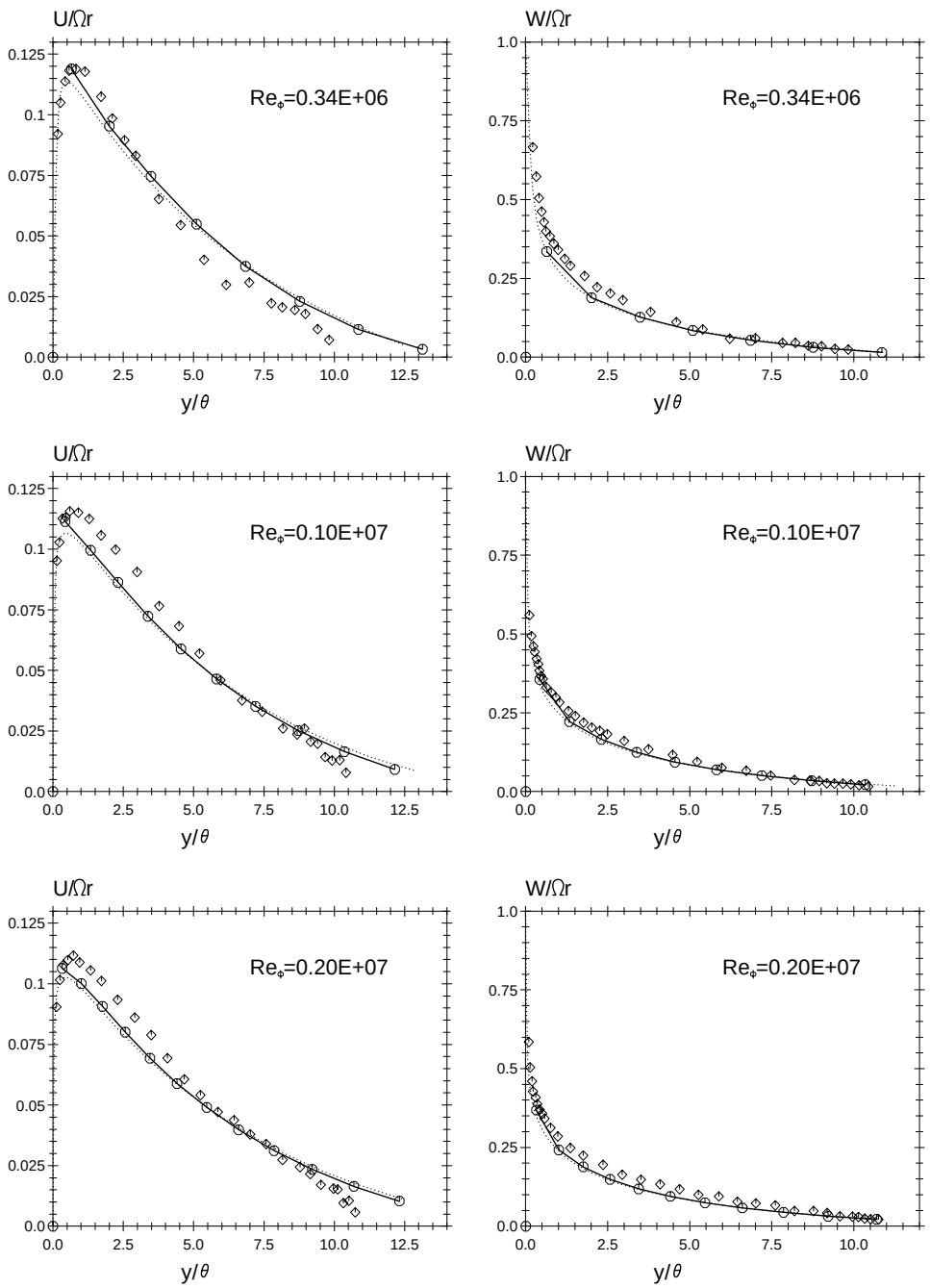

Figure 6.60: Radial and tangential velocity profiles in the free-disc flow using the TEAM wall function and non-linear $k-\varepsilon$ model with the 120×28 grid; —⊖—: high-*Re* model prediction (circles indicate the position of nodes); .....: low-*Re* model prediction; ◊: Cham & Head experiments.

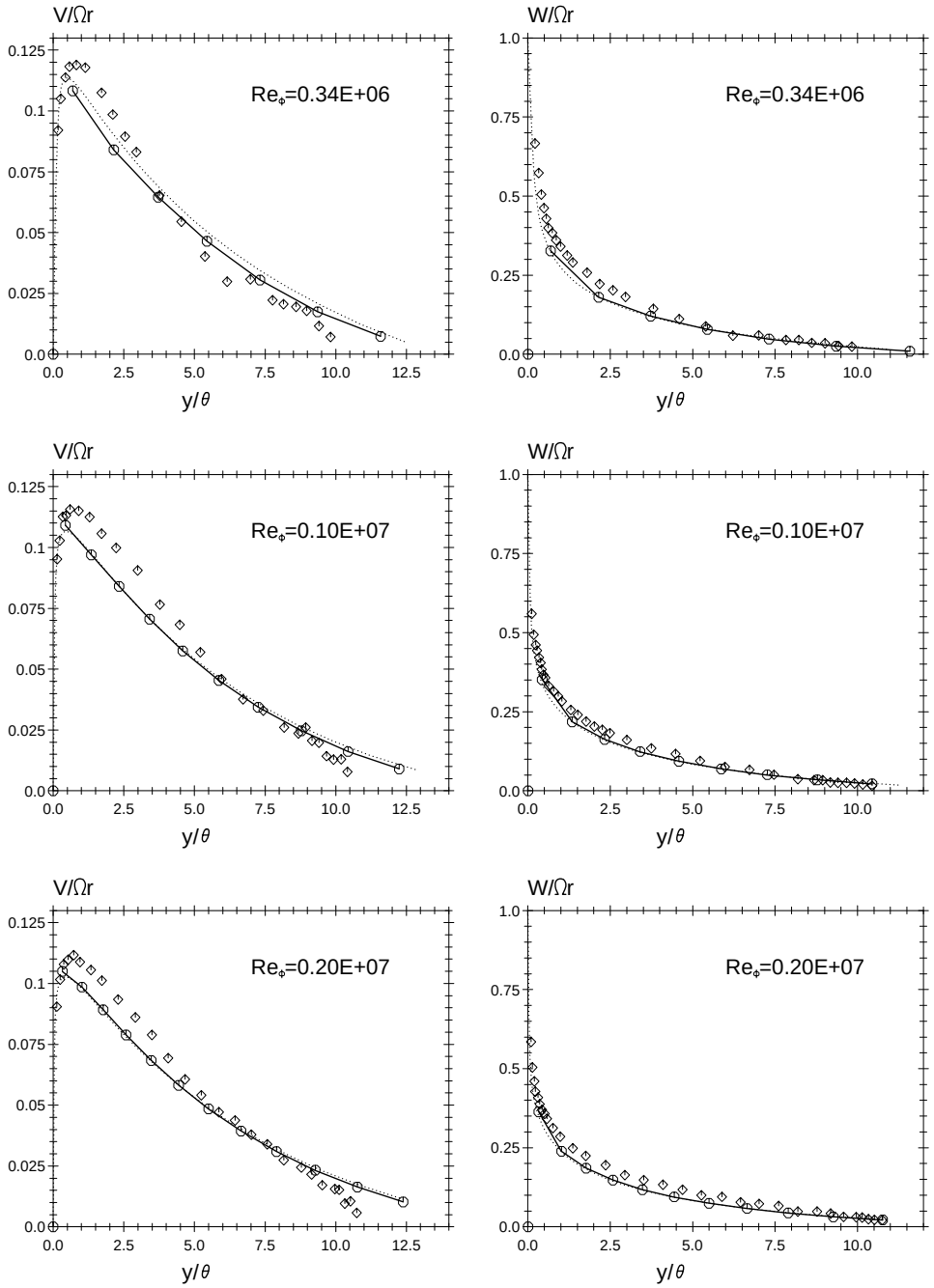

Figure 6.61: Radial and tangential velocity profiles in the free-disc flow using the simplified Chieng & Launder wall function and non-linear $k-\varepsilon$ model with the 120×28 grid; —⊖—: high-*Re* model prediction (circles indicate the position of nodes); .....: low-*Re* model prediction; ◊: Cham & Head experiments.

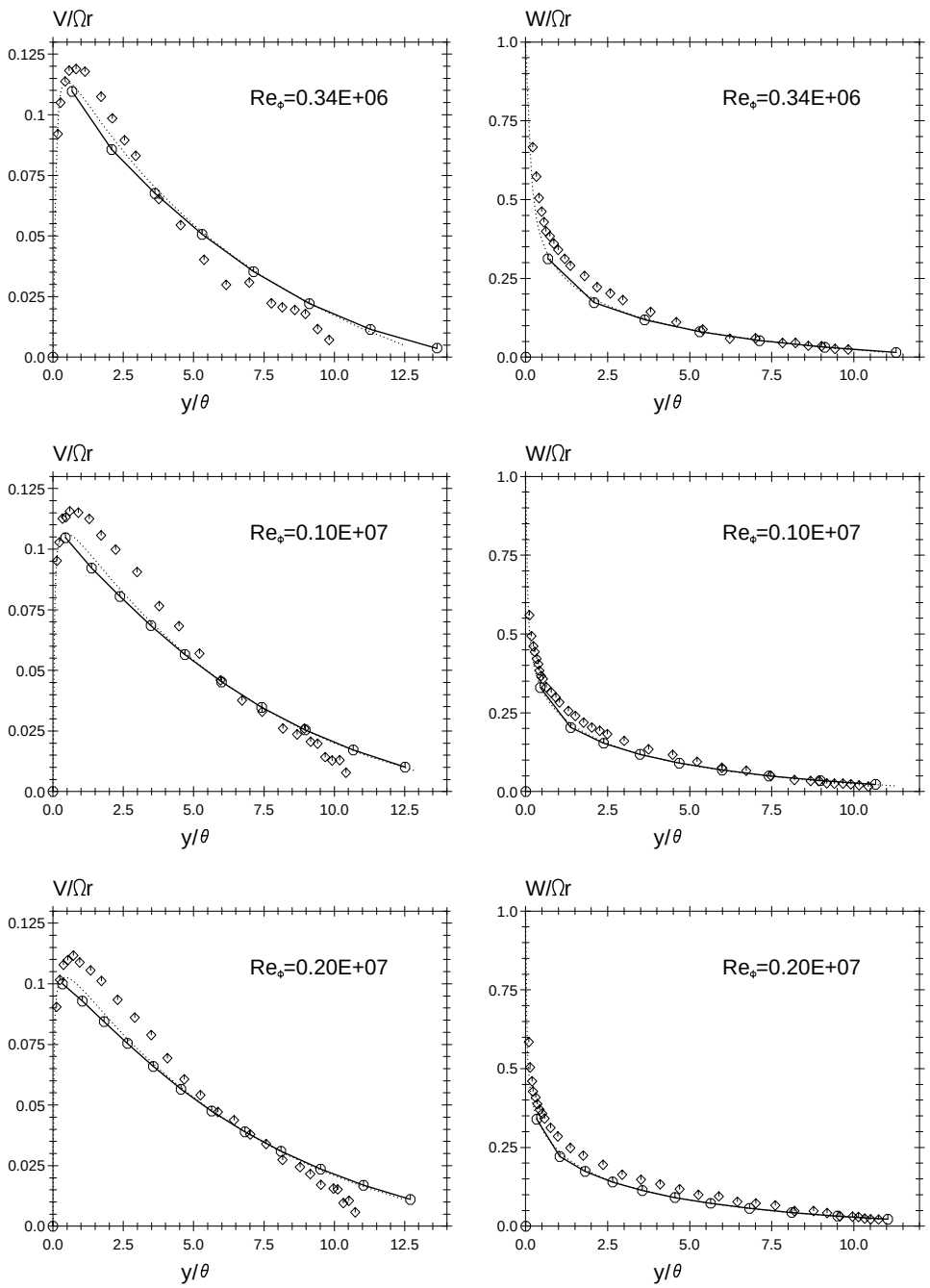

Figure 6.62: Radial and tangential velocity profiles in the free-disc flow using the Chieng & Launder wall function and non-linear $k-\varepsilon$ model with the 120×28 grid; —⊖—: high-*Re* model prediction (circles indicate the position of nodes); .....: low-*Re* model prediction; ◊: Cham & Head experiments.

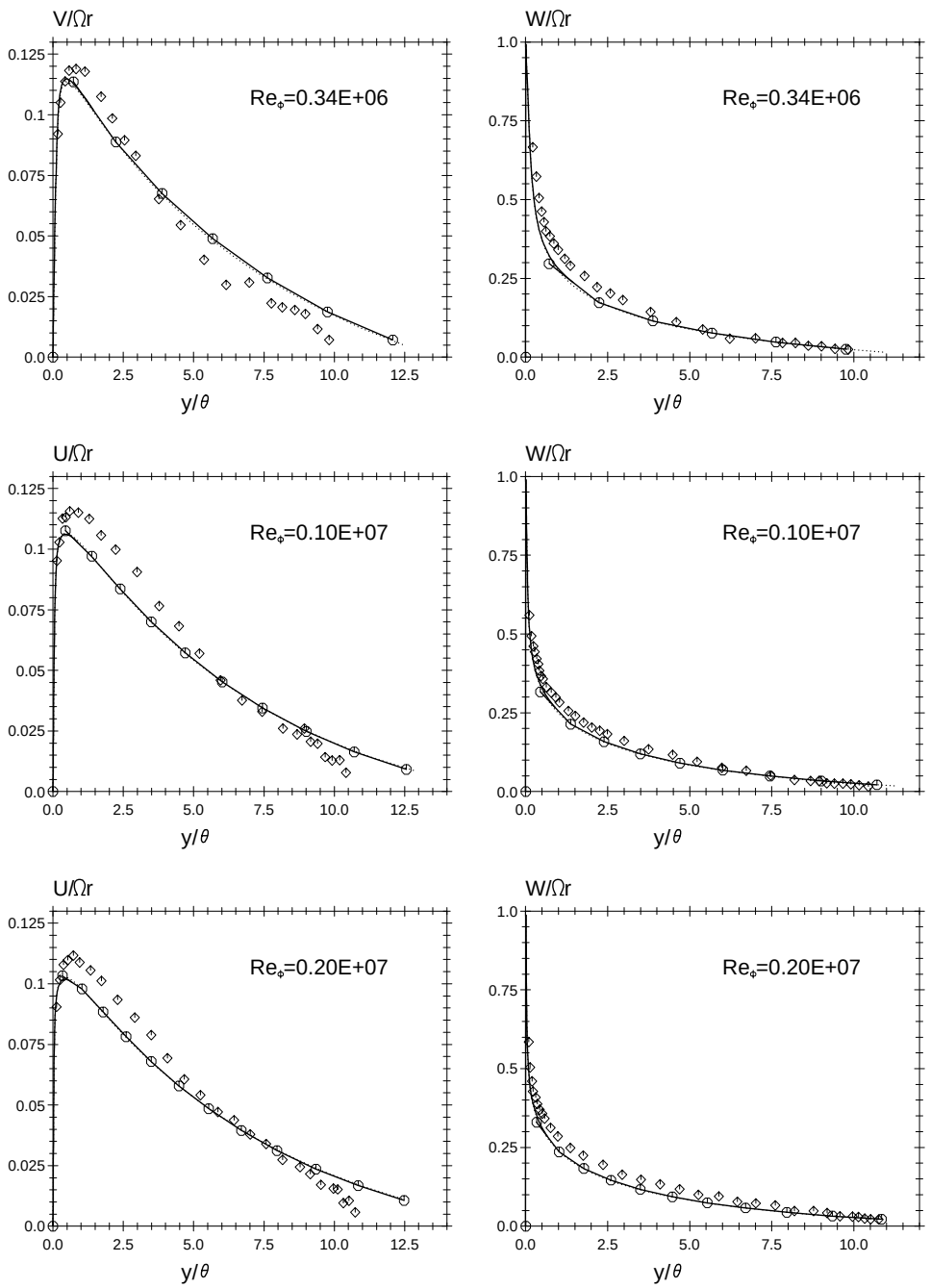

Figure 6.63: Radial and tangential velocity profiles in the free-disc flow using the UMIST-*N* wall function and non-linear $k-\varepsilon$ model with the 120×28 grid; —⊖—: high-*Re* model prediction (circles indicate the position of nodes); .....: low-*Re* model prediction; ◊: Cham & Head experiments.

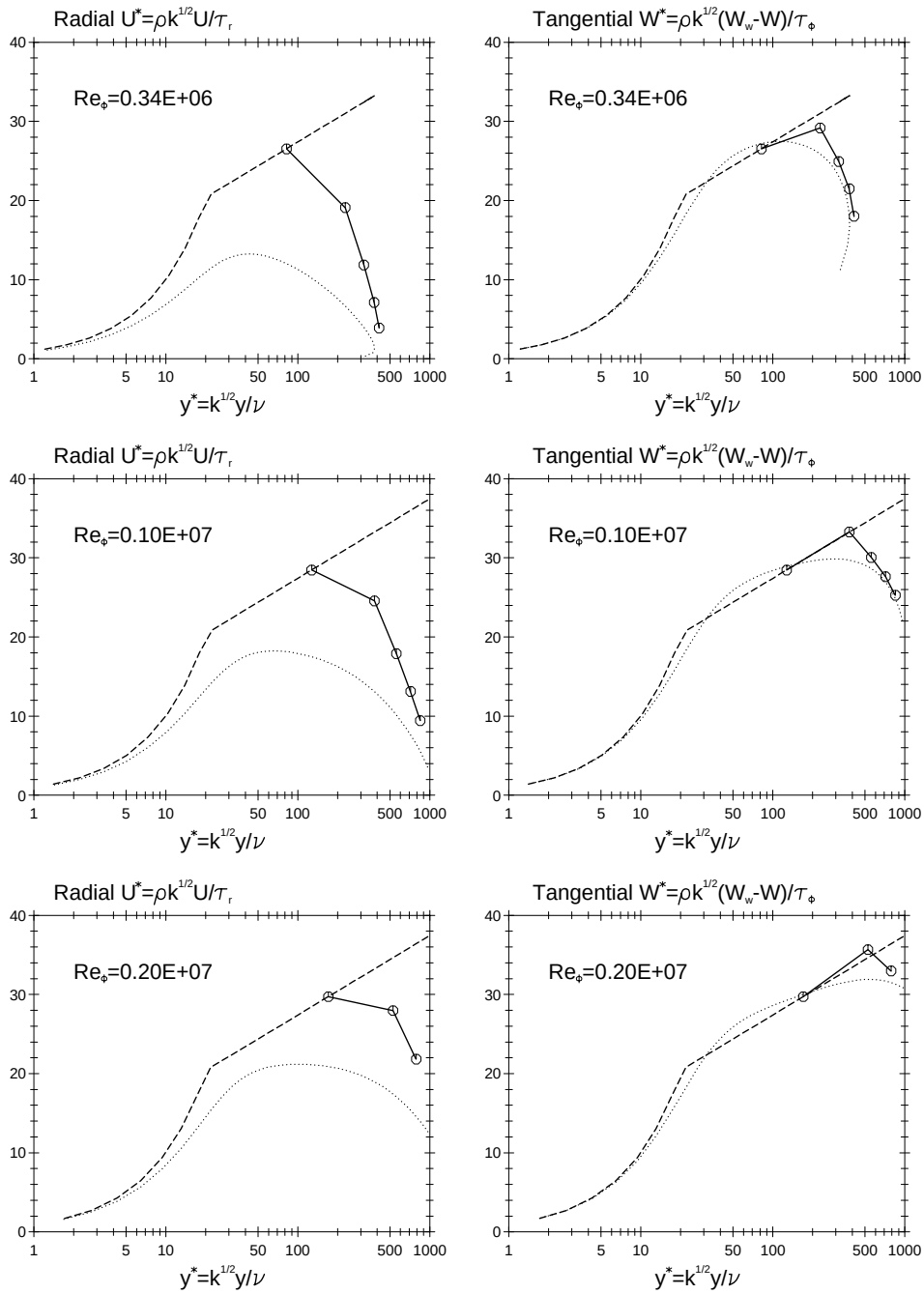

Figure 6.64: Radial and tangential velocity profiles in the free-disc flow using the TEAM wall function and non-linear $k-\varepsilon$ model with the 120×28 grid; —⊖—: high-*Re* model prediction (circles indicate the position of nodes); .....: low-*Re* model prediction; - - -: "universal" log-law.

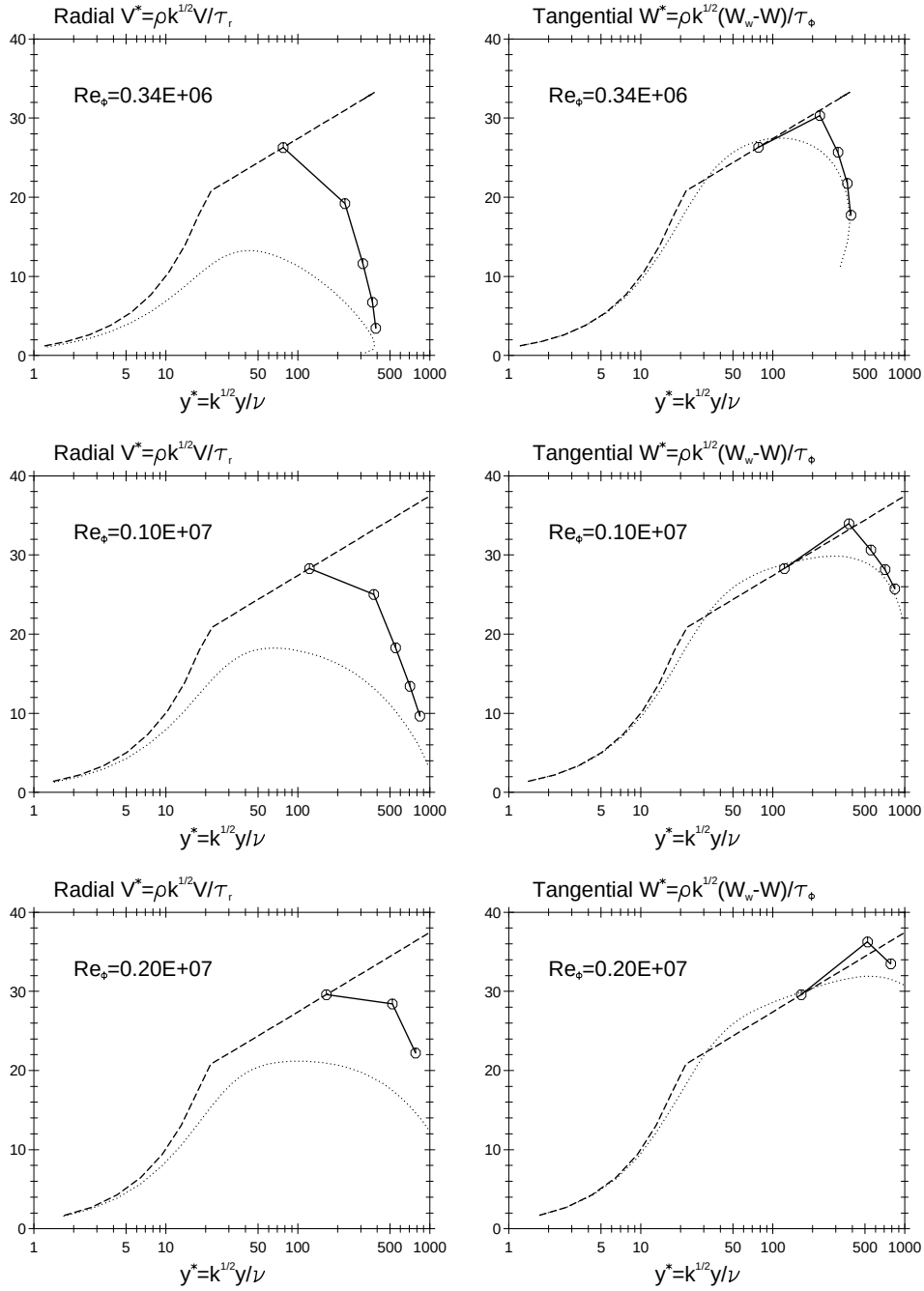

Figure 6.65: Radial and tangential velocity profiles in the free-disc flow using the simplified Chieng & Launder wall function and non-linear $k-\varepsilon$ model with the 120×28 grid; —⊖—: high-*Re* model prediction (circles indicate the position of nodes); .....: low-*Re* model prediction; - - -: "universal" log-law.

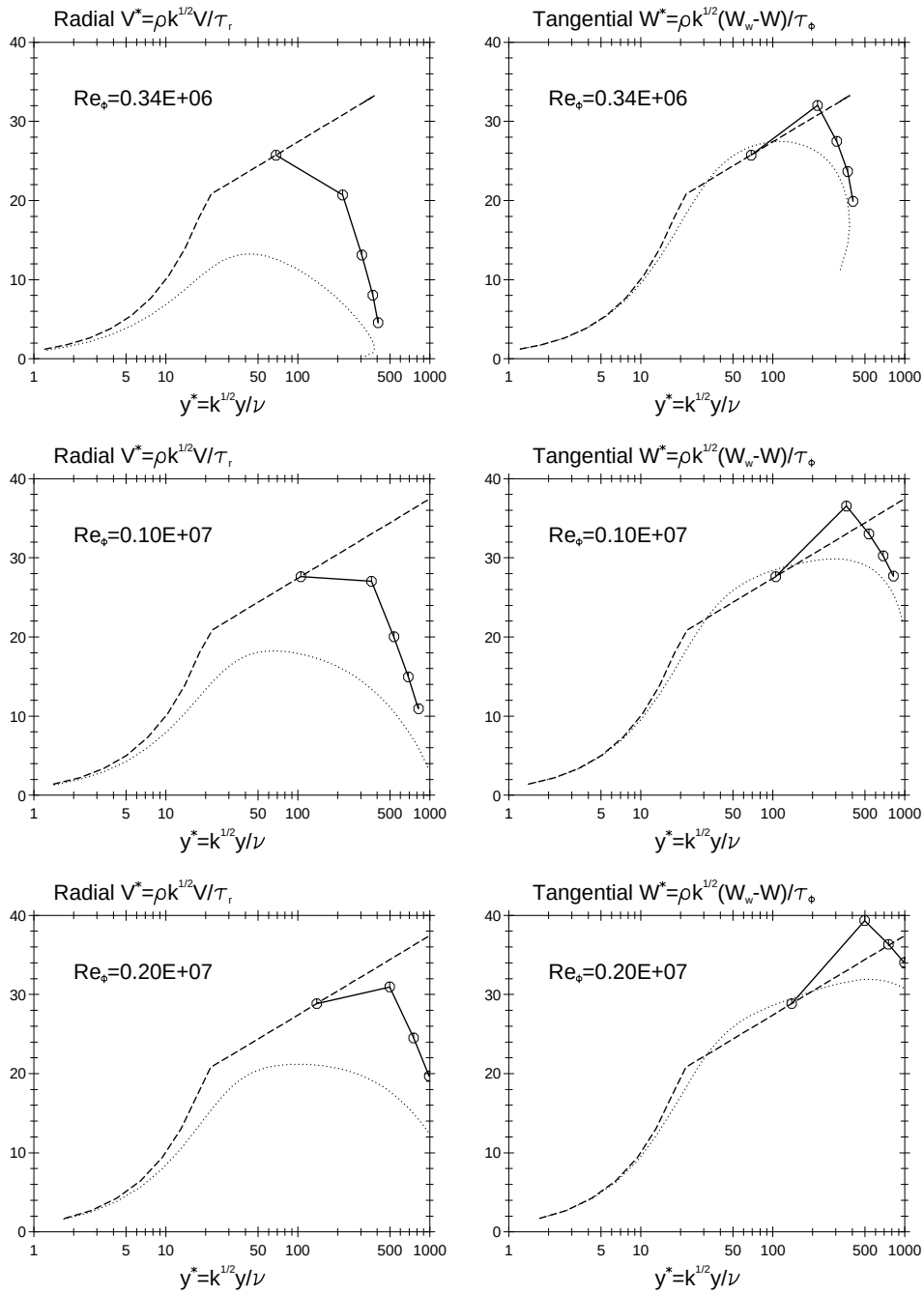

Figure 6.66: Radial and tangential velocity profiles in the free-disc flow using the Chieng & Launder wall function and non-linear $k-\varepsilon$ model with the 120×28 grid; —⊖—: high-*Re* model prediction (circles indicate the position of nodes); .....: low-*Re* model prediction; - - -: "universal" log-law.

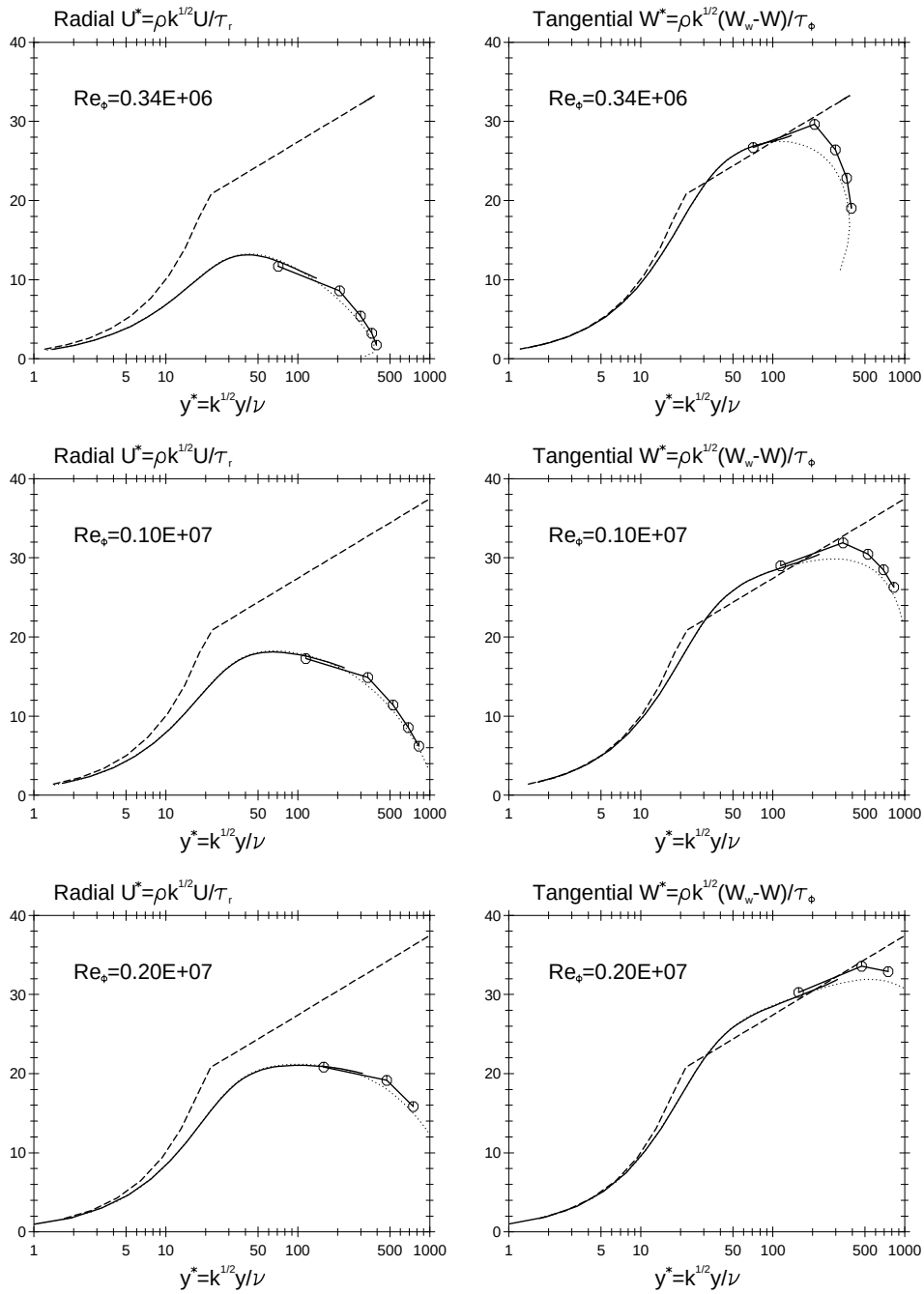

Figure 6.67: Radial and tangential velocity profiles in the free-disc flow using the UMIST-N wall function and non-linear $k-\varepsilon$ model with the 120×28 grid; —⊖—: high-Re model prediction (circles indicate the position of nodes); .....: low-Re model prediction; - - -: "universal" log-law.

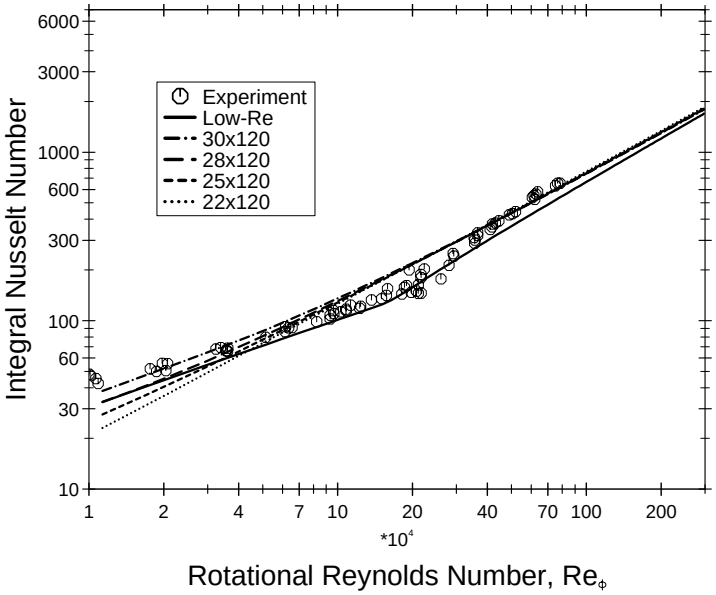

Figure 6.68: Predicted integral Nusselt number in the free-disc flow using the TEAM wall function and non-linear $k-\varepsilon$ model. Solid line: low-*Re* model; broken lines: wall function results for different grid arrangements; ○: experimental values from Cobb & Saunders [130].

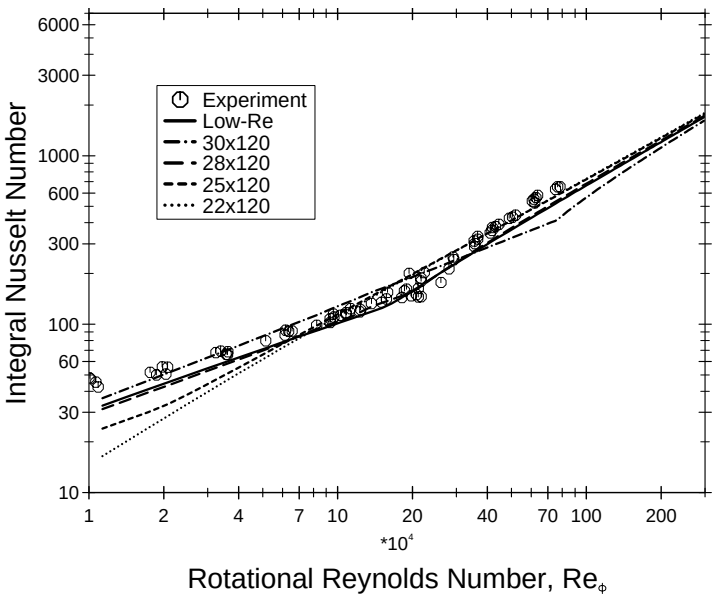

Figure 6.69: Predicted integral Nusselt number in the free-disc flow using the simplified Chieng & Launder wall function and non-linear $k-\varepsilon$ model. Solid line: low-*Re* model; broken lines: wall function results for different grid arrangements; ○: experimental values from Cobb & Saunders [130].

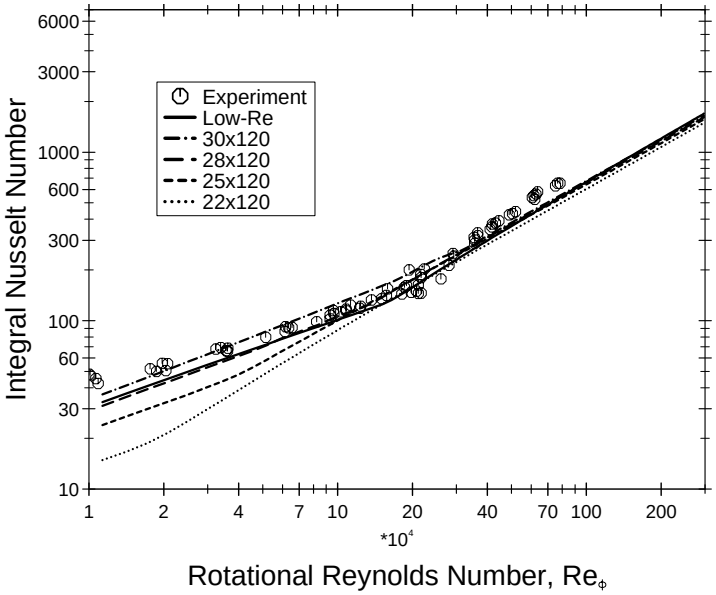

Figure 6.70: Predicted integral Nusselt number in the free-disc flow using the Chieng & Launder wall function and non-linear $k-\varepsilon$ model. Solid line: low-*Re* model; broken lines: wall function results for different grid arrangements; ○: experimental values from Cobb & Saunders [130].

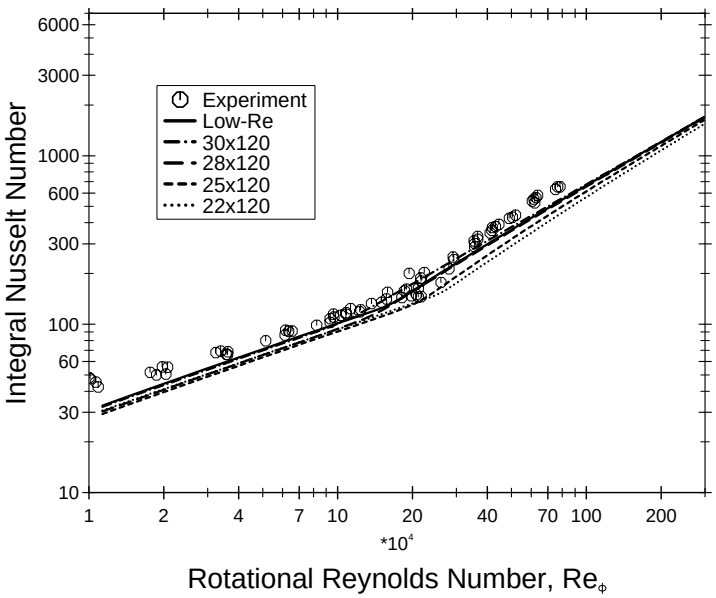

Figure 6.71: Predicted integral Nusselt number in the free-disc flow using the UMIST-*N* wall function and non-linear $k-\varepsilon$ model. Solid line: low-*Re* model; broken lines: wall function results for different grid arrangements; ○: experimental values from Cobb & Saunders [130].

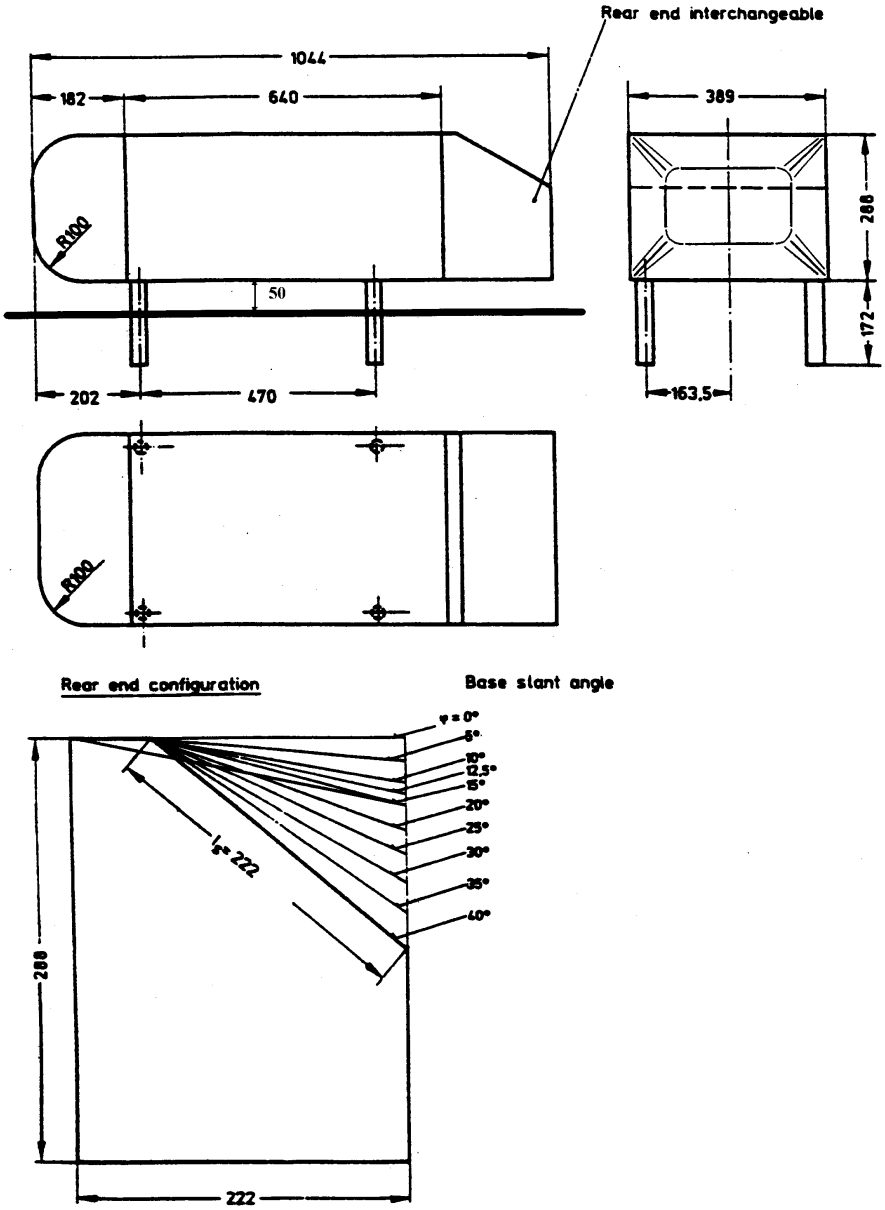

Figure 7.1: Ahmed body geometry (taken from Ahmed *et al*. [137]).

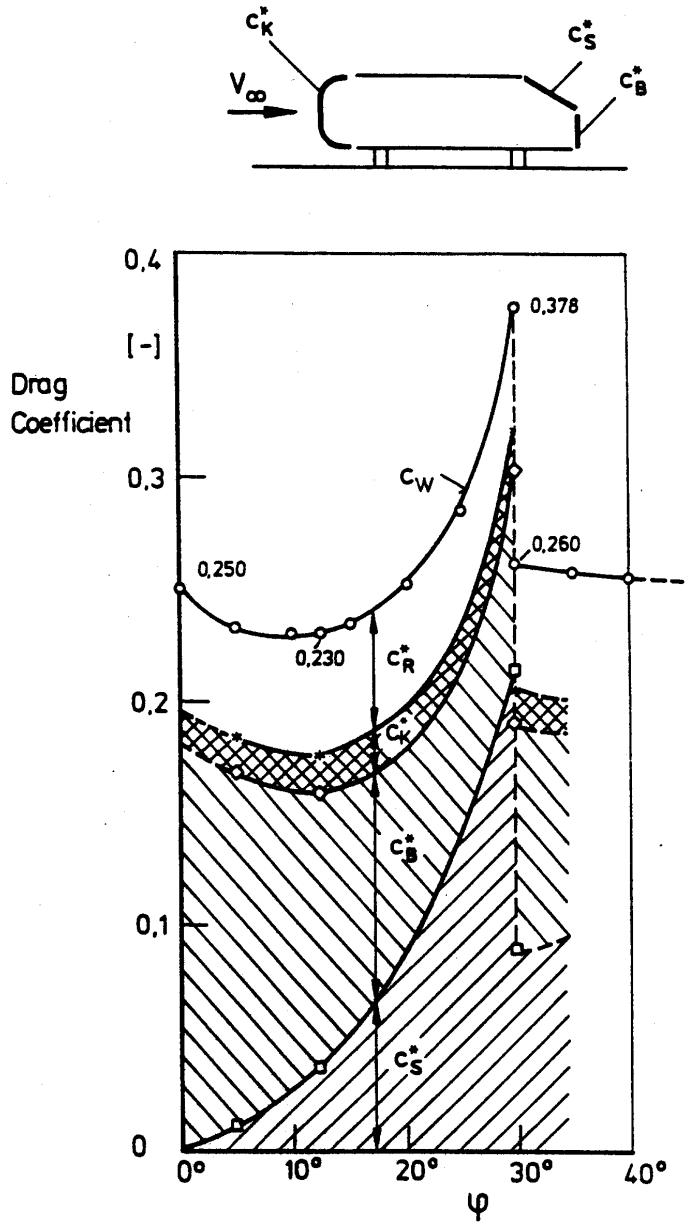

Figure 7.2: Drag breakdown measured by Ahmed *et al*. [137] for varying slant angle, φ.

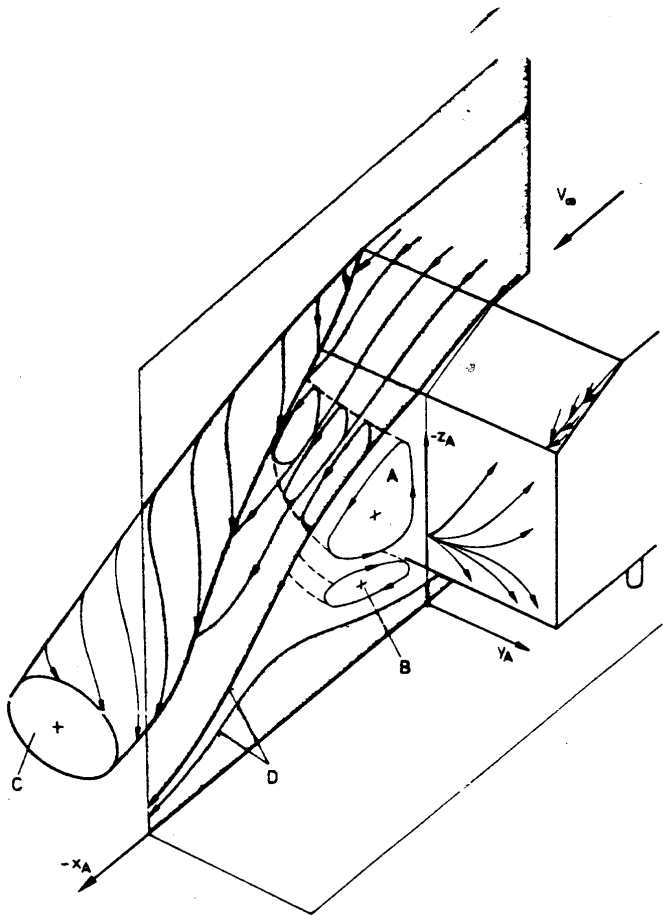

Figure 7.3: Schematic representation of the Ahmed body with low drag flow $\beta \approx 20^\circ$ (taken from Ahmed *et al*. [137]).

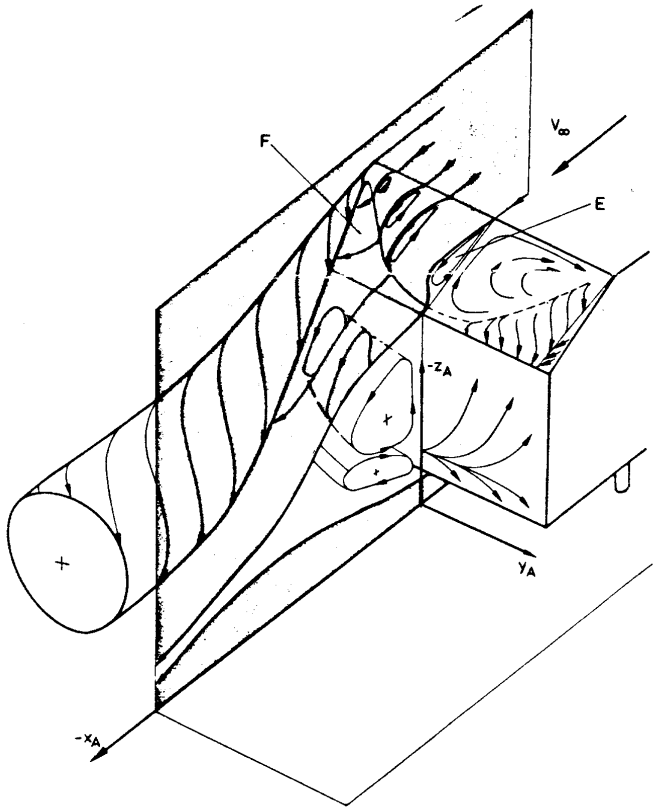

Figure 7.4: Schematic representation of the Ahmed body with high drag flow $\beta = 30^\circ$ (taken from Ahmed *et al*. [137]).

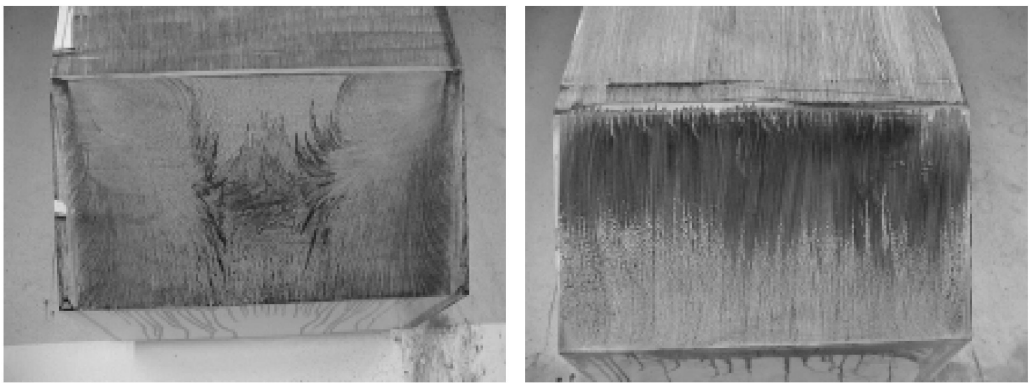

Figure 7.5: Oil/soot streakflow visualization on the rear of the Ahmed body with slant angles 25° (left) and 35° (right) (taken from Lienhart *et al*. [138]).

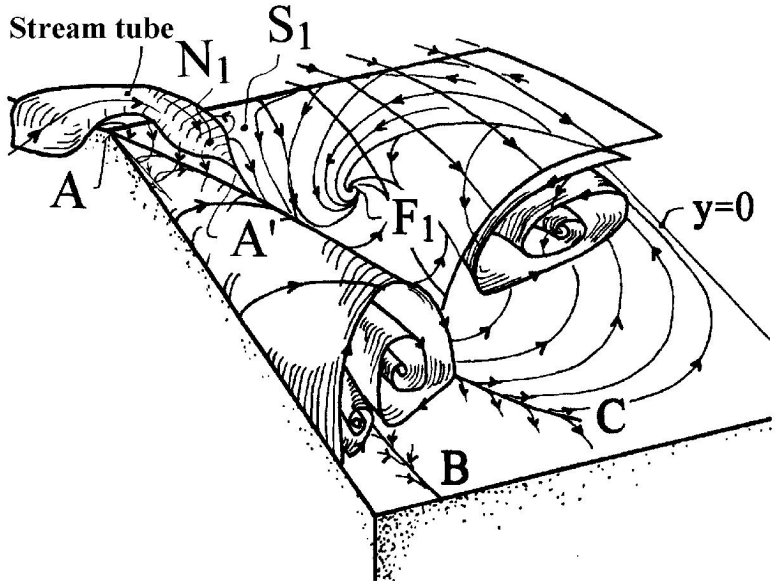

Figure 7.6: Schematic representation of the flow over the 25° rear slant of the Ahmed body (taken from from Spohn & Gilliéron. [139]).

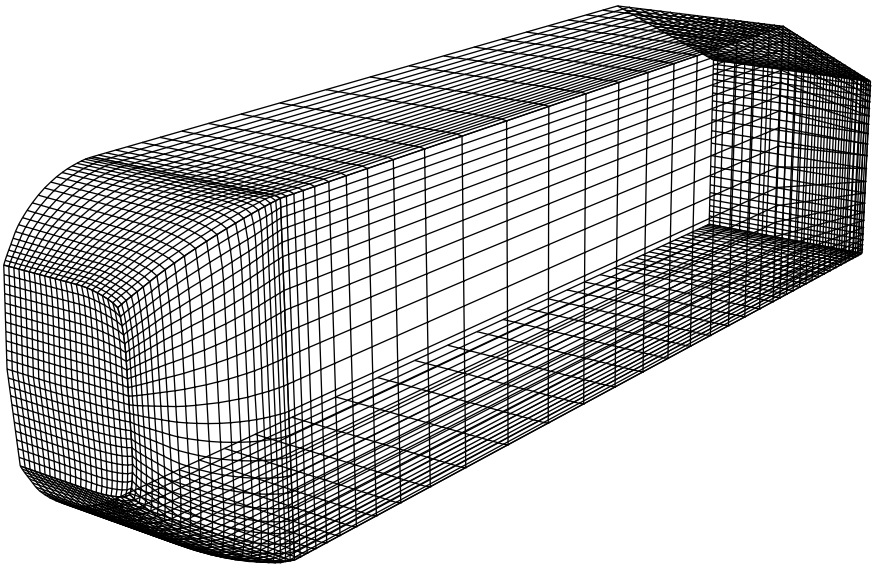

Figure 7.7: Grid on nose cone and front portion of Ahmed body (taken from Robinson [35]).

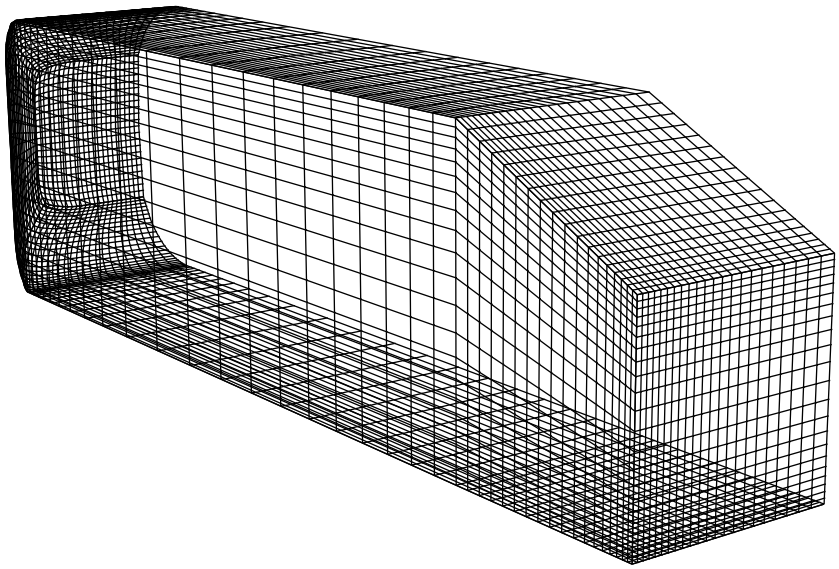

Figure 7.8: Grid used on rear section and slant of 25° Ahmed body (taken from Robinson [35]).

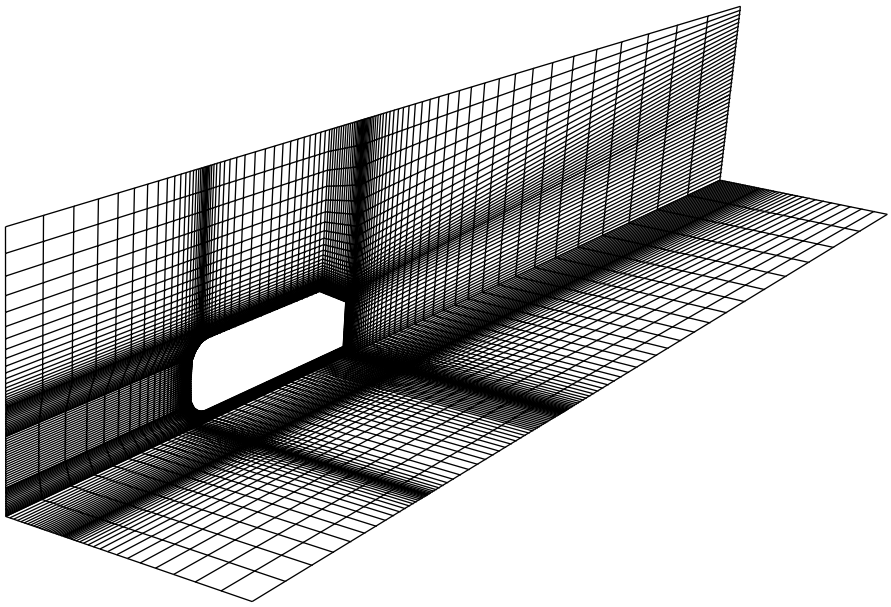

Figure 7.9: Grid on symmetry plane and floor showing some refinement propagated at block boundaries (taken from Robinson [35]).

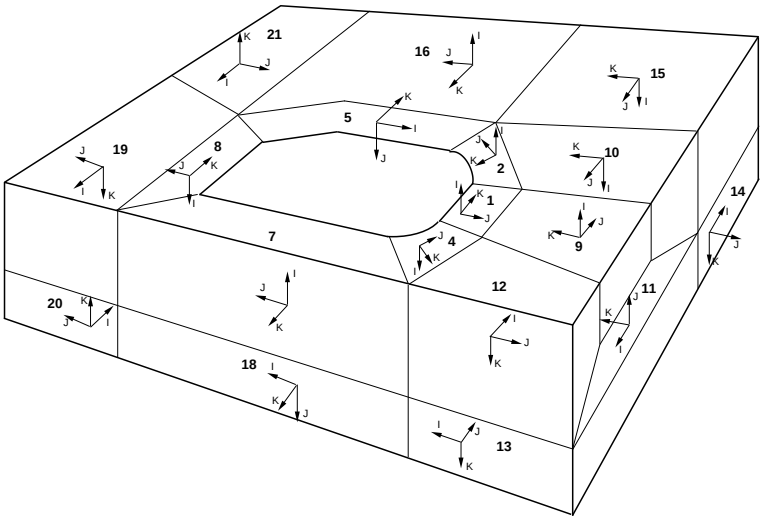

Figure 7.10: Block arrangement for the Ahmed body (25° slant angle) showing block numbers and coordinate frames.

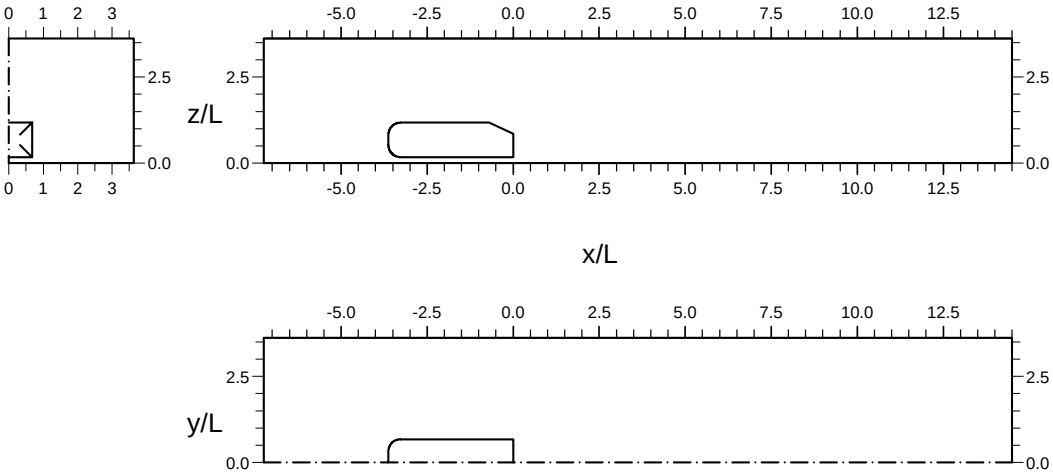

Figure 7.11: Sketch of domain in third angle projection used for Ahmed body calculations (taken from Robinson [35]). Lengths are non-dimensionalized with $L = 0.288$m, the height of the body.

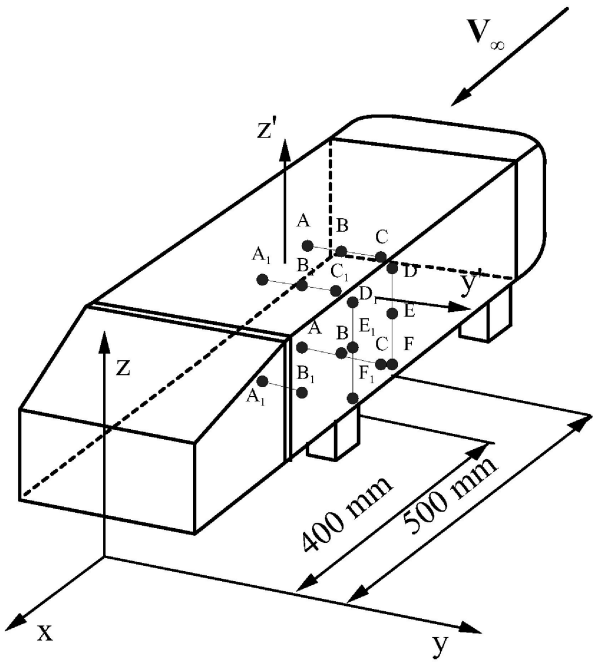

Top	x	y
A	-500	0
A_1	-400	0
B	-500	80
B_1	-400	80
C	-500	160
C_1	-400	160

Side	x	z
D	-500	294
D_1	-400	294
E	-500	194
E_1	-400	194
F	-500	94
F_1	-400	94

Down	x	y
A	-500	0
A_1	-400	0
B	-500	80
B_1	-400	80
C	-500	160

Figure 7.12: Sketch showing position of boundary layer measurements on the central part of the Ahmed body (taken from information supplied to participants of the 2002 ERCOFTAC Workshop on Refined Turbulence Modelling).

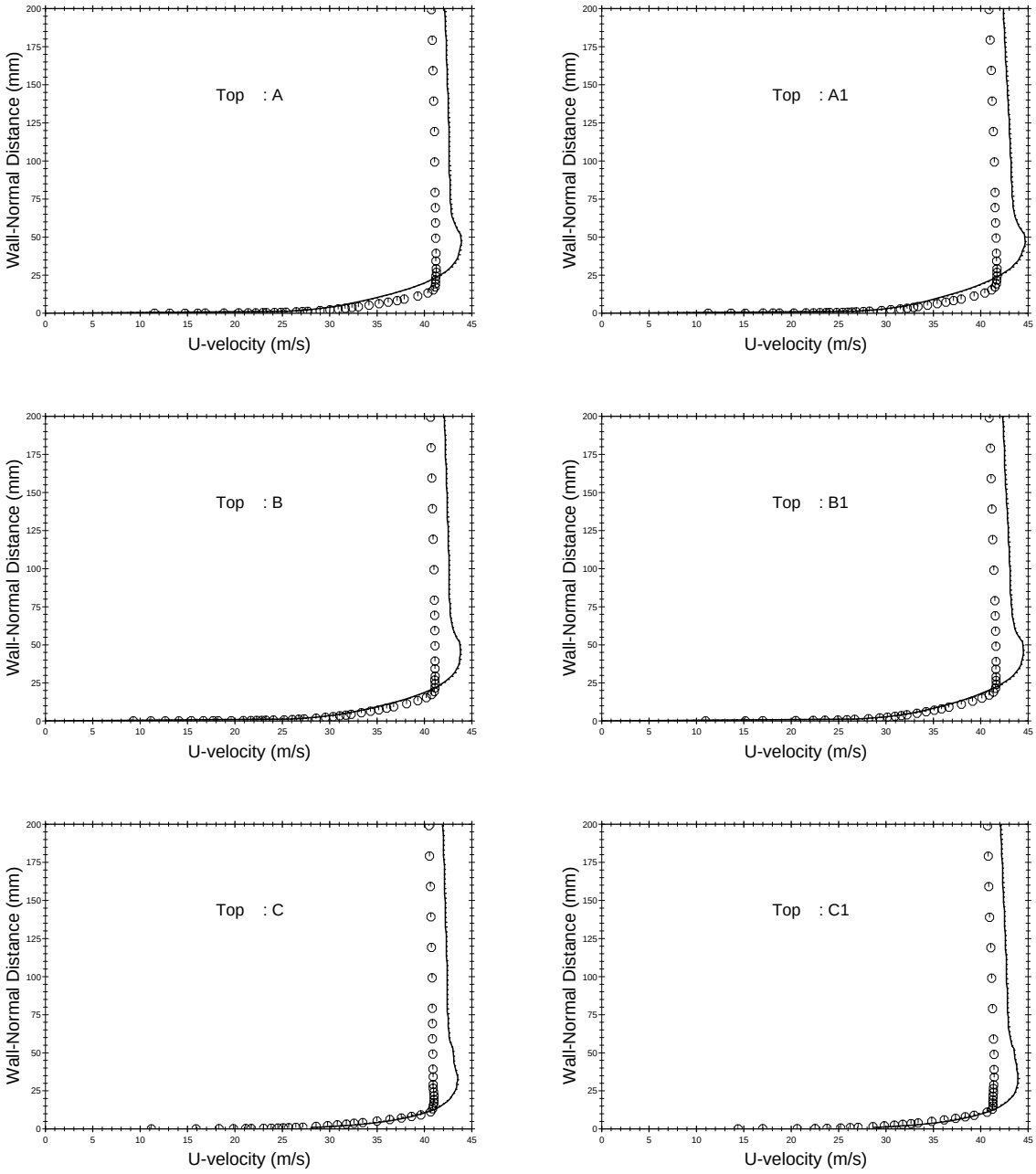

Figure 7.13: Streamwise mean U-velocity profiles at six positions on the top surface of the Ahmed body (for position of points see Figure 7.12), —-: linear $k-\varepsilon$ with SCL wall function; ....: linear $k-\varepsilon$ with UMIST-N wall function; ○: experimental measurements from Lienhart *et al*. [138].

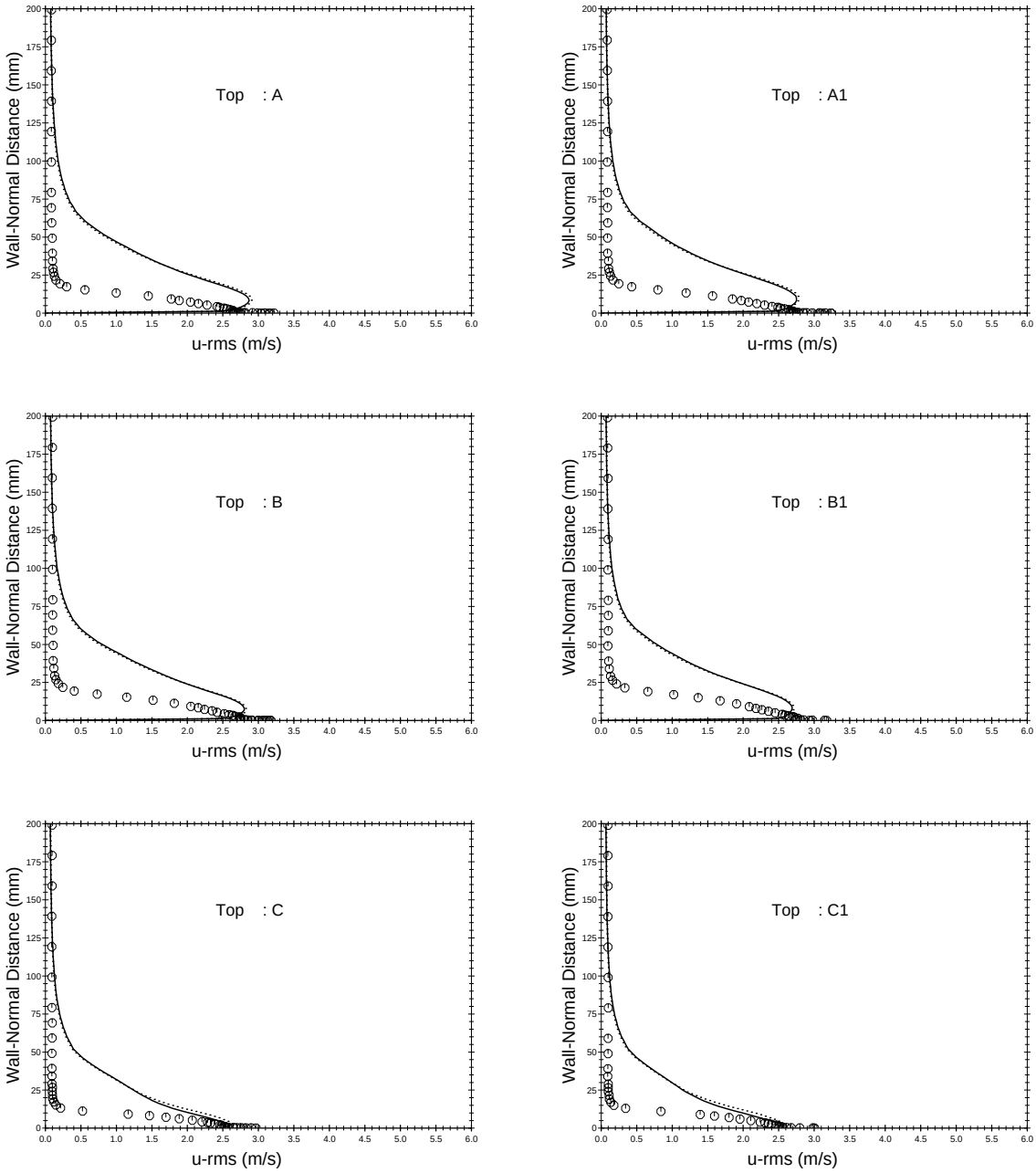

Figure 7.14: Streamwise RMS u'-profiles at six positions on the top surface of the Ahmed body (for position of points see Figure 7.12), —-: linear $k-\varepsilon$ with SCL wall function; ....: linear $k-\varepsilon$ with UMIST-*N* wall function; ○: experimental measurements from Lienhart *et al*. [138].

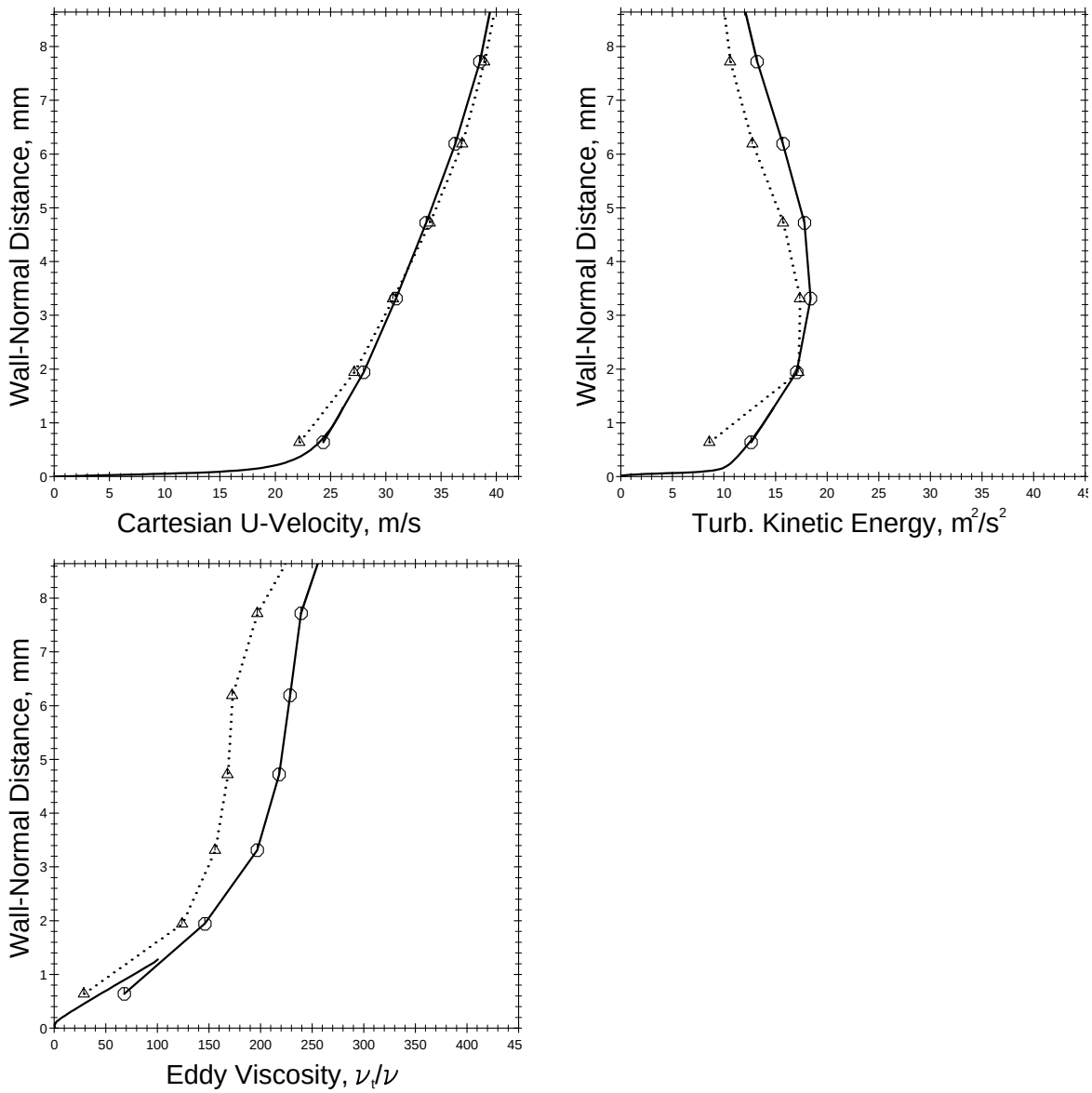

Figure 7.15: Streamwise mean U-velocity, turbulent kinetic energy and eddy-viscosity at $x \approx -831$mm on the top surface and on centreline of the Ahmed body, —○—: linear $k-\varepsilon$ with UMIST-N wall function; ....△....: linear $k-\varepsilon$ with SCL wall function; (symbols indicate position of grid nodes).

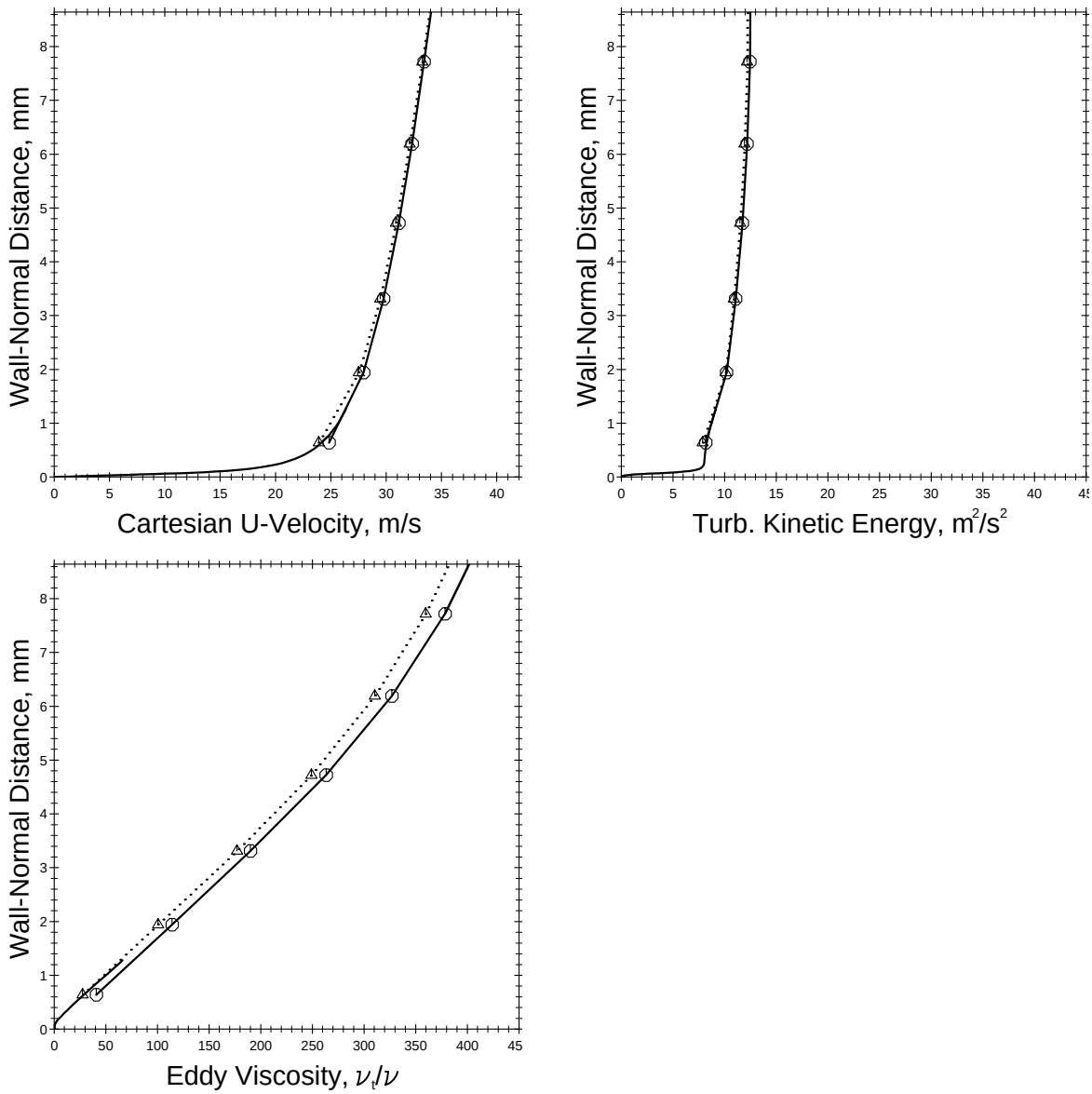

Figure 7.16: Streamwise mean U-velocity, turbulent kinetic energy and eddy-viscosity at $x \approx -475$mm on the top surface and on centreline of the Ahmed body, —⊖—: linear $k-\varepsilon$ with UMIST-N wall function; ....△....: linear $k-\varepsilon$ with SCL wall function; (symbols indicate position of grid nodes).

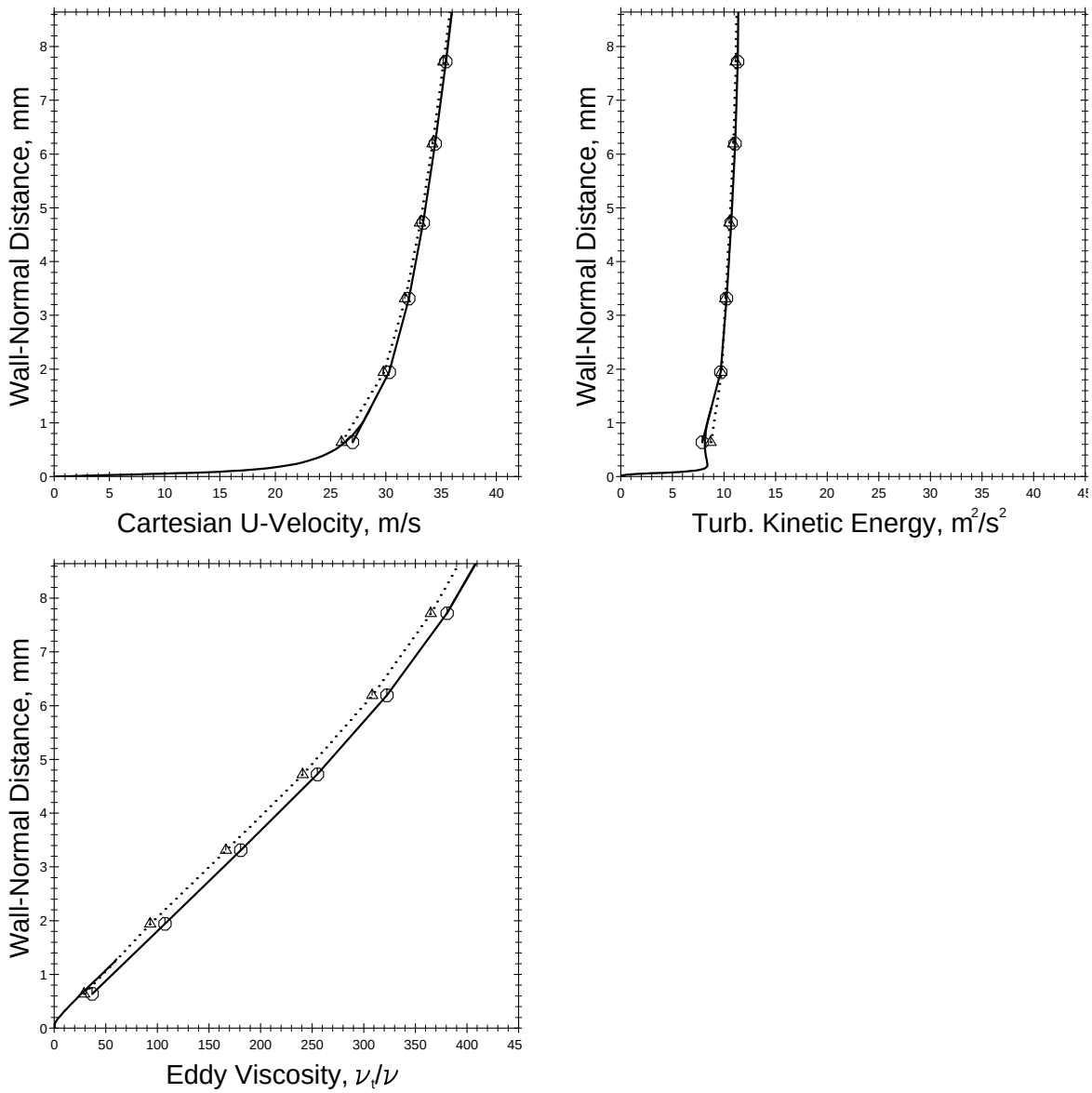

Figure 7.17: Streamwise mean U-velocity, turbulent kinetic energy and eddy-viscosity at $x \approx -346$mm on the top surface and on centreline of the Ahmed body, —○—: linear $k-\varepsilon$ with UMIST-N wall function; ....△....: linear $k-\varepsilon$ with SCL wall function; (symbols indicate position of grid nodes).

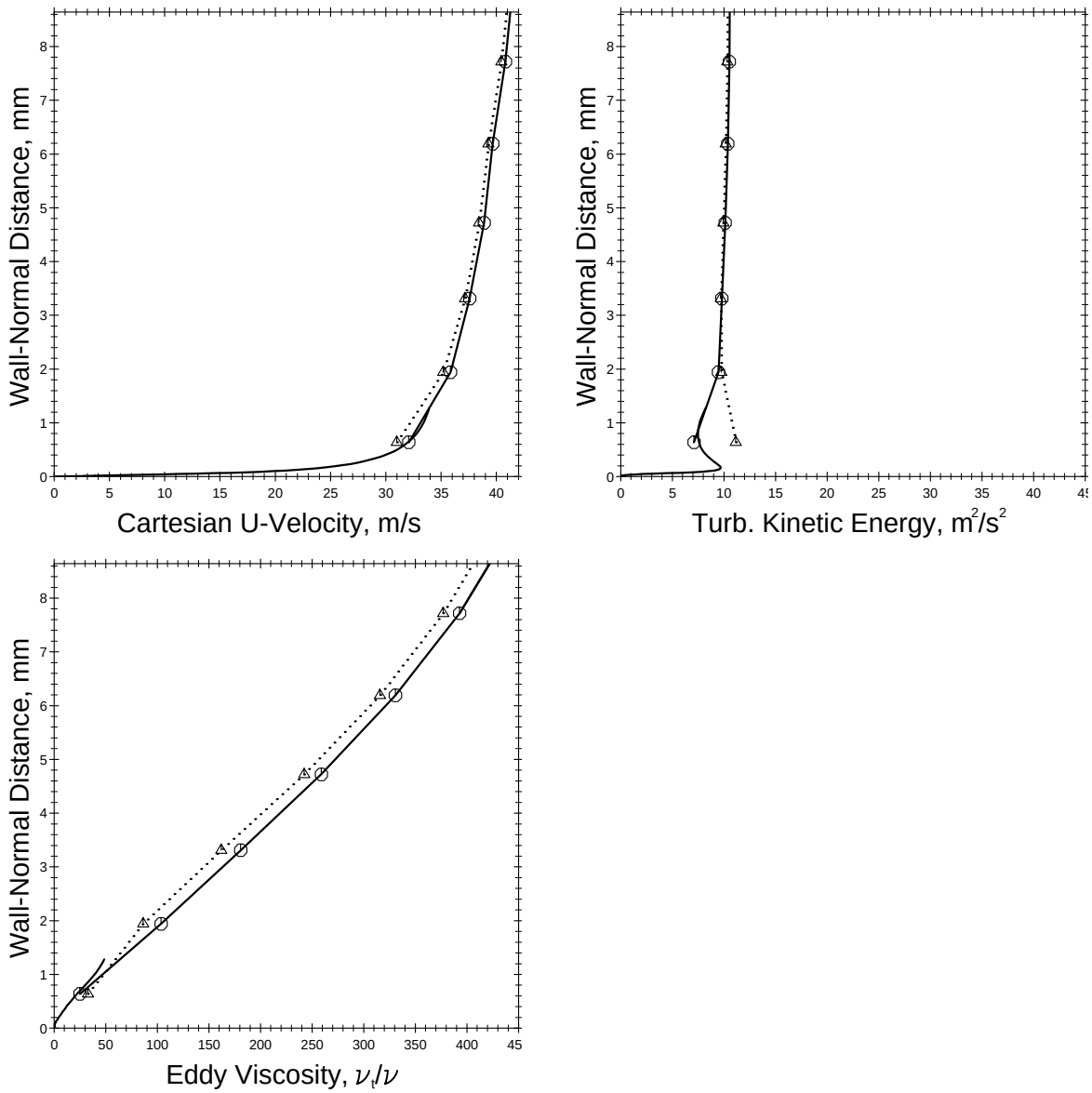

Figure 7.18: Streamwise mean U-velocity, turbulent kinetic energy and eddy-viscosity at $x \approx -244$mm on the top surface and on centreline of the Ahmed body, —○—: linear $k-\varepsilon$ with UMIST-N wall function; ....△....: linear $k-\varepsilon$ with SCL wall function; (symbols indicate position of grid nodes).

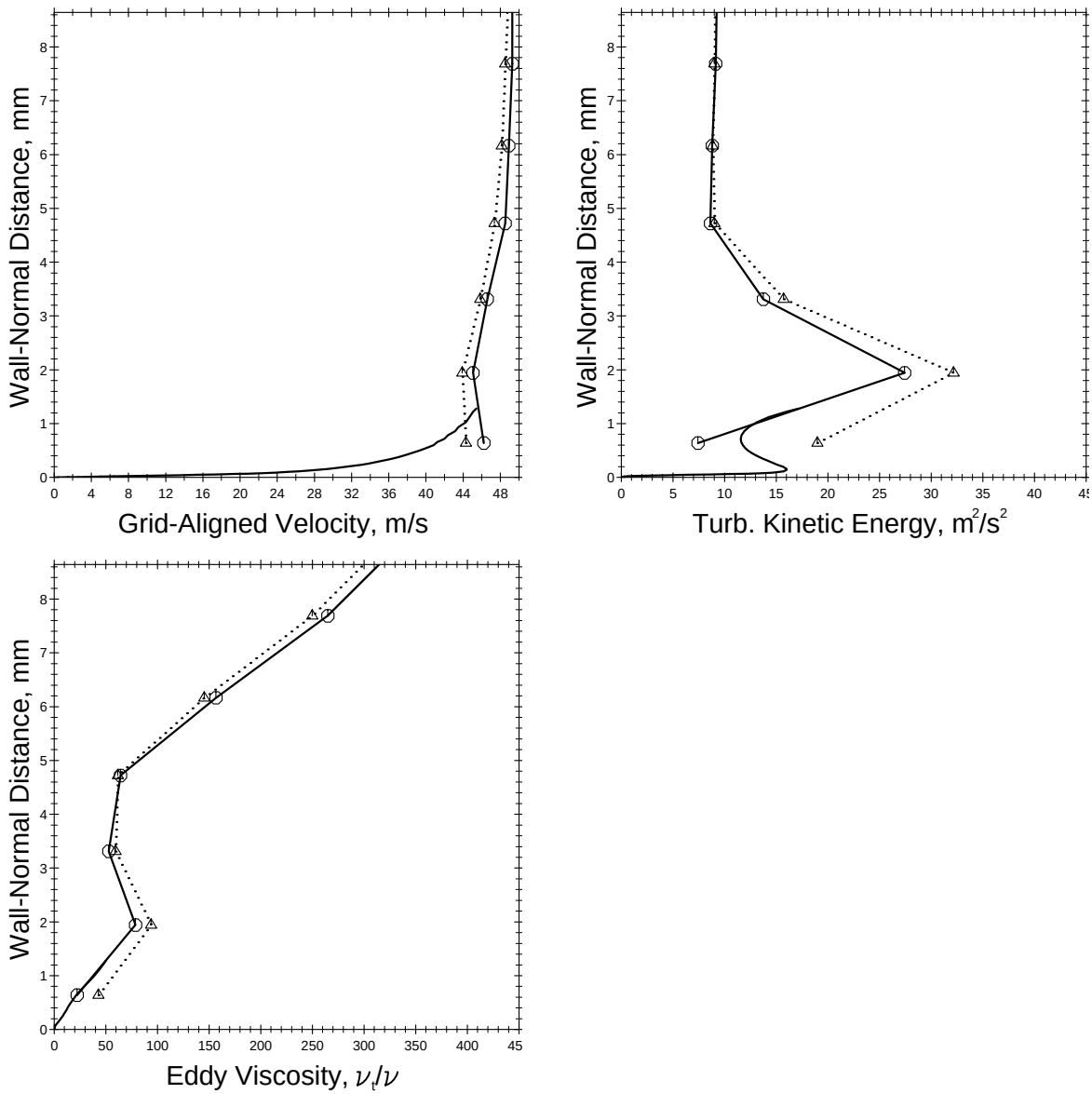

Figure 7.19: Wall-parallel mean velocity, turbulent kinetic energy and eddy-viscosity at $x \approx -194$mm on the slant surface and on centreline of the Ahmed body, —⊖—: linear $k-\varepsilon$ with UMIST-N wall function; ....△....: linear $k-\varepsilon$ with SCL wall function; (symbols indicate position of grid nodes).

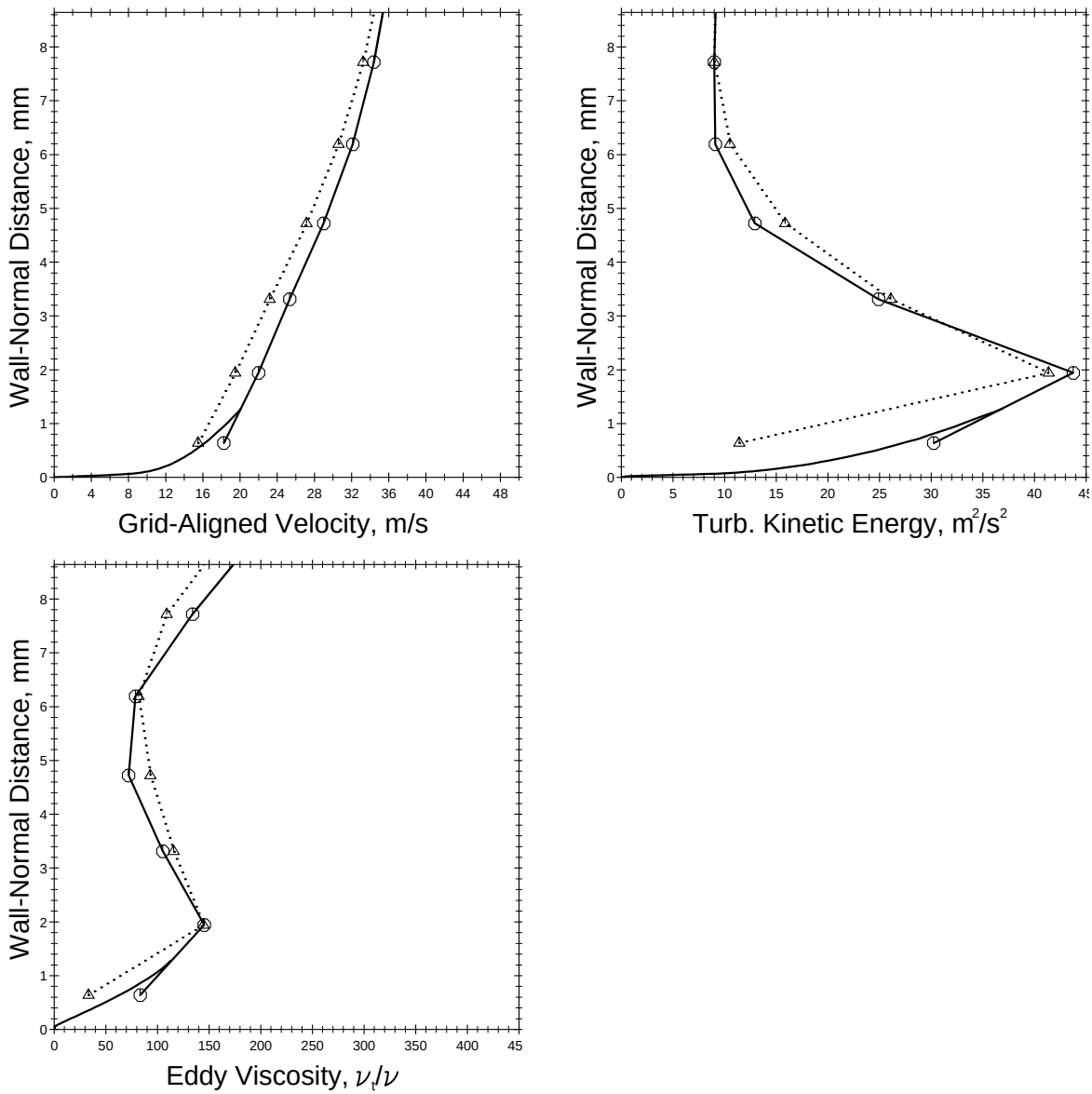

Figure 7.20: Wall-parallel mean velocity, turbulent kinetic energy and eddy-viscosity at $x \approx -165$mm on the slant surface and on centreline of the Ahmed body, —⊖—: linear $k-\varepsilon$ with UMIST-N wall function; ....△....: linear $k-\varepsilon$ with SCL wall function; (symbols indicate position of grid nodes).

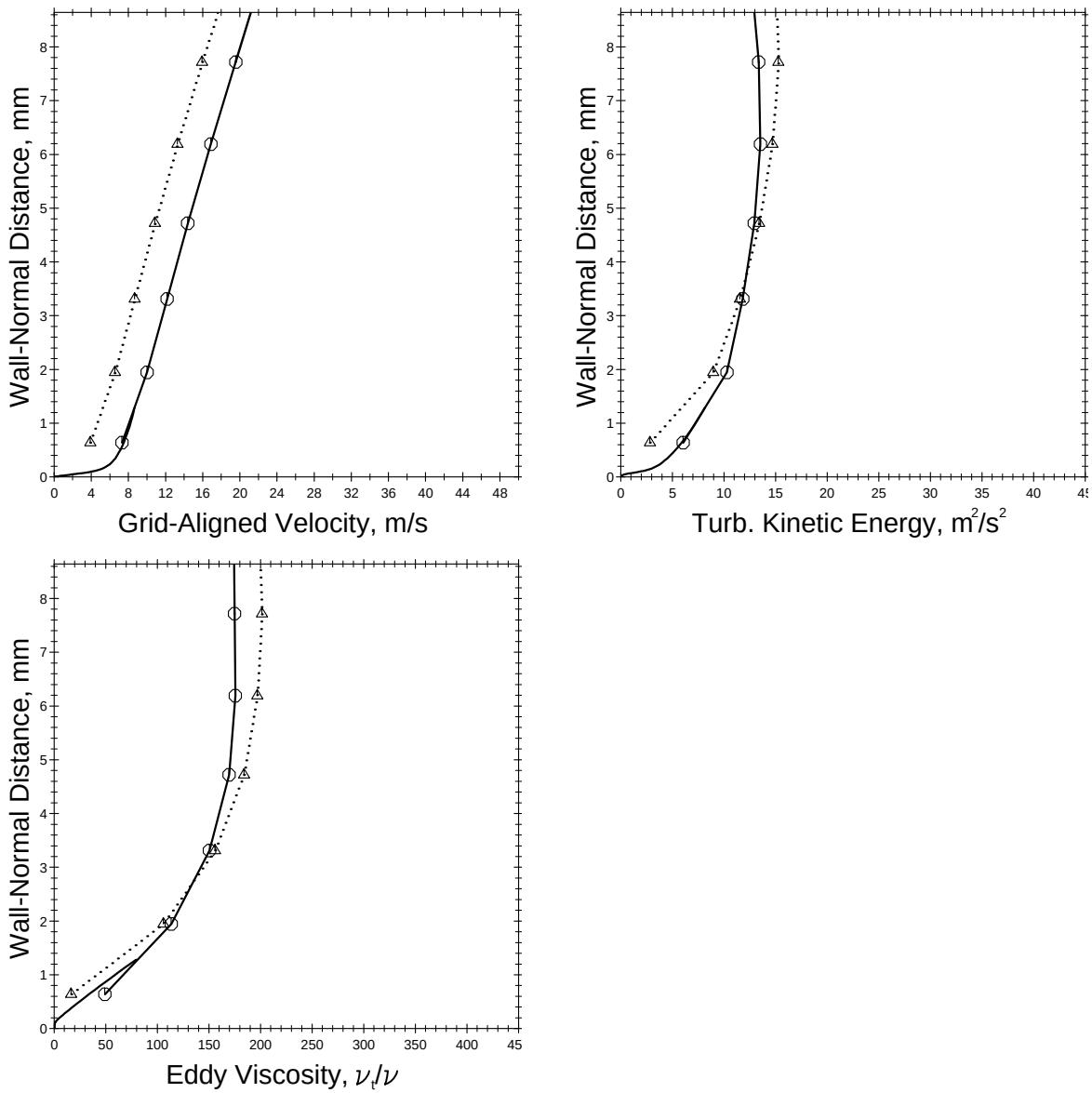

Figure 7.21: Wall-parallel mean velocity, turbulent kinetic energy and eddy-viscosity at $x \approx -109$mm on the slant surface and on centreline of the Ahmed body, —⊖—: linear $k-\varepsilon$ with UMIST-N wall function; ....△....: linear $k-\varepsilon$ with SCL wall function; (symbols indicate position of grid nodes).

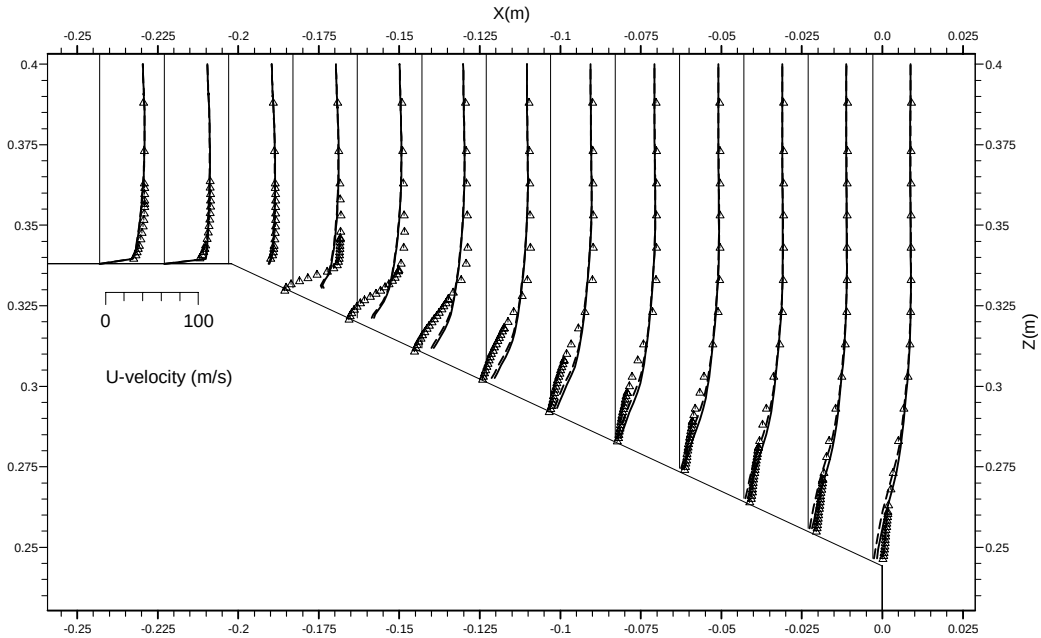

Figure 7.22: Mean U-velocity profiles over the Ahmed body 25° rear slant, ——: linear $k-\varepsilon$ with UMIST-N wall function; - - -: linear $k-\varepsilon$ with SCL wall function; △: experimental measurements of Lienhart *et al*. [138].

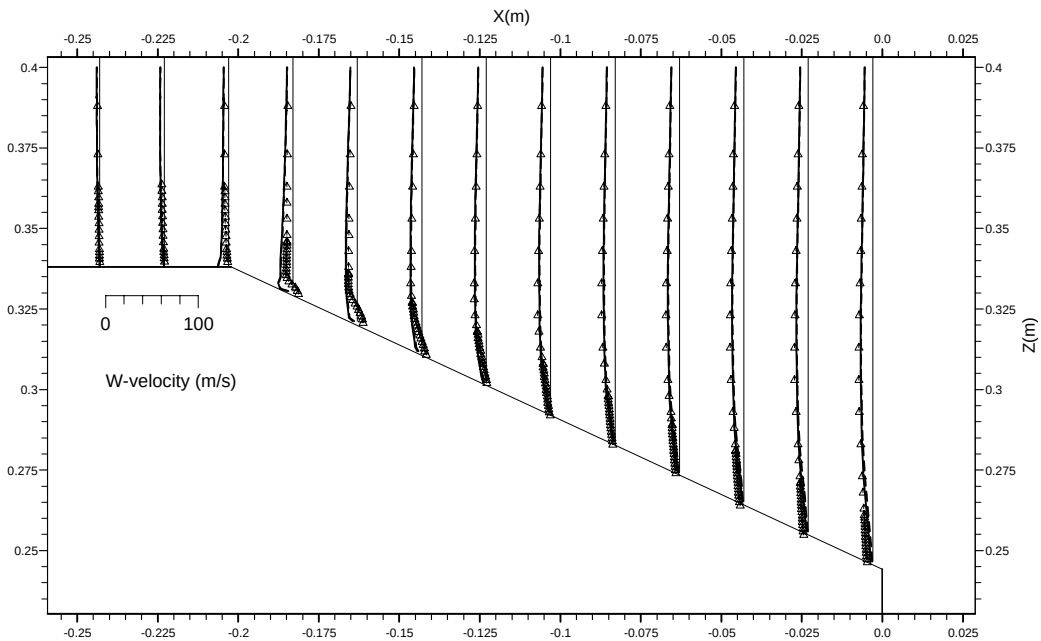

Figure 7.23: Mean W-velocity profiles over the Ahmed body 25° rear slant, ——: linear $k-\varepsilon$ with UMIST-N wall function; - - -: linear $k-\varepsilon$ with SCL wall function; △: experimental measurements of Lienhart *et al*. [138].

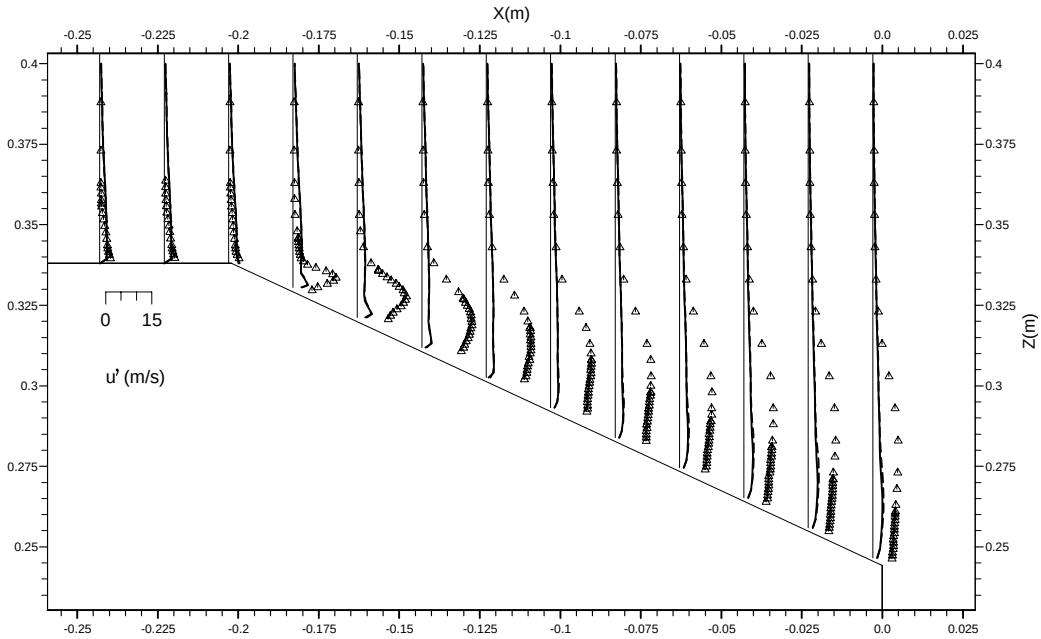

Figure 7.24: RMS u'-velocity profiles over the Ahmed body 25° rear slant, ——: linear $k-\varepsilon$ with UMIST-*N* wall function; - - -: linear $k-\varepsilon$ with SCL wall function; △: experimental measurements of Lienhart *et al*. [138].

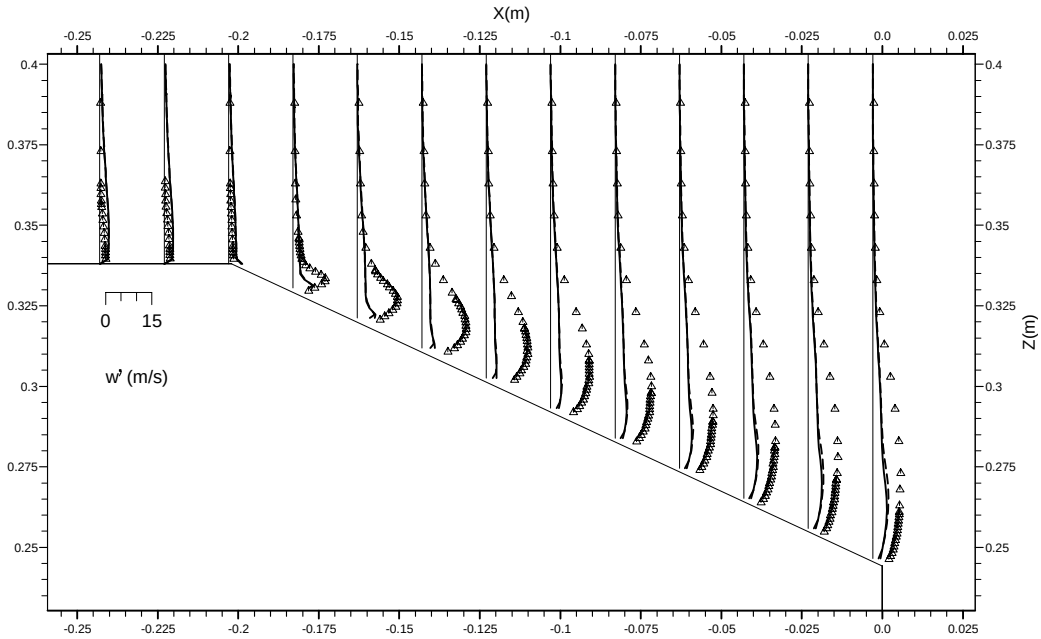

Figure 7.25: RMS w'-velocity profiles over the Ahmed body 25° rear slant, ——: linear $k-\varepsilon$ with UMIST-*N* wall function; - - -: linear $k-\varepsilon$ with SCL wall function; △: experimental measurements of Lienhart *et al*. [138].

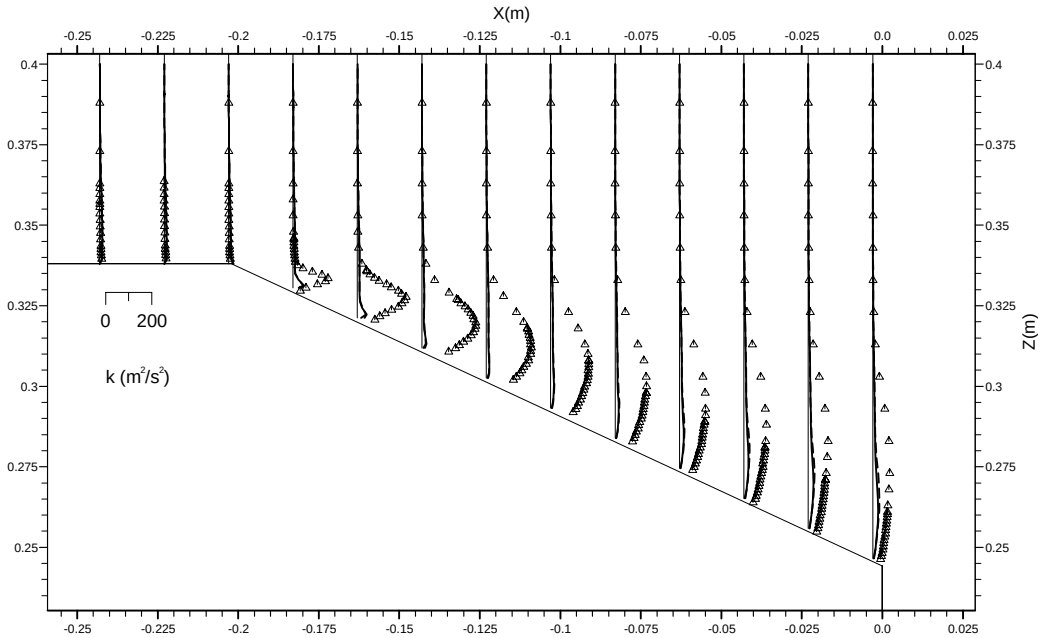

Figure 7.26: Turbulent kinetic energy profiles over the Ahmed body 25° rear slant, ——: linear $k-\varepsilon$ with UMIST-*N* wall function; - - -: linear $k-\varepsilon$ with SCL wall function; △: experimental measurements of Lienhart *et al*. [138].

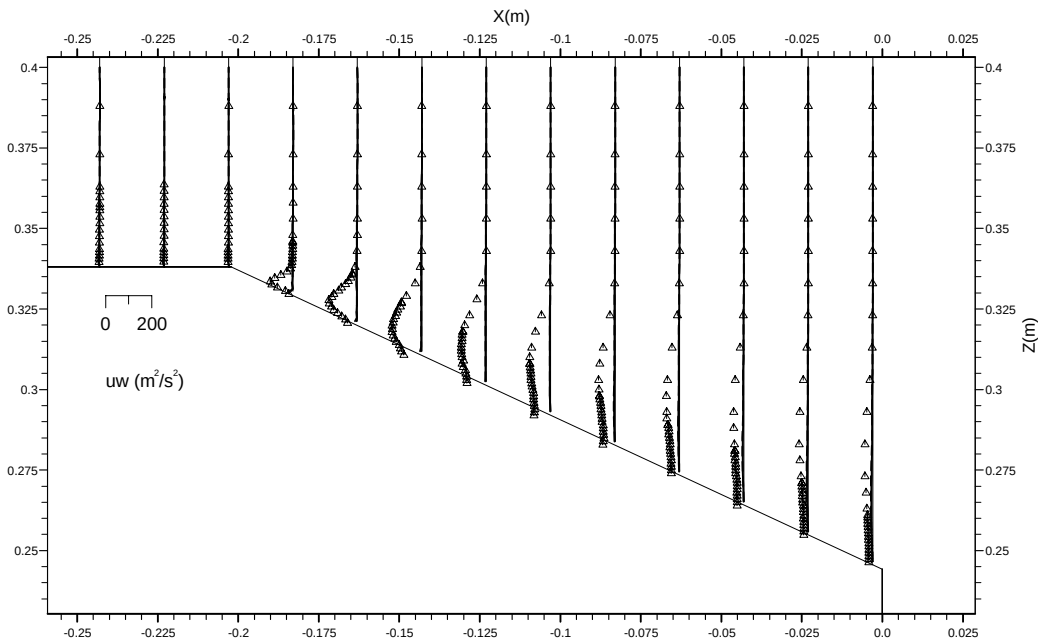

Figure 7.27: *uw*-stress profiles over the Ahmed body 25° rear slant, ——: linear $k-\varepsilon$ with UMIST-*N* wall function; - - -: linear $k-\varepsilon$ with SCL wall function; △: experimental measurements of Lienhart *et al*. [138].

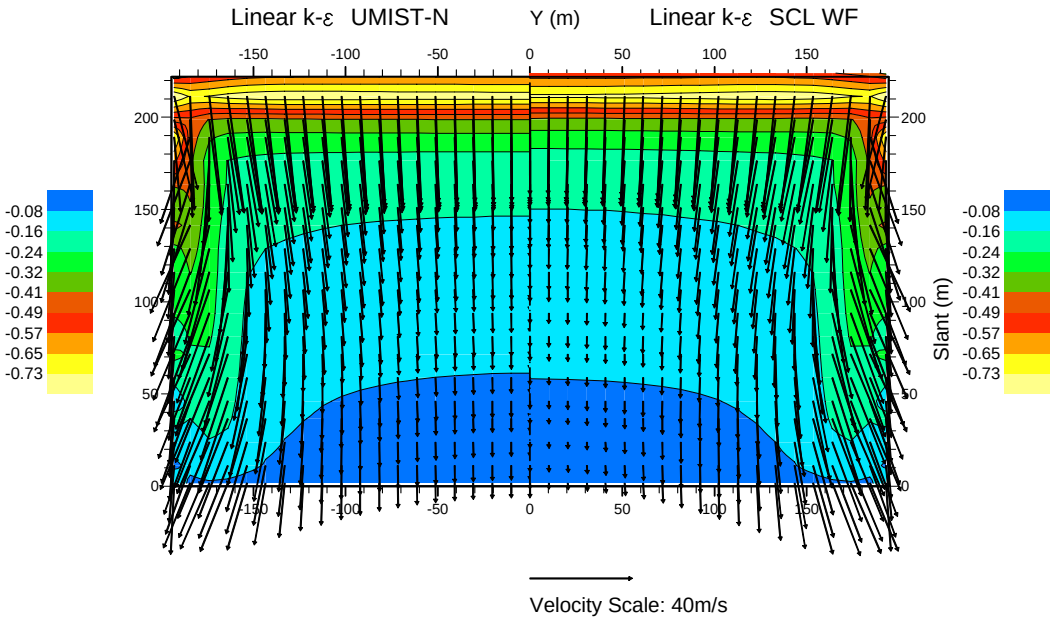

Figure 7.28: Velocity vectors and pressure coefficient contours on the Ahmed body 25° rear slant. The left half of the picture shows results from the linear $k-\varepsilon$ model with UMIST-N wall function and the right half the linear $k-\varepsilon$ model with SCL wall function. Velocity vectors shown are taken from values at the main-grid node adjacent to the wall surface.

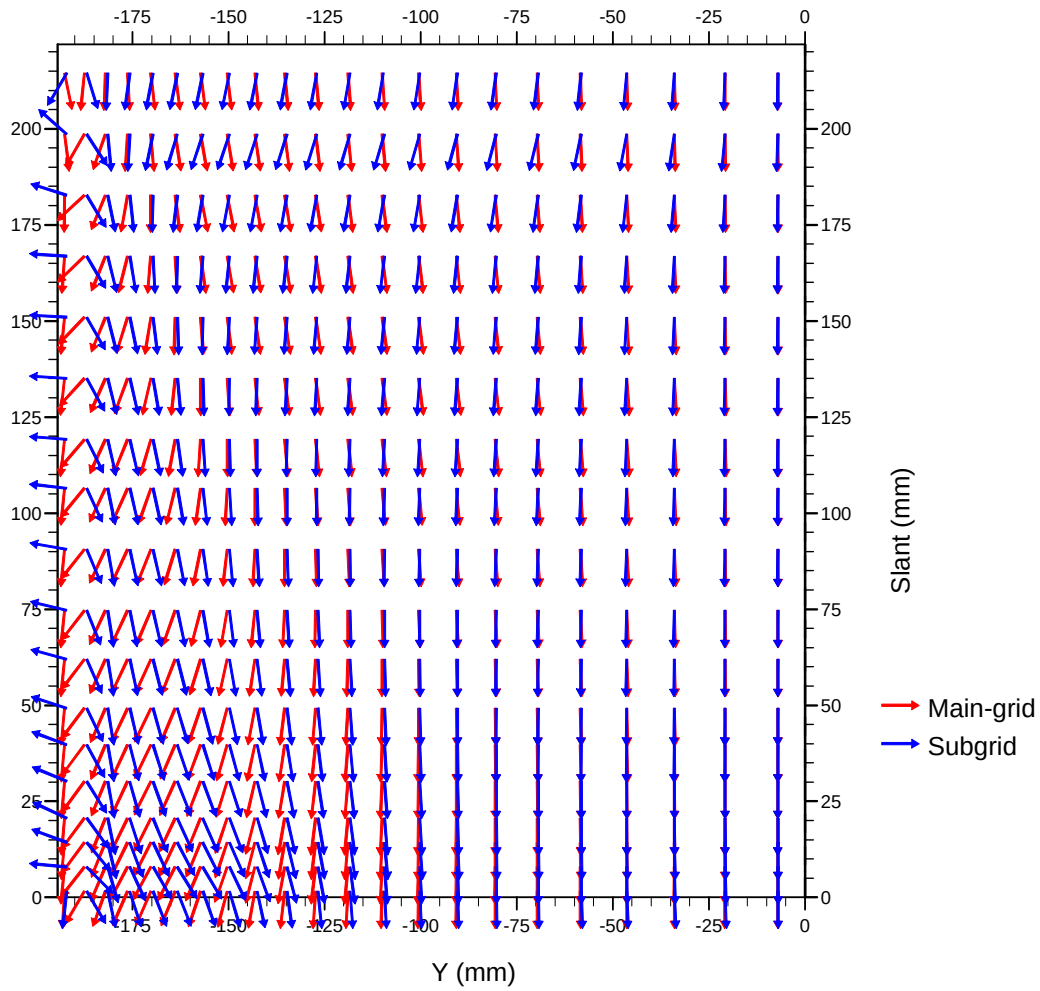

Figure 7.29: Velocity vectors on the Ahmed body 25° rear slant, as viewed from above (the axis of symmetry is on the right-hand y-axis). Results were obtained using the linear $k-\varepsilon$ model and UMIST-N wall function. Velocity vectors in red are the near-wall main-grid node values whilst vectors in blue are from the subgrid node which is closest to the wall (i.e. the subgrid node that is used to calculate the wall shear stress). Differences in the direction of the red and blue arrows therefore indicate skewing of the velocity vector between the main-grid node and the wall. The red vectors correspond to those shown on the left-hand-side of Figure 7.28. All vectors have been specified with unit length.

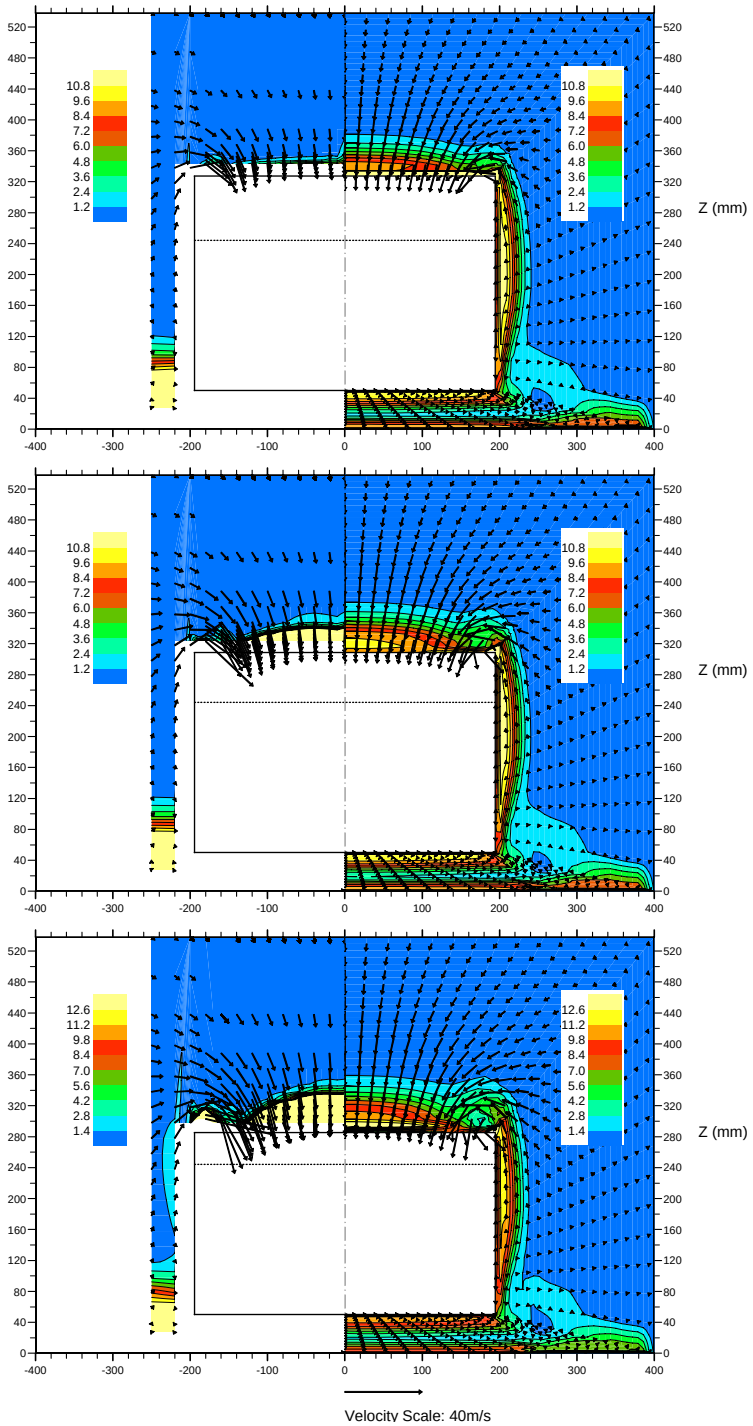

Figure 7.30: Velocity vectors and turbulent kinetic energy contours (in m^2s^{-2}) around the rear of the Ahmed body. The left half of the pictures show experimental data from Lienhart *et al.* [138] and the right half predictions using the linear $k-\varepsilon$ model with UMIST-*N* wall function. The outline of the Ahmed body is shown in solid lines and the slant edge in broken lines. The top picture is at $x = -178$mm, the middle at $x = -138$mm and bottom at $x = -88$mm.

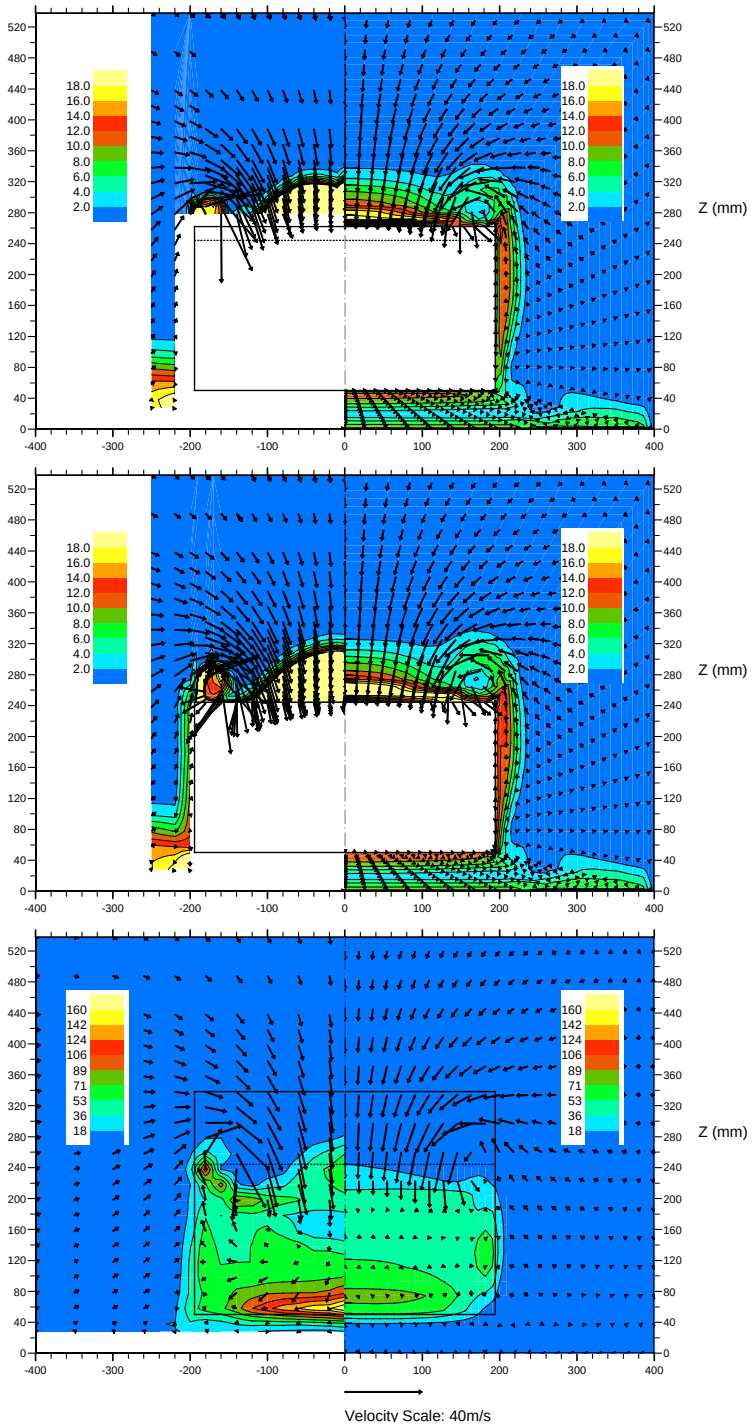

Figure 7.31: Velocity vectors and turbulent kinetic energy contours (in m^2s^{-2}) around the rear of the Ahmed body. The left half of the pictures show experimental data from Lienhart *et al.* [138] and the right half predictions using the linear $k-\varepsilon$ model with UMIST-*N* wall function. The outline of the Ahmed body is shown in solid lines and the slant edge in broken lines. The top picture is at $x = -38$mm, the middle at $x = 0$mm and bottom at $x = 80$mm.

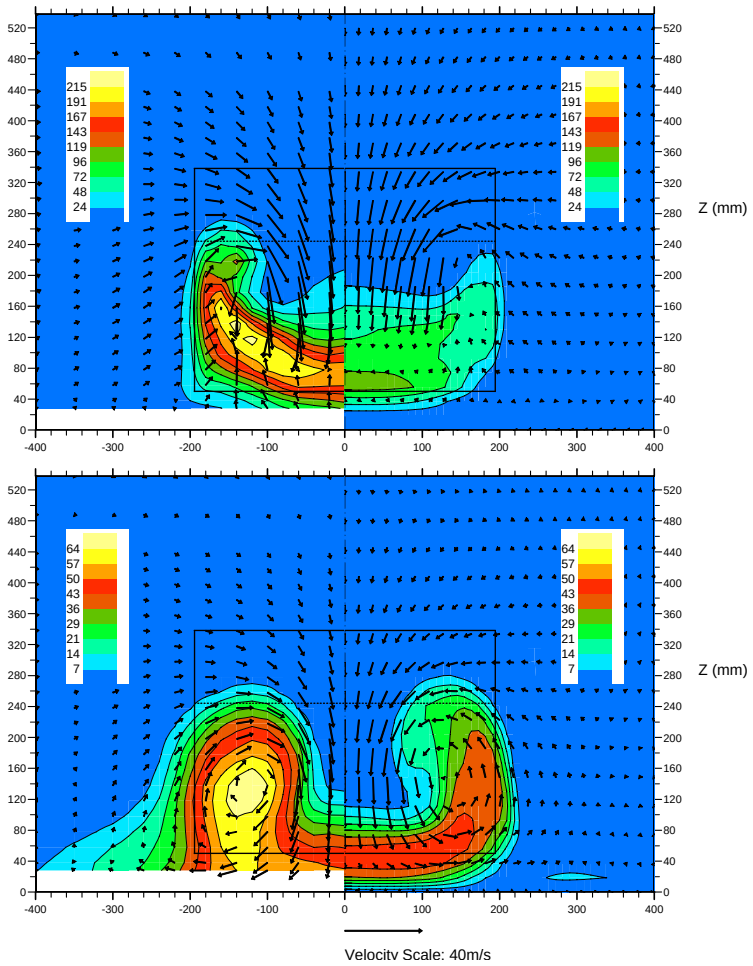

Figure 7.32: Velocity vectors and turbulent kinetic energy contours (in m^2/s^2) around the rear of the Ahmed body. The left half of the pictures show experimental data from Lienhart *et al*. [138] and the right half predictions using the linear $k-\varepsilon$ model with UMIST-*N* wall function. The outline of the Ahmed body is shown in solid lines and the slant edge in broken lines. The top picture is at $x = 200$mm and the bottom at $x = 500$mm.

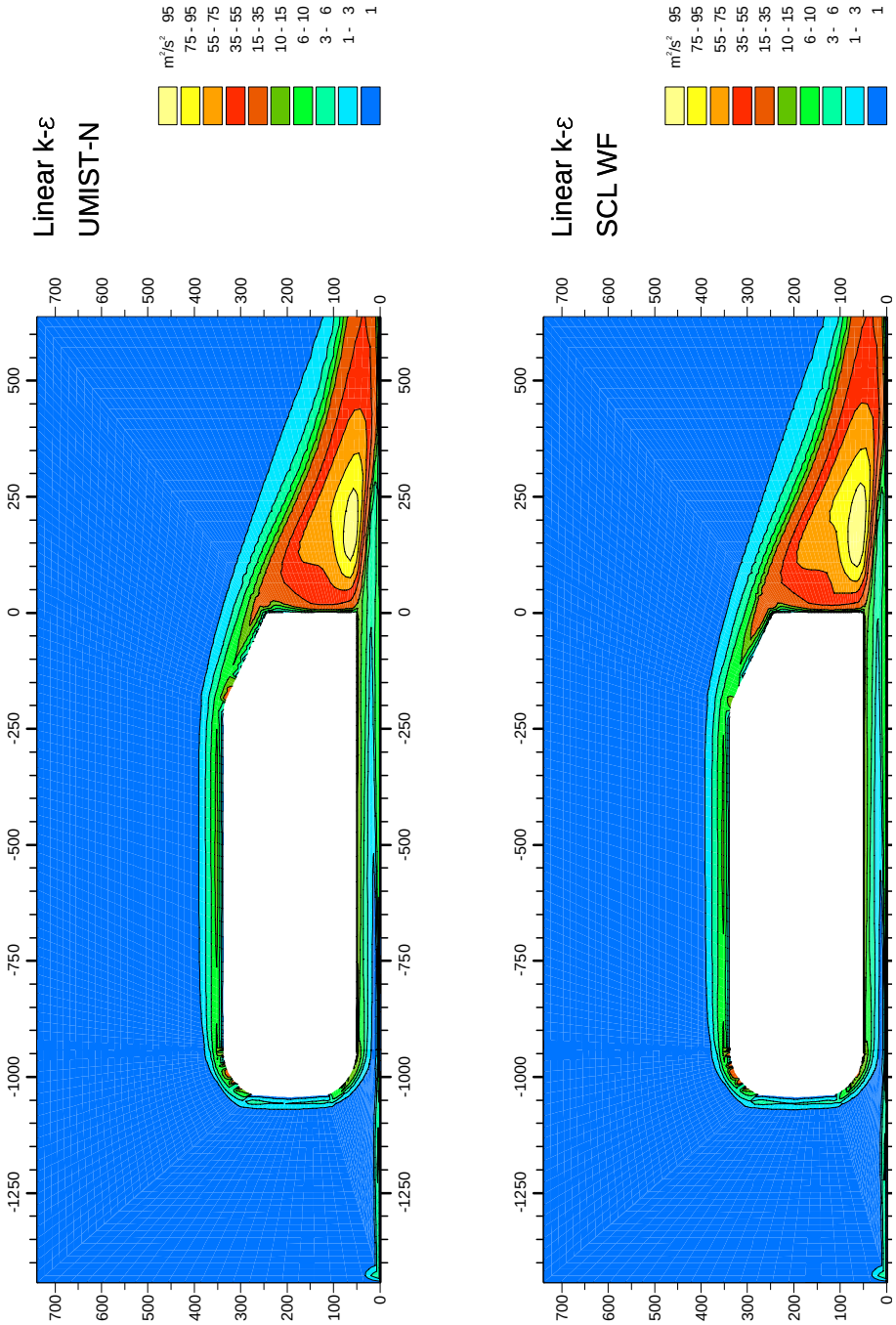

Figure 7.33: Turbulent kinetic energy contours around the Ahmed body at $y = 0$ using the linear $k - \varepsilon$ model with the UMIST-N wall function (top) and the linear $k - \varepsilon$ model with the Simplified Chieng & Launder wall function (bottom).

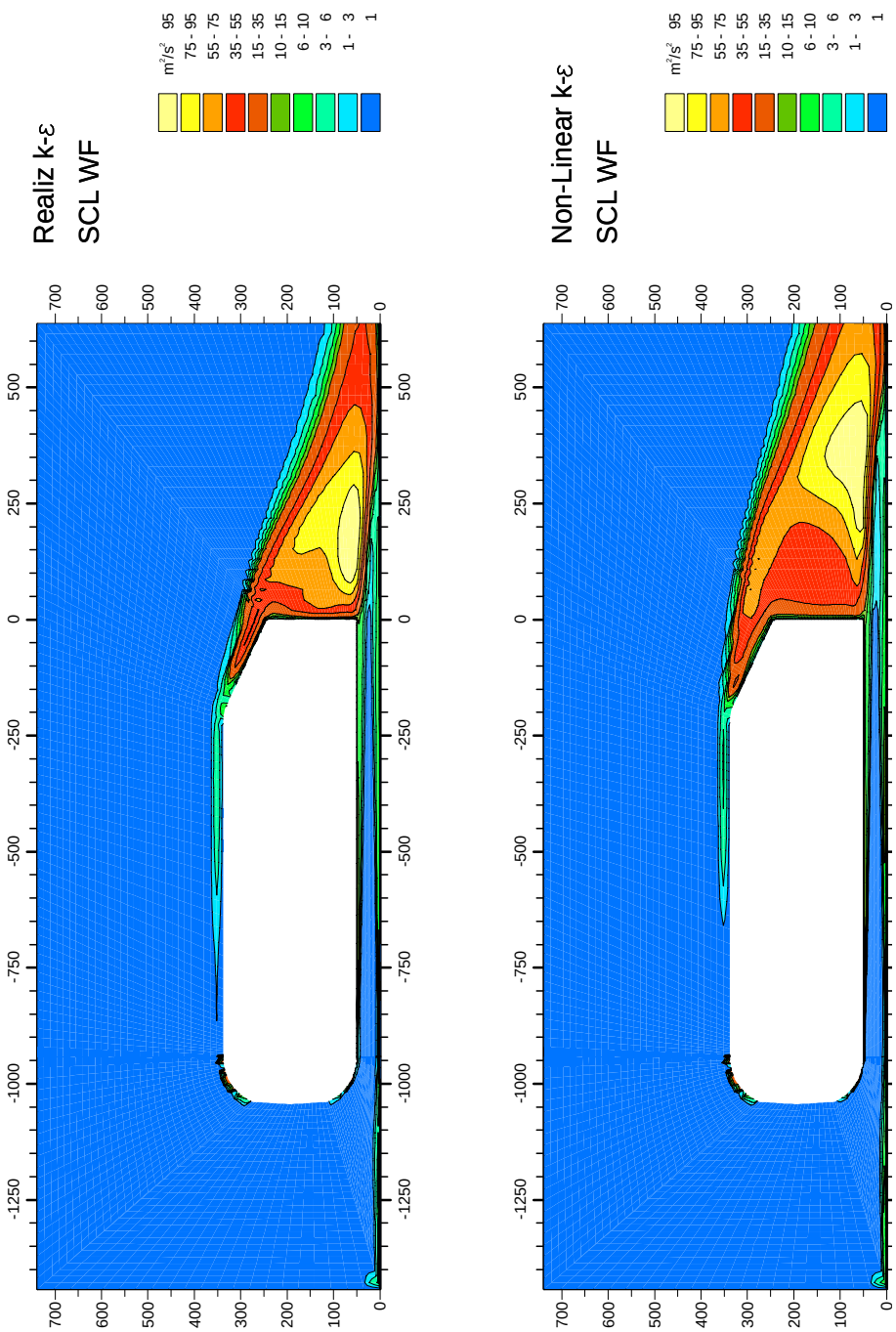

Figure 7.34: Turbulent kinetic energy contours around the Ahmed body at $y = 0$ using the realizable linear $k - \varepsilon$ model with the SCL wall function (top) and the non-linear $k - \varepsilon$ model with the SCL wall function (bottom). Both realizable and non-linear model computations were undertaken by Robinson [35].

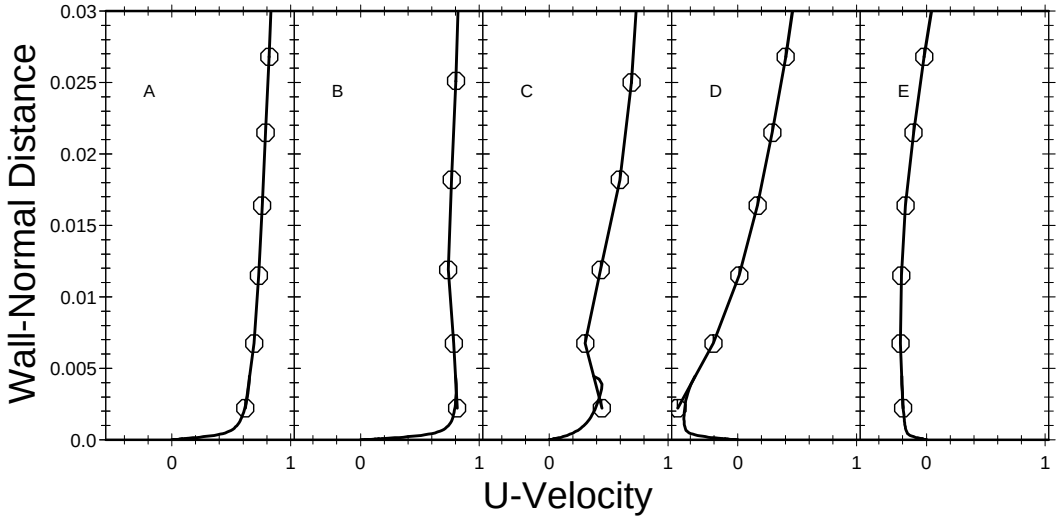

Figure 7.35: Profiles of the wall-parallel U-velocity at five positions around the 90° rear corner of the Ahmed body, A, B, C, D and E, shown in Figure 7.36. Results were obtained using the linear $k-\varepsilon$ model with the UMIST-N wall function (including the $\partial P/\partial\zeta$ term). Symbols indicate main-grid nodal values and the subgrid velocity distribution is also shown. The wall-normal distance is non-dimensionalized with the height of the car body $(L = 288\text{mm})$ and velocity with the free-stream value $\left(U_0 = 38.51\text{ms}^{-1}\right)$.

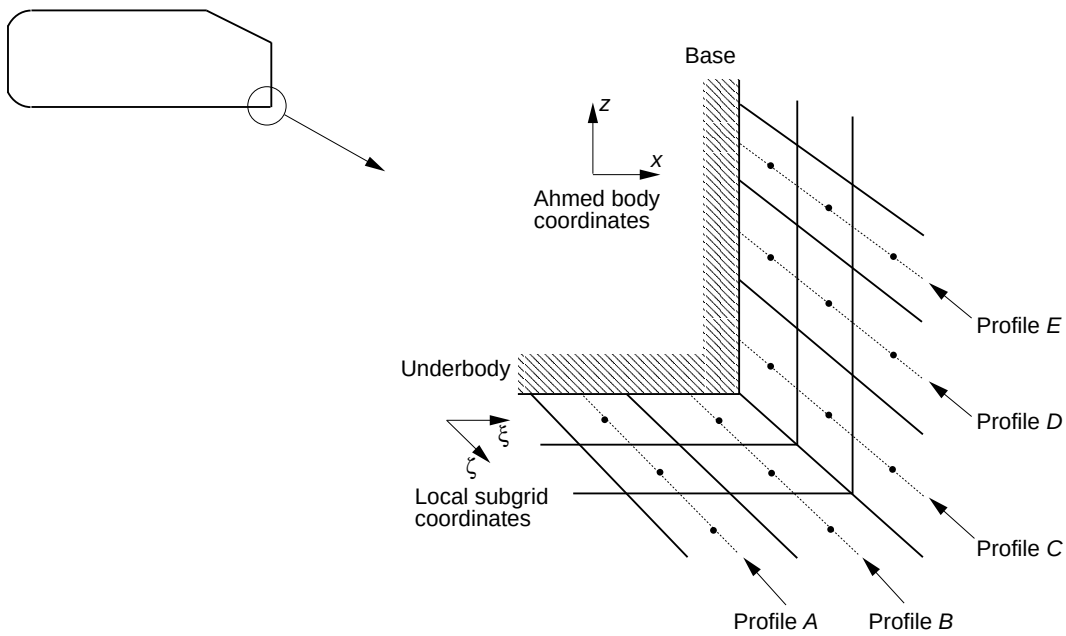

Figure 7.36: Sketch of the rear corner of the Ahmed body showing the local grid arrangement and the location of profiles used in Figures 7.35, 7.37 and 7.38.

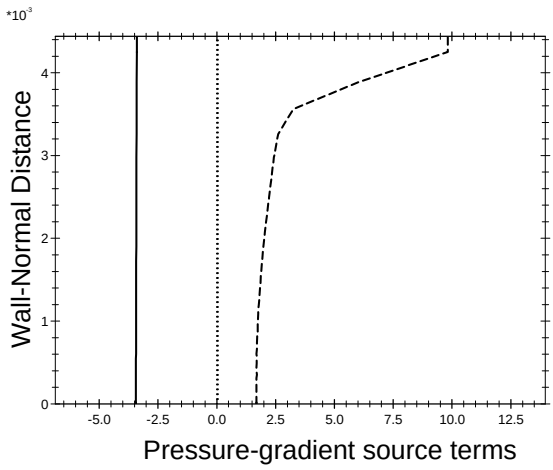

Figure 7.37: Profiles of the three pressure-gradient source terms appearing in the subgrid U-momentum equation at position C adjacent to the 90° rear corner of the Ahmed body, shown in Figure 7.36; —-: $\left(\sqrt{g_{11}}g^{11}\partial P/\partial\xi\right)$; ....: $\left(\sqrt{g_{11}}g^{12}\partial P/\partial\eta\right)$; - - -: $\left(\sqrt{g_{11}}g^{13}\partial P/\partial\zeta\right)$. Results were obtained using the linear $k-\varepsilon$ model with the UMIST-N wall function. The wall-normal distance is non-dimensionalized with the height of the car body $(L = 288\text{mm})$.

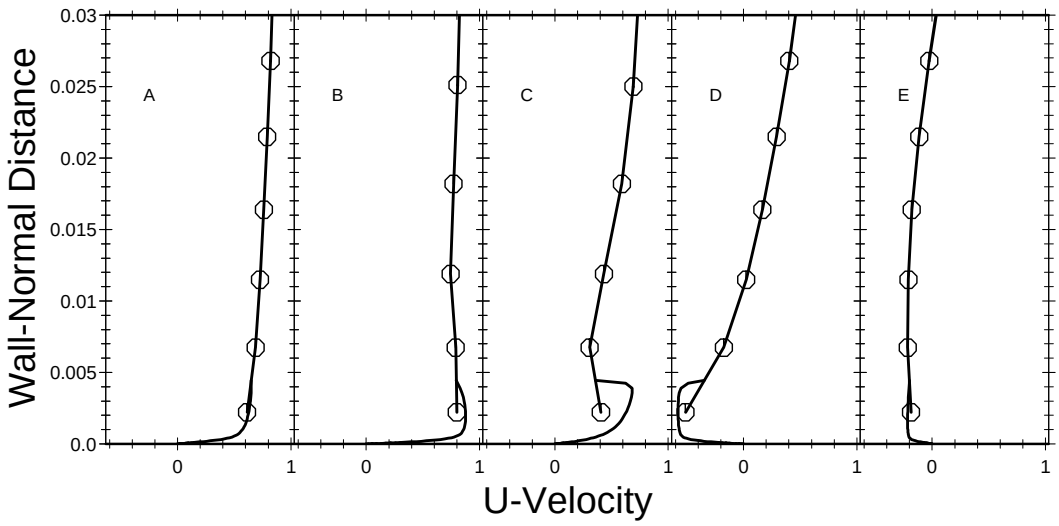

Figure 7.38: Profiles of the wall-parallel U-velocity at five positions around the 90° rear corner of the Ahmed body, shown in Figure 7.36. Results were obtained using the linear $k-\varepsilon$ model with the UMIST-N wall function (without the $\partial P/\partial\zeta$ term). Symbols indicate main-grid nodal values and the subgrid velocity distribution is also shown. The wall-normal distance is non-dimensionalized with the height of the car body $(L = 288\text{mm})$ and velocity with the free-stream value $\left(U_0 = 38.51\text{ms}^{-1}\right)$.